Abstract

HEHR, BRIAN DOUGLAS. Development of the Thermal Neutron Scattering Cross Sections of Graphitic Systems using Classical Molecular Dynamics Simulations. (Under the direction of Prof. Ayman I. Hawari.)

Proposed next-generation nuclear reactor concepts such as the High Temperature Gas Reactor (HTGR) and Very High Temperature Reactor (VHTR) incorporate graphite as a structural material and neutron moderator. The details of neutron slowing-down and thermalization in graphite impact the reactor energy spectrum, which, in turn, influences core design and fuel loading calculations. Of particular interest is the behavior of the graphite scattering cross section at thermal energies (below about 1 eV) where the interatomic binding environment of carbon atoms in the system determines the form of the differential cross section. In the absence of material-specific thermal cross sections, neutronics codes will, by default, utilize the free-gas approximation, which is commonly a drastic overestimation of the true cross section.

In this work, the thermal cross sections of graphite were developed, using classical molecular dynamics (MD), for crystalline graphite and for graphite structures subjected to displacement cascades simulating the exposure to neutron irradiation. This was made possible through the implementation of Van Hove correlation functions linking the atomic trajectories to the neutron scattering phenomenon. In order to evaluate the cross section directly from the atomic trajectories, significant quantum effects were integrated into the (real and symmetric) classical scattering formulae. For incoherent scattering, the specific phenomena of

importance are detailed balance and atomic recoil, and a correction scheme has been developed herein to account for both. This correction takes the form of a transformation between the real and imaginary parts of the intermediate scattering function, established on the basis of a fluctuation-dissipation type relation. The transformed intermediate function is shown to produce consistent differential cross sections that are in agreement with *ab-initio* based calculations. Furthermore, the transformation procedure is proven to reduce to the appropriate semiclassical limits at the extremes of small and large momentum transfers.

Correlations among the positions of distinct atomic pairs are also computed for the purpose of ascertaining the coherent inelastic cross section. These are validated against experimental measurements of the total scattering law and cross section of graphite. The Van Hove approach is markedly advantageous in this respect because the coherent inelastic component, which accounts for as much as 20-25% of the total graphite cross section, is inaccessible in the LEAPR / NJOY formalism used to generate the standard ENDF/B-VII graphite libraries.

Additionally, damage was introduced into the MD graphite model through a series of collision cascades, each beginning with a randomly selected primary knock-on atom of energy 1 – 1.5 keV. As the cascade concentration was raised (simulating higher radiation exposure levels), increasingly complex defect formations were observed and specific defect types were identified including simple vacancies and interstitials, the Stone-Wales defect, the interplanar divacancy defect, interplanar cross-linking and regions of near-amorphization.

Total amorphization was also studied by melting and rapidly quenching the system at different densities.

For the purpose of studying the effect of damage on the cross section and frequency distribution, collision cascade concentrations were accumulated in an 8000-atom crystalline MD system. A transition from the crystalline frequency distribution towards the amorphous distribution was confirmed in the damaged region of the cell, associated with a dampening of the high-frequency in-plane optical modes of the vibrational spectrum, an enhancement of the out-of-plane modes, and a flattening of overall distribution. The total cross section was found to increase by as much at 48%, with the most significant change occurring in the 0.01-0.03 eV range.

Development of the Thermal Neutron Scattering Cross Sections of Graphitic Systems using Classical Molecular Dynamics Simulations

by
Brian Douglas Hehr

A dissertation submitted to the Graduate Faculty of
North Carolina State University
in partial fulfillment of the
requirements for the Degree of
Doctor of Philosophy

Nuclear Engineering

Raleigh, North Carolina

2010

APPROVED BY:

_____	_____
Dr. Ayman I. Hawari, Chair of Advisory Committee	Dr. Mohamed A. Bourham
_____	_____
Dr. Bernard W. Wehring	Dr. Albert R. Young

Biography

Brian Douglas Hehr was born in Reading, Pennsylvania to parents Steven and Brenda Hehr. At the age of 3, Brian and his family moved to the vicinity of Charlotte, NC. Brian graduated from Sun Valley High School in 2000 and subsequently enrolled at North Carolina State University, where he graduated *summa cum laude* with dual B.S. degrees in physics and nuclear engineering. During his undergraduate studies, Brian participated in four summer internships – two at the Clariant Corporation headquarters in Charlotte and two at Los Alamos National Laboratory in New Mexico.

Immediately following graduation, Brian began working with Dr. Ayman Hawari of North Carolina State University on atomistic graphite simulations. Upon completing his Master's degree in the summer of 2007, Brian continued on as a Ph.D. student, this time focusing on thermal neutron scattering.

Acknowledgements

I would like to offer my heartfelt gratitude to Dr. Ayman Hawari for guiding my endeavors in this project and providing advice on both my Ph.D. work and future career. His ideas formed the foundation upon which the developments of this dissertation have matured. Dr. Hawari's patience and motivation have been inspirational during my studies, and I aspire to emulate his dedication throughout my own career. I would also like to thank him for supporting my attendance at professional conferences, which has afforded me a valuable opportunity to communicate with others in my field.

The remaining members of my dissertation committee – Dr. Mohamed Bourham, Dr. Bernard Wehring, and Dr. Albert Young – deserve recognition as well for setting aside their valuable time to serve in this role.

Many thanks to Dr. Iyad Al-Qasir for always taking the time to talk with me, no matter how busy. I have learned much from his extensive knowledge of physics. I would also like to extend my appreciation to Dr. Victor Gillette for sharing his considerable programming experience as well as his expertise in a variety of topics.

Table of Contents

List of Tables

List of Figures

Chapter 1

Introduction

1.1 Overview

The use of graphite as a moderator and structural material dates back to the Chicago Pile I experiment of 1942, during which the world's first artificially induced, self-sustained chain reaction was achieved. Since then, graphite has been integrated into commercial and research reactors worldwide; the Russian RMBK fleet and the British Dragon reactor, for instance, have both featured graphite as the neutron moderator. A number of Generation-IV designs, including the Very High Temperature Reactor (VHTR), likewise incorporate graphite either as stacked prismatic blocks or in pebble form with embedded TRISO fuel particles. A schematic of the proposed VHTR system is shown in Fig. 1-1.

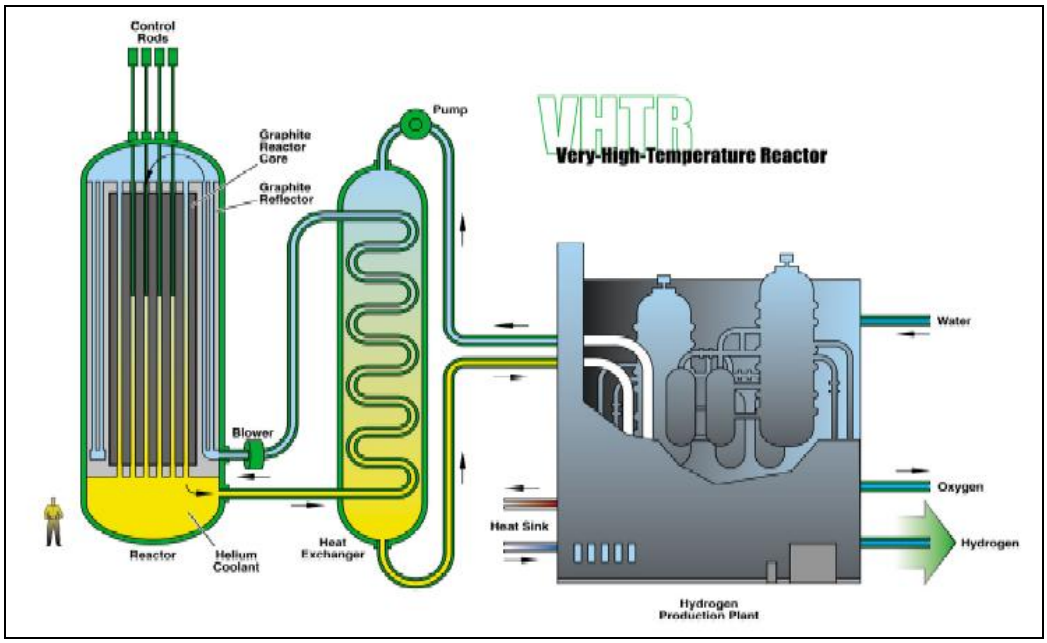

Fig. 1-1. Diagram of the Very High Temperature Reactor (VHTR) concept [1] .

At present, the majority of commercial power reactors are water-moderated. The resurgence of graphite has been driven by certain advantageous physical properties that include excellent mechanical strength, low density, high melting temperature, large heat capacity, and a low neutron absorption cross section. The standard metric for rating the effectiveness of a moderator is the *moderating ratio*, given by the formula:

$$\varepsilon_M = \frac{\xi \Sigma_s}{\Sigma_a} \tag{1.1}$$

where Σ_s is the scattering cross section, Σ_a is the absorption cross section, and ξ, the average lethargy gain, is defined as:

$$\xi = 1 - \frac{(A-1)^2}{2A} \ln\left(\frac{A+1}{A-1}\right) \tag{1.2}$$

in which A is the atomic mass number of the moderator. Essentially, ξ is a measure of the average energy lost by the neutron in a collision with a moderator atom. The purpose of the moderator is to deliver low-energy neutrons to the fuel; therefore, the moderating ratio is directly proportional to the lethargy gain and scattering cross section, and inversely proportional to the absorption cross section, which represents a neutron removal mechanism. The moderating ratio of several common moderator materials is tabulated in Table 1.1.

Table 1.1. Atomic number and moderating ratio of select moderators [2]

Moderator	A	$\xi\Sigma_s / \Sigma_a$
H_2O	1 (H),16 (O)	71
D_2O	2 (D),16 (O)	5670
C	12	192
Be	9	143

Deuterium oxide (heavy water) far outshines other moderators in terms of ε_M , chiefly because of its tiny absorption cross section. This advantage is offset by the hefty price of manufacturing heavy water, as well as the requirement of a high pressure environment to prevent vaporization. The pressure constraint is particularly detrimental in new reactor designs such as the VHTR which emphasize high temperature operation as a means of increasing thermodynamic efficiency. Graphite, the second most effective moderator in Table 1.1, retains its structural integrity even at temperatures approaching the melting point of 3650˚C [3] – well above the expected accident temperature in a VHTR, for instance.

In fact, graphite acts not only as the moderator in the VHTR concept, but also as a structural material. As mentioned, graphite remains stable well above accident temperatures and can absorb excess heat like a thermal sponge in, for instance, an overpower or loss of coolant event. Perhaps the most limiting accident scenario presently under consideration is a pipe break that enables air ingress into the core. At high temperatures, graphite reacts exothermically with oxygen to produce the toxic gas CO (carbon monoxide), and the heat of reaction serves to increase the core maximum temperature still further, raising the specter of a graphite fire. Such an event transpired in 1957 at the Windscale reactor in Britain, where an uncontrolled release of Wigner energy set the air-cooled core ablaze [4]. Given this possibility, current designs for gas cooled reactors typically specify an inert coolant such as helium. The buildup of stored (Wigner) energy remains a concern, however, and this topic will be revisited in more depth later.

1.2 Forms of Graphite

1.2.1 Perfect Graphite

The graphite structure is illustrated in Fig. 1-2. In its perfectly crystalline state, graphite exhibits a hexagonal, planar configuration with ABAB type stacking. A rhombohedral form also exists with ABC stacking yet identical in-plane properties. Whereas neighboring layers of atoms are weakly bound through Van der Waals forces, the characteristic honeycomb structure of each plane is held together by strong covalent bonds, resulting in a high degree of anisotropy in the system properties. Two distinct atomic sites exist in graphite: one is distinguished by the presence of atoms directly above and below in neighboring planes (at $\pm$ c/2) and the other by honeycomb gaps above and below.

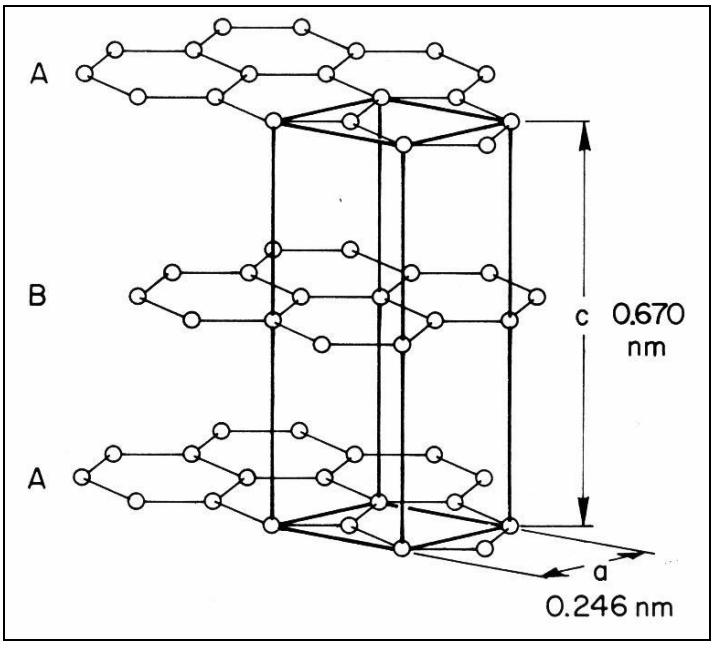

Fig. 1-2. Graphite structure and lattice parameters (at 0 K). The hexagonal unit cell of graphite is demarcated in bold lines.

To define the system mathematically, a grid of lattice points is constructed wherein the displacement between any two points is given by:

$$\Delta\vec{r} = A\vec{a} + B\vec{b} + C\vec{c} \tag{1.3}$$

in which A,B, and C are integers and $\vec{a}$, $\vec{b}$, and $\vec{c}$ are the primitive translation vectors. Defining α, β, and γ as the angles between vectors $\vec{b}$ - $\vec{c}$, $\vec{a}$ - $\vec{c}$, and $\vec{a}$ - $\vec{b}$ respectively, the hexagonal lattice corresponds to the conditions $a = b \neq c$, $\alpha = \beta = 90^0$ and $\gamma = 120^0$. An example of a hexagonal lattice is shown in Fig. 1-3.

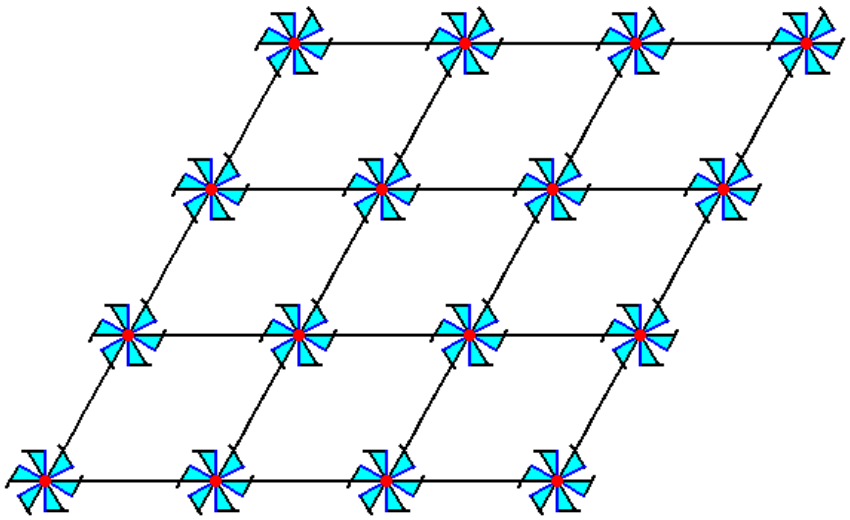

Fig. 1-3. The hexagonal lattice. Elements of rotational symmetry are indicated by blue triangles.

The structure of any crystal is specified unequivocally through a combination of the lattice and basis, where the basis represents translations relative to a lattice site. All other atoms are equivalent by symmetry to these basis atoms, and indeed, the crystal system itself can be

visualized as the product of infinite repetitions of the basis atoms. For graphite, there are four basis sites, which, specified as fractions of a unit cell, are:

C1: [0 , 0 , 1/4]

C2: [0 , 0 , 3/4]

C3: [1/3 , 2/3 , 1/4]

C4: [2/3 , 1/3 , 3/4]

Since the basis positions and primitive vector angles are rigidly fixed in the hexagonal symmetry group associated with graphite, all that remains is to establish the *lattice parameters*, i.e. the unit cell scaling factors that generate the minimum-energy crystal structure at a given temperature. As depicted in Fig. 1-2, these are a = 2.46 Å (in-plane) and c = 6.7 Å (out-of-plane) in 0 K graphite, resulting in a nearest-neighbor interatomic spacing of 1.42 Å. The phenomenon of thermal expansion (or contraction) arises from a temperature-dependent shift in the lattice parameters due to anharmonicity in the interatomic potential energy.

1.2.2 Reactor-Grade Graphite

Graphite manufactured for use in the nuclear industry differs from ideal (crystalline) graphite in certain respects. First, the constituent graphitic crystallites are randomly oriented, rather than aligned along a single c-axis. Second, the crystalline regions are embedded in a porous matrix of amorphous carbon, and the average density of reactor-grade graphite is consequently lower than that of perfect graphite (approximately 1.6 – 1.85 g/cm^3 as opposed

to 2.25 g/cm^3) [5]. Third, impurities that adversely affect reactor performance, such as boron, are largely removed in the production of reactor-grade graphite.

In addition to randomization in the orientation of crystallites, disorder is also observable in the interlayer spacing and stacking. Whereas perfect graphite exhibits a single, characteristic interlayer spacing in hexagonal form and a different, but still constant, spacing in rhombohedral form, the spacings in reactor-grade graphite are subject to variability. Deviations from the nominal spacing have been represented, in past work [6], using a Gaussian distribution. Moreover, the graphitic layers are turbostratic in reactor-grade such that adjacent layers may be translated or rotated randomly in relation to each other [7]. A consequence of this disorder is that the ABAB stacking sequence is broken, and, in fact, many of the characteristic powder diffraction peaks of graphite are broadened or lost entirely [8].

Bearing in mind the lower density of reactor-grade graphite as well as its coexistent phases, one would expect the properties of the reactor-grade and crystalline variants to diverge significantly. Indeed, the properties of reactor-grade graphite are much more isotropic due to the lack of a collective orientation (although some anisotropy still exists because of the *extrusion* process). In terms of structural integrity, isotropy is an advantage in nuclear applications because the moderator will undergo uniform dimensional changes under heating or irradiation.

1.3 Nuclear Cross Sections

Consider a monoenergetic beam of neutrons incident on a thin slab of known composition. Assuming that attenuation is negligible within the slab, the neutron-nuclear reaction rate will be uniform and a *cross section* proportional to the probability of reaction can be defined as:

$$\sigma = \frac{R}{\phi N_D} \tag{1.4}$$

where R is the reaction rate density, ϕ is the incident flux (# of neutrons per unit area per unit time) and N_D is the atomic number density of the slab. Dimensionally, the nuclear cross section therefore represents an area, consistent with its original conceptualization as the effective "target area" presented to an incoming particle. While the cross section is a simple constant in this hypothetical example, a more constructive approach is to assign separate cross sections to different modes of interaction. The focus of this study is on scattering interactions in which the relevant neutron variables are the incident energy, scattered energy, and the scattering angle. A diagram of a neutron scattering event is shown in Fig. 1-4.

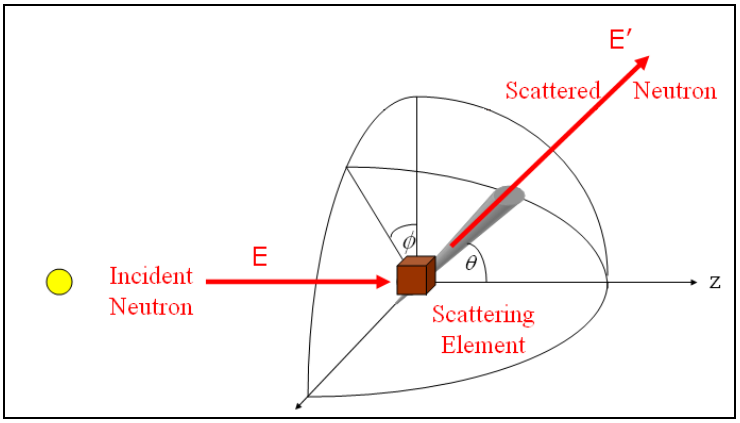

Fig. 1-4. Schematic of a neutron scattering event. The scattering element could be a single atom or a finite piece of a many-atom system. For the purpose of defining the cross section, it is assumed that only one interaction per neutron occurs in the element.

The quantity of interest is the probability that a neutron of incident energy *E* will scatter into a solid angle dΩ about Ω with a final energy of *dE'* about *E'*, where, in the notation of Fig. 1-4:

$$d\Omega = \sin\phi d\theta d\phi \tag{1.5}$$

This probability is contained in the *double differential scattering cross section*, defined as:

$$\frac{d\sigma}{d\Omega dE'} = \frac{N_s}{\phi d\Omega dE'} \tag{1.6}$$

where N_s is the number of neutrons scattered per unit time into dΩ about Ω with a final energy of *dE'* about *E'*. From the definition, it follows that:

$$\frac{d\sigma}{dE'} = \int \frac{d\sigma}{d\Omega dE'} d\Omega \propto \text{probability of scattering into dE' about E', regardless of } \Omega$$

$$\frac{d\sigma}{d\Omega} = \int \frac{d\sigma}{d\Omega dE'} dE' \propto \text{probability of scattering into } d\Omega \text{ about } \Omega, \text{ regardless of } E'$$

$$\sigma = \int \frac{d\sigma}{d\Omega dE'} d\Omega dE' \propto \text{probability of scattering}$$

If the scattering event causes no change in the total kinetic energy, the scattering is labeled *elastic.* If, in addition, *E = E'*, then only the direction of propagation of the incident neutron is altered. When the total kinetic energy is not conserved, the scattering is *inelastic* and some form of excitation or de-excitation has occurred in the scattering system. A variety of physical phenomena can lead to excitation, including but not limited to phonon emission, phonon absorption, and nuclear excitation (at higher energies). At low neutron energies (below about 1 eV), thermalization transpires through inelastic processes only.

1.4 Thermal Scattering Cross Section of Graphite

1.4.1 Overview of Thermal Scattering

When the incident energy of a neutron falls below approximately 1 eV, the atomic structure of a material exerts an appreciable influence on the scattering properties of the neutron. The reason is twofold: first, the neutron energy coincides with vibrational (phonon) energies of atoms in the crystal structure; second, the wavelength of the neutron is on the same order as the interatomic distances of the constituent atoms. Therefore, the neutron can be viewed as scattering from the collective structure rather than from any individual atom. The typical behavior of the cross section in the thermal scattering regime is illustrated in Fig. 1-5.

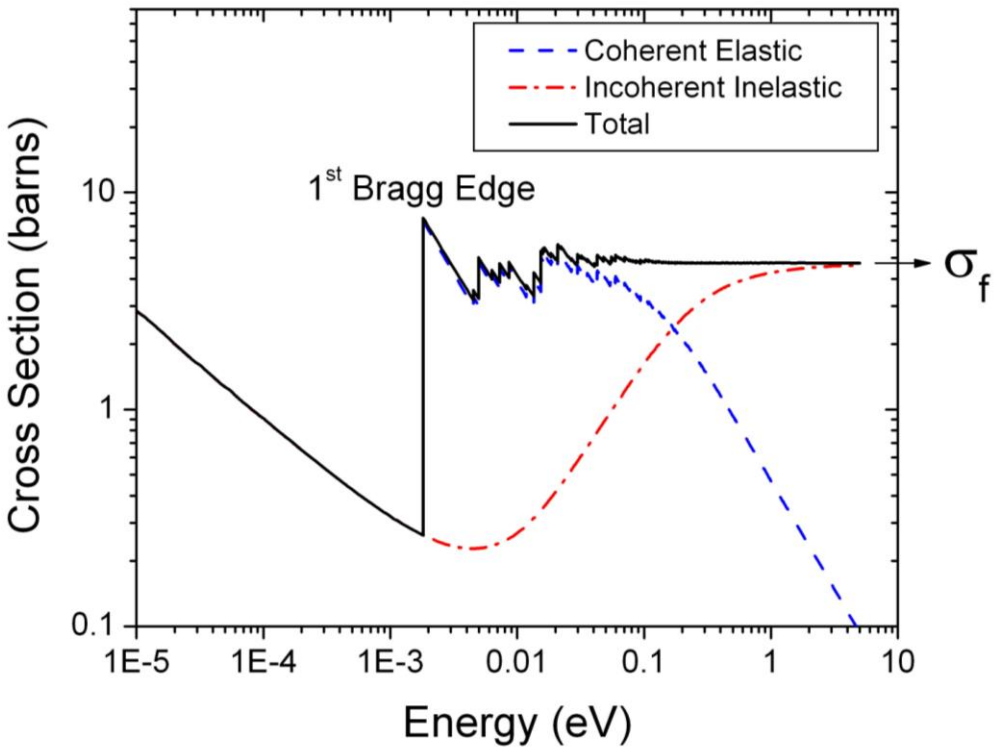

Fig. 1-5. The neutron scattering cross section at thermal energies.

The underlying mechanisms of thermal scattering fall into two broad categories. ***Elastic*** scattering can occur when the wavelength of the incident neutron satisfies Bragg's diffraction law, given by:

$$n\lambda = 2d\sin\theta \tag{1.7}$$

where n is an integer, λ is the neutron wavelength, d is the spacing between atomic planes, and θ is the angle between the neutron and the scattering plane. Clearly, Bragg's law yields a meaningful solution only in the case that $\sin\theta \leq 1$, thereby putting a lower bound on the neutron energy at which coherent elastic scattering is possible. For graphite, this minimum energy is about 2 meV and coincides with an abrupt spike in the cross section, apparent in Fig. 1-5 near the minimum point of the inelastic cross section curve. Coherent elastic scattering is not directly relevant to the thermalization process because only the direction of neutron propagation is affected. Therefore, this component of the cross section will be disregarded in the present work. Incoherent elastic scattering is important only for hydrogenous solids and will likewise be disregarded.

Inelastic processes occur throughout the entire range of thermal neutron energies. Generally, these involve the exchange of one or more phonons between the neutron and lattice; phonon absorption (de-excitation) is dominant at low incident energies while phonon emission (excitation) is responsible for the main contribution at high energies. Inelastic energy exchange can include both a coherent and an incoherent component, with the relative proportion depending upon the structural arrangement and intrinsic scattering lengths of the

atoms. The scattering length of carbon-12 is overwhelmingly coherent and, consequentially, both mechanisms are important in graphite.

In the high energy limit – where the neutron wavelength becomes much smaller than the interatomic spacings – scattering interactions are well described by an elastic "billiard ball" model and the specific distribution of phonons is no longer important. Hence, the scattering cross section of any material approaches the free atom cross section in this limit, which demarcates the boundary between the thermal and epithermal regimes.

1.4.2 Graphite Cross Section Calculations

Presently, the standard approach to thermal cross section generation is to invoke approximations such that the double differential scattering cross section is reduced to an analytic function of the vibrational (phonon) density of states, $\rho(\omega)$. The LEAPR module of the NJOY code [9], for example, follows this methodology. If one chooses to work within the LEAPR framework, the main issue becomes the accurate determination of the density of states.

In the early days of thermal library creation, $\rho(\omega)$ was often inferred by fitting the interatomic force constants to known material properties such as the heat capacity, bulk modulus or dispersion relation. This approach suffers from two deficiencies: first, there is the theoretical possibility that multiple $\rho(\omega)$ trial functions could fit the same set of experimental data;

second, the fitting method is not predictive because the quantity of interest is forcibly conformed to measured data, rather than being constituted independently and then validated against measured data.

With improvements in computational power, it is now feasible to evaluate thermal cross sections through atomistic simulation. Recently, $\rho(\omega)$ has been calculated to high fidelity using the interatomic force constants obtained from *ab-initio* simulation. Because the details of interatomic interaction are treated quantum mechanically in *ab-initio*, no specific analytical model is needed to discern the force constants. Consequently, the empiricism of the earlier methods is avoided to a large extent.

Ab-initio based phonon distributions have been used to produce thermal scattering libraries for a wide range of materials (e.g. in [10]-[13]) and were found to generate good agreement against experimental heat capacity and cross section data. The scattering cross section of graphite, in particular, has been investigated extensively using *ab-initio* techniques [12],[14]. As shown in Fig. 1-6, the cross section calculated from the *ab-initio* $\rho(\omega)$ agrees quite closely with measured data once the 1-phonon coherent inelastic component is included. The ENDF/B-VII standard libraries, by comparison, are based on the Young-Koppel density of states [15], which was obtained by fitting force constants to the specific heat of graphite between 100 K and 1000 K. Coherent inelastic effects are absent from all ENDF/B-VII cross section libraries.

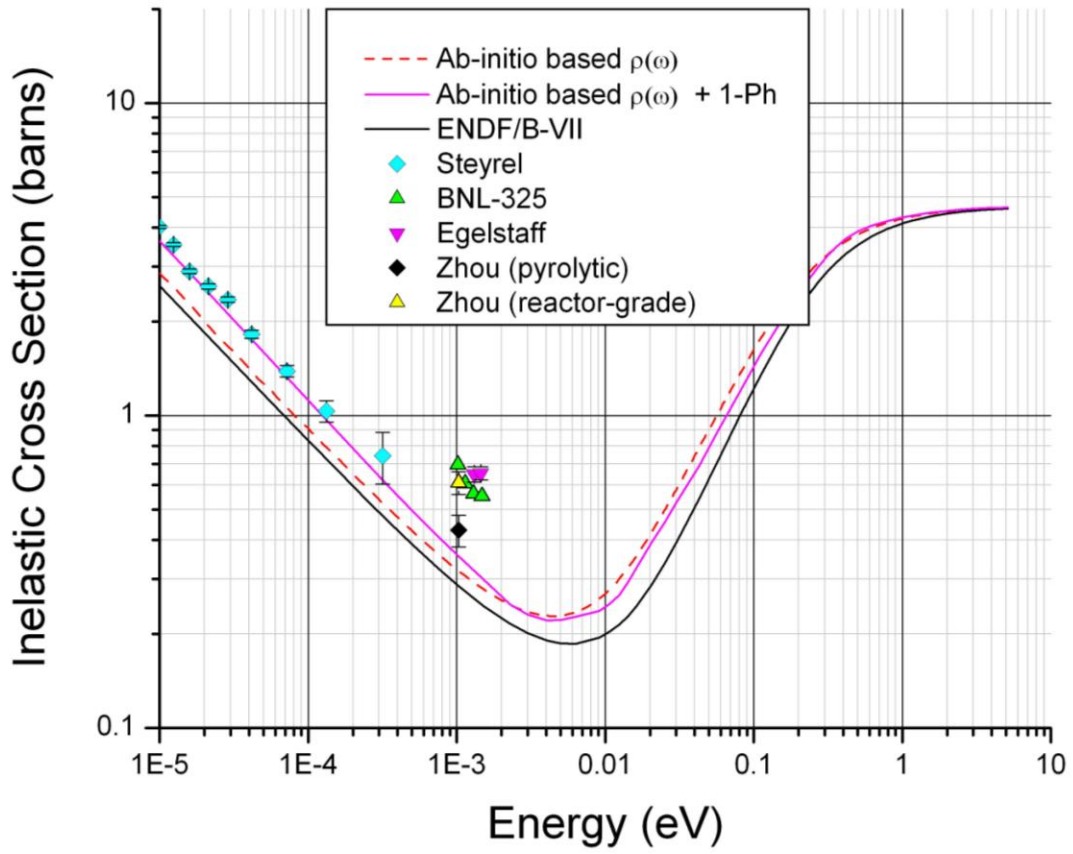

Fig. 1-6. Comparison of the calculated thermal inelastic scattering cross section of graphite at 300 K, including 1-phonon coherent effects [14], versus measured data from Steyrel [16], Egelstaff [17], BNL [18], and Zhou [19],[20]. Triangles correspond to reactor-grade graphite while diamonds indicate pyrolytic graphite.

Noting the segregation of the experimental cross section data into two distinct clusters based on microstructure (pyrolytic vs. reactor-grade), one may observe that the total inelastic scattering cross section of reactor-grade is substantially higher than that of pyrolytic at 1E-3 eV. Since reactor-grade graphite contains multiple phases that differ in interatomic binding, disparities are indeed anticipated in the total cross section, as well as in the details of the differential energy spectra.

To summarize, the current state of knowledge regarding inelastic thermal neutron scattering in graphite is as follows:

- Coherent and incoherent effects are both significant, with coherent inelastic scattering comprising as much as 20–25 % of the room-temperature cross section between 1E-5 and 5 eV.
- The total inelastic scattering cross section of reactor-grade graphite is about 70% larger than that of pyrolytic graphite at 1E-3 eV. Differences are expected in the differential energy spectra as well.

1.5 Motivation and objective

As discussed in the previous section, the thermal scattering cross section of perfect, crystalline graphite has been investigated and benchmarked using *ab-initio*. While the thermal scattering impact of single and di-interstitial defects has also been explored using static *ab-initio* simulation [21], the consequences of heavy irradiation and realistic defect formations have not yet been examined computationally. This is due partly to the loss of symmetry that accompanies irradiation defects or imperfections, and partly to the difficulty of modeling complex defect clusters using a time-independent structural optimization approach. Specifically, for atomistic simulation techniques such as *ab-initio* that rely on crystallographic symmetry to computationally simplify the interatomic force calculations, the

presence of defects can result in a many-fold increase in the cost of evaluating the cross section, particularly when the simulated system is large. Size limitations are especially detrimental to irradiation studies since a large supercell is typically needed to observe properly the defect formation processes that arise during high-energy displacement cascades. In the case of time-independent *ab-initio* simulation, an initial guess of the defect structure would be required as input because the simulation technique does not allow for dynamical evolution of the system.

In contrast to the static *ab-initio* approach, classical molecular dynamics (MD) simulations run just as efficiently with imperfections as without, and are also suitable for dynamically modeling the defect accumulation processes responsible for lattice damage in a reactor environment. Classical MD, based on a well established interatomic potential function, therefore presents a more predictive (and computationally less intensive) approach for analyzing changes in the material structure and properties due to cascade buildup. Furthermore, Fourier transform techniques can be utilized to evaluate the thermal neutron scattering cross section directly from the atomic positions, without necessarily invoking the approximations embedded in codes such as LEAPR. This is possible through the use of statistical time correlation functions, which serve as a link between fundamental microscopic variables and measurable material properties.

The objectives of this work are to investigate the thermal neutron scattering cross section of graphite using classical MD time correlation functions, and to initiate an examination of the

impact of cascade-induced damage on the cross section. As will be demonstrated in Chapter 3, achieving these objectives also entails the development of quantum corrections to the classical Van Hove functions.

Chapter 2

Molecular Dynamics

2.1 Overview

Molecular dynamics (MD) is a simulation technique in which an interacting atomic system is evolved for a specified period of time under the laws of classical physics. Two preconditions are necessary in order to operate in the classical framework, namely that:

(1) Atoms can be treated as point masses, the motions of which are governed by Newtonian mechanics.

(2) Electrons are instantaneously in equilibrium with nuclei.

Item (1) is valid when the thermal de Broglie wavelength is much smaller than interatomic spacings in the material. The thermal wavelength is inversely related to both mass and temperature, and so an increase in either quantity will improve the appropriateness of this condition. Item (2) is an excellent approximation due to the vast mass difference between electrons and atomic nuclei.

In the scheme of multiscale modeling that is illustrated in Fig. 2-1, MD corresponds to the nanoscale; that is, times on the order of nanoseconds and lengths on the order of nanometers are accessible in MD. On a larger scale lie the continuum methods, where the microscopic details of atomic motion are averaged and collapsed into macroscopic variables. This is the scale on which laboratory measurements and engineering design commonly take place. At

the smallest scale that is currently practicable, quantum methods and approximations such as density function theory (DFT) can be used to investigate the electronic structure in addition to the atomic motions.

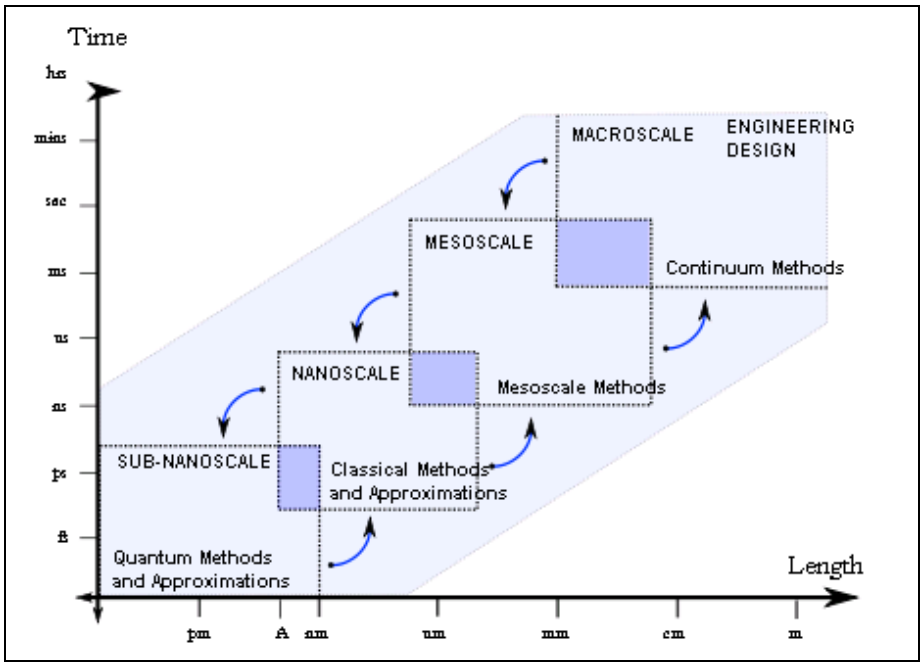

Fig. 2-1. Overview of multi-scale modeling

Some overlap exists between contiguous methods on the scale. For instance, the *ab-initio* MD technique combines DFT-based interatomic force calculations with the numerical time evolution algorithms and ensemble control of an MD simulation. One arrives at classical MD by invoking the Born-Oppenheimer approximation to collapse electronic interactions into a function that depends solely on the atomic positions. At a larger scale, the atomic positions and momenta from MD simulations can be converted into macroscopically observable material properties through Green-Kubo type relations [22]. In fact, taking a

holistic perspective on multi-scale modeling, it is apparent that macroscopic phenomena could, in principle, be modeled from the most basic equations of quantum mechanics with few intermediate approximations. Limitations in computational power severely restrict the viability of this ideal at present. Much of the cost lies in evaluating the potential energy function (or Hamiltonian) of the system, along with its associated derivatives.

2.2 Potential Function

2.2.1 Introduction

Atomic interactions are modeled in MD using an empirically fitted potential energy function, the form of which is grounded in the specific nature of the system. In general, the potential function may be written as an expansion over 1,2,3, … N-body terms as:

$$U = \sum_i V_1(\vec{r}_i) + \sum_i \sum_{i<j} V_2(\vec{r}_i, \vec{r}_j) + \sum_i \sum_{i<j} \sum_{i<j<k} V_3(\vec{r}_i, \vec{r}_j, \vec{r}_k) + \ldots \quad (2.1)$$

where the potential is labeled an N-body potential when the expansion is carried out to V_N.

Three-body or greater terms are generally needed to reproduce the physical properties of a covalent system accurately. An ionic system would require potential terms stemming from Coulombic effects as well as electronic binding, whereas certain liquid or solid state systems of noble gas atoms (e.g. argon) may only exhibit Van der Waals interactions, which can be represented with a simple 12-6 Lennard Jones formula [23].

Atomic interactions in graphite cannot be condensed into a simple 2-body potential. This is because the covalent interactions of graphite depend not only on the interatomic distances, but also on bond angles, torsional angles, and the coordination number. In other words, the potential energy is contingent upon the binding *environment*, and, for a given atom, the number of neighbor atoms affects the strength of each bond. It was this realization that led Abell [24] and later workers to develop the class of potentials known as *bond order potentials*. The theoretical basis for the bond order potentials lies in the derivation, from quantum mechanical equations, that:

$$E = \sum_k Z_k \left(q V_{Rk} + p_k V_{Ak} \right) \tag{2.2}$$

where E is the binding energy per atom, Z_k is the number of atoms in the k^{th}-neighbor coordination shell, p_k is the bond order term, q is the number of valence electrons per atom, and V_{Ak} and V_{Rk} are functions describing interatomic attraction and repulsion respectively. While the summation of Eq. (2.2) encompasses, in theory, all atoms within the system, it is common practice to limit this summation only to the first neighbor shell for reasons of computational efficiency (though the bond order term, p_k, may include contributions beyond the first shell). This restriction is known as the *nearest neighbor approximation*, and despite its seeming severity, it has been utilized successfully over the years to reproduce the observed physical properties of many systems. Analogously to density functional theory, the justification for the nearest neighbor approximation lies more in its proven utility rather than in any rigorous physical argument.

2.2.2 REBO Potential

The 2nd generation reactive empirical bond order (REBO) potential [25] is presently one of the most sophisticated potential functions available for hydrocarbons. As with the Abell [24] and Tersoff [26] potentials, interatomic interactions in REBO are modeled as a sum of attractive and repulsive terms where the attractive part is modified by a bond order function. Mathematically:

$$E = \sum_i \sum_{j>i} f_C\left(r_{ij}\right)\left[V_R\left(r_{ij}\right) + \bar{b}_{ij} V_A\left(r_{ij}\right)\right] \tag{2.3}$$

where V_R and V_A are pairwise repulsive and attractive functions, $\bar{b}_{ij}$ is the bond order term, r_{ij} is the scalar distance between atoms *i* and *j*, and $f_C\left(r_{ij}\right)$ is a cutoff function that smoothly attenuates the potential energy to zero beyond the first neighbor shell. The repulsive and attractive components are given by:

$$V_R = \left(1 + \frac{Q}{r_{ij}}\right) A \exp\left(-\alpha r_{ij}\right) \tag{2.4}$$

$$V_A = \sum_{n=1,3} B_n \exp\left(-\beta_n r_{ij}\right) \tag{2.5}$$

in which A, Q, α, B_n, and β_n are empirical fitting constants. The exponential form of these functions is derivable from quantum formulae, but the $\left(Q / r_{ij}\right)$ prefactor in V_R was included with the specific intent of preventing atoms from approaching each other too closely during a high-energy collision (noting that the exponential terms saturate to a constant as $r_{ij} \rightarrow 0$).

The bond order factor is comprised of four terms:

$$\bar{b}_{ij} = \frac{1}{2}\left[b_{ij}^{\sigma-\pi} + b_{ji}^{\sigma-\pi}\right] + \Pi_{ij}^{RC} + b_{ij}^{DH} \tag{2.6}$$

where $b_{ij}^{\sigma-\pi}$ and $b_{ji}^{\sigma-\pi}$ account for bond angles, Π_{ij}^{RC} is the bond conjugation term, and b_{ij}^{DH} represents the dihedral (torsional) contribution. The explicit forms of these functions are more intricate than the pairwise terms and are described in detail in the original paper [25]. The individual components of Eq. (2.6) share a common theme, however, in that each varies with the local atomic coordination number.

2.3 REBO corrections

Short-ranged empirical potentials are known to suffer from deficiencies that particularly impact anisotropic materials such as graphite. First and foremost is the absence of the long-ranged, interplanar Van der Waals interactions binding together graphite layers. Without an additional potential energy term to at least approximate the effects of these interactions, the graphite structure will be unstable.

This scenario is illustrated graphically in Fig. 2-2. Rather than remaining stationary, entire planes of atoms can drift along the a-b axes or oscillate along the c-axis. As will be demonstrated later, long-ranged interactions are also responsible for low-frequency lattice vibrations that significantly affect the thermal neutron scattering properties of graphite.

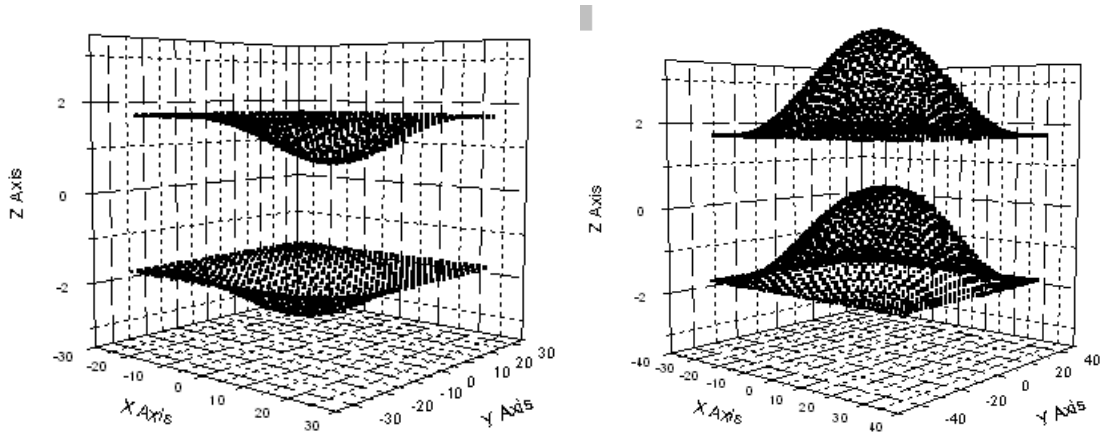

Fig. 2-2. Snapshots of an MD graphite supercell under the short-ranged REBO potential model. Distortion of the graphite planar structure occurs in the absence of long-range atomic interactions.

The REBO potential, being a generalized hydrocarbon potential, was fitted to the static (zero temperature) properties of a range of hydrocarbon systems. Because the fitting procedure was performed at 0 K, there is no guarantee that temperature-dependent properties of the MD system will conform to experimental data, and adjustments may be needed to achieve agreement. Adjustments to the REBO potential, as applied to graphite, are expected to include the implementation of a Van der Waals potential as well as corrections to the empirical fitting parameters.

2.3.1 Long Range Interactions

The structural effect of the long-ranged interactions is to maintain the rigid, layered arrangement of carbon atoms in graphite. Therefore, associated modifications to the REBO potential should work to counteract the bending of the layers that is obvious in Fig. 2-2. A straightforward approach is to add an explicit Van der Waals term, which ubiquitously takes the form of a Lennard-Jones potential:

$$V_{ij}^{LJ} = 4\varepsilon\left[\left(\frac{\sigma}{r_{ij}}\right)^{12} - \left(\frac{\sigma}{r_{ij}}\right)^{6}\right] \tag{2.7}$$

in which ε and σ are empirical parameters that specify the depth and position of the potential energy well. Stuart, Tutein, and Harrison have recommended values of ε = 0.00284 eV and σ = 3.4 Å for graphite [27], where σ is approximately equal to the interlayer spacing. This parameterization is used in the present work.

At short distances (e.g. between 1st or 2nd neighbor shells), the Lennard-Jones potential interferes with the covalent terms of REBO by generating a strong repulsive force between atoms. Thus, the L-J potential is modified by a smooth, "reverse" cutoff function that tapers off the long-ranged potential between 3.40 Å and 3.00 Å, with no long range component present below 3.00 Å. These limits were chosen so as to be inclusive of nearest- neighbor interplanar interactions at (0,0,+c/2) or (0,0,-c/2).

As in prior versions of the modified REBO potential [28] , the standard cutoff function is replaced with an anisotropic function, defined by:

$$f_c^{'}\left(r_{ij,}z,T\right) = f_c\left(r_{ij}\right) + f_c^{'}\left(z,T\right) \tag{2.8}$$

where:

$$f_c^{'}\left(z,T\right) = \frac{K\left[1-\cos\left(\frac{2\pi\ z}{\Delta d}\right)\right]}{2} \tag{2.9}$$

in which *K* is an empirical fitting parameter, *z* is the c-axis displacement, and Δd is the interlayer spacing. This modification, which is grounded in the anisotropy of the graphite

structure, enables regulation of the c-axis mean-squared displacement independently of the in-plane displacements. For small displacements along the c-axis, $f_c^{'}(z,T)$ brings about a parabolic increase in energy with respect to the displacement.

The parameter K was fitted to the out-of-plane mean squared displacement (MSD) for graphite, where the components of MSD are defined by:

$$MSD = \sqrt{MSD_{xy}^2 + MSD_z^2} = \left\langle \Delta^2 r \right\rangle = \frac{\sum_{t=T_o}^{T}\sum_{n=1}^{N}\left[\left|\vec{r}_n^{\,t} - \vec{r}_n^{\,0}\right|\right]^2}{(N)(T-T_o)} \tag{2.10}$$

in which r_n^t refers to the instantaneous displacement of particle *n* at time *t*, *N* is the total number of particles, T_o is the initial time step, T is the final time step, and (T-T_o) is the total number of time steps over which MSD is calculated.

Multiplying $f_c^{'}(z,T)$ through the pairwise attractive and repulsive terms gives a number with units of energy, and one would expect, on physical grounds, that:

$$f_c^{'}\left(\frac{\Delta d}{2},T\right)\left[V_R(r_{ij}) + \bar{b}_{ij}V_A(r_{ij})\right] \sim E_{\Delta d} \tag{2.11}$$

where $E_{\Delta d}$ is the interlayer binding energy of graphite, known experimentally to be about 50-60 meV/atom [29]. Optimization of K based on an initial guess from Eq. (2.11) results in a value of 0.003, which fits experimental MSD data quite well as shown in Fig. 2-3. The in-plane MSD is not significantly affected by $f_c^{'}(z,T)$, though it is, of course, influenced by $f_c(r_{ij})$.

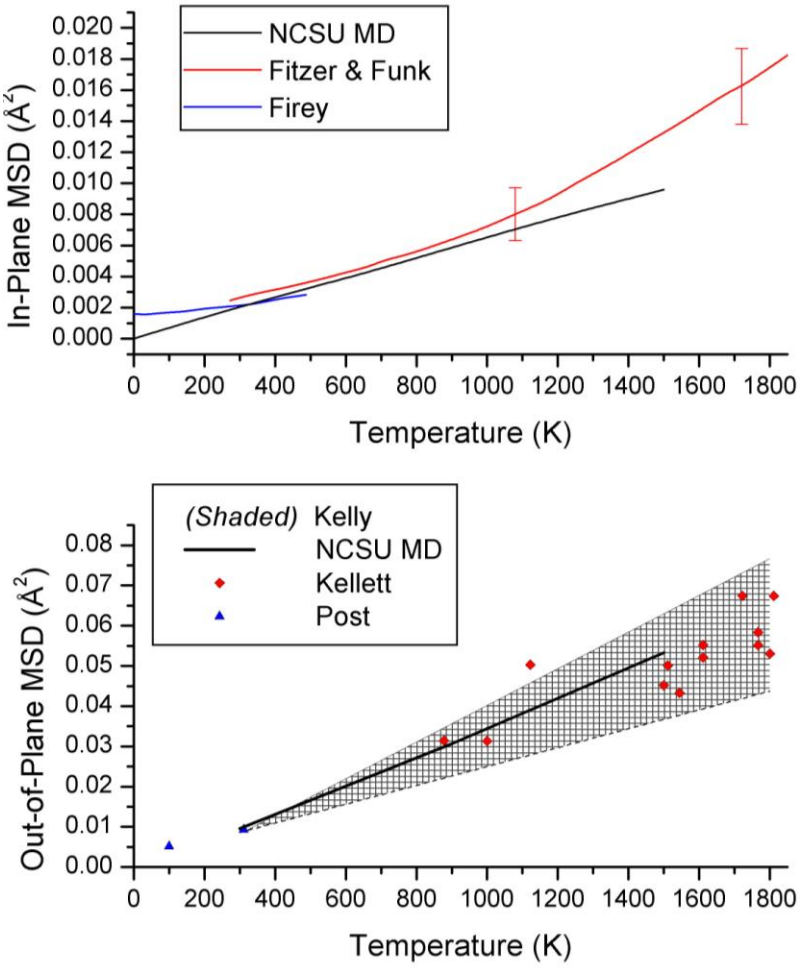

Fig. 2-3. In-plane (top panel) and out-of-plane (bottom panel) mean squared displacement in graphite. The in-plane MSD is compared against the x-ray diffraction measurements of Fitzer & Funk [30] and lattice dynamical calculations from Firey [31]. Out-of-plane MSD is shown alongside theoretical upper and lower bounds proposed by Kelly [32] as well as measurements performed by Kellet [33] and Post [34].

2.3.2 REBO pairwise adjustments

The second generation REBO potential, in its published form, is defined solely on the basis of distances, angles, and local coordination numbers. Parameterization of the potential was originally carried out by fitting to a set of physical properties (zero-point energy, bond

energy, bond distance, etc.) as determined for various hydrocarbon configurations. Notably, the fitting routine was limited to the static (0 K) properties of perfect lattices such that considerations of thermal motion were absent.

In the REBO formulation (and many others), a cutoff function limits interatomic interactions to the 1st neighbor shell. It is known, however, that 2nd neighbor atoms contribute significantly to the graphite potential. For example, Nicholson and Bacon [35] provide values for the principal force constants of the first two neighbor shells of graphite as listed in Table 2.1.

Table 2.1. Principal force constants of graphite in N/m, from Nicholson and Bacon

	1st shell	2nd shell
K_{11}	323.36	-33.533
K_{22}	279.95	91.44
K_{33}	231.95	-38.533

The 2nd neighbor force constants are roughly 10 – 33% of the magnitude of the corresponding 1st neighbor values, indicating that the 2nd neighbor interactions cannot be discounted. In practice, agreement between the REBO potential and measured physical data is achieved by effectively collapsing the 2nd, 3rd, … neighbor interactions into the 1st neighbor fitting parameters. Strictly speaking, such a parameterization is valid only if the influence of the longer-ranged interactions is temperature-invariant.

At nonzero temperatures, it is expected that thermal vibrations and lattice expansion would perturb the longer-ranged interactions. These perturbations can be addressed by introducing a temperature-dependent adjustment factor that is fitted to the thermal expansion coefficient. Essentially, an adjustment factor is applied to the pairwise coefficients as:

$$A(T) = A_o \exp\left[\alpha C(T) T\right] \tag{2.12}$$

$$B_n(T) = B_{n,o} \exp\left[\beta_n C(T) T\right] \tag{2.13}$$

which accounts for deficiencies in the ability of the nearest-neighbor potential to accurately model the true many-shell potential. Here, A_o and $B_{n,o}$ are the standard REBO pairwise coefficients and C(T) is a temperature-dependent adjustment factor, fitted to a sigmoidal function of the form:

$$C(T) = c_o + \frac{b}{1 + \exp\left[\dfrac{-(T - T_o)}{d}\right]} \tag{2.14}$$

in which c_o, b, d, and T_o are adjustable parameters. Using nonlinear least-squares regression (see [36] for more details), the parameter values shown in Table 2.2 were obtained, which correspondingly alter the thermal expansion behavior of the MD system to reflect the true expansion coefficient of graphite, as demonstrated in Fig. 2-4.

Table 2.2. Parameters for Sigmoidal Fit to C(T).

b	=	4.769E-06	Å/K
d	=	389.7	K
T_o	=	1410	K
c_o	=	-1.681E-06	Å/K

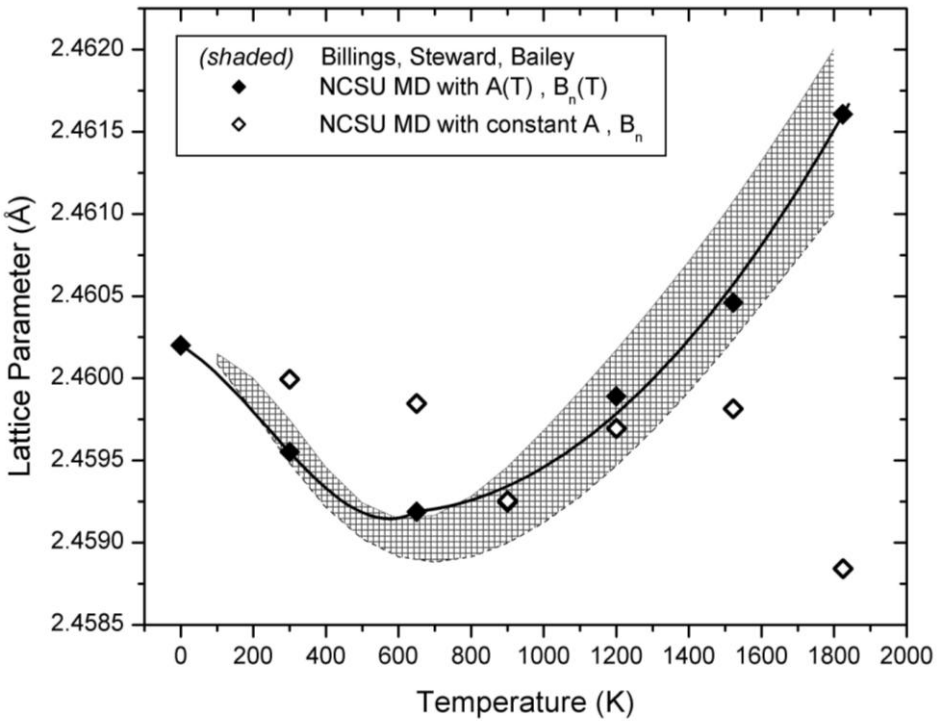

Fig. 2-4. Impact of pairwise REBO adjustment factors on thermal expansion. The shaded region represents the total span of measured data reported by Billings [37], Steward [38] and Bailey [39].

2.4 Correlation Functions

2.4.1 MD implementation

Correlation functions serve as the principal means by which material properties of relevance to engineering design can be related to the microscopic details of atomic motion. Aside from the thermal scattering correlation functions proposed by Van Hove, which constitute the foremost subject of development in the present work, there exists a class of *Green-Kubo* relations linking transport coefficients to the integrals of correlation functions. Green-Kubo

relations are discussed further in Appendix A, in conjunction with their application to the specific property of the in-plane thermal conductivity of graphite.

The correlation of two stochastic random variables $\boldsymbol{x}$ and $\boldsymbol{y}$ is defined, in general terms, by a phase space integral of the form [40]:

$$C_{xy^*}(t_1,t_2) = E\{\boldsymbol{x}(t_1)\boldsymbol{y}^*(t_2)\} = \int_{-\infty}^{\infty}\int_{-\infty}^{\infty} xy^* f(x,y;t_1,t_2)dxdy \tag{2.15}$$

where $\boldsymbol{x}$ and $\boldsymbol{y}$ are construed as ensembles of possible outcomes, $E\{\}$ is the expectation value, x and y represent trial outcomes, and $f(x,y;t_1,t_2)$ is the probability density of outcomes x and y occurring at times t_1 and t_2 respectively. The implementation of this somewhat abstract formula in the context of an MD simulation is elucidated by considering the statistical mechanical interpretation of MD. From that perspective, the state of the MD system at time t corresponds to a single point within the phase space of atomic positions $\{\vec{r}\}$ and momenta $\{\vec{p}\}$. As the system evolves in time, transitions continually occur from one state to another, and the system history forms an increasingly long path in phase space that stretches from the initial state to the final state. While the system may pass through any accessible phase space point, certain states are more probable than others and so the calculation of averaged quantities must be weighted appropriately (as by the density function, $f(x,y;t_1,t_2)$, of Eq. (2.15)).

Under the assumption of ergodicity, which is fundamental to the legitimacy of the MD method itself, the phase space average of Eq. (2.15) may be written as an equivalent time average of the form [41]:

$$C_{xy^*}(\tau) = \lim_{t\to\infty} \frac{1}{t} \int_0^t x(t) y^*(t+\tau) dt \tag{2.16}$$

where τ is referred to as the delay time. Technically, the upper integration limit must approach infinity to ensure that the time evolution of the MD system encompasses all possible phase space configurations. Because real simulations cannot be infinite in duration, the system is taken to be adequately sampled after some finite time interval that depends on the initial state and intrinsic material properties. MD simulations also progress in discrete time steps and Eq. (2.16) therefore reduces to:

$$C_{xy^*}(\tau) = \frac{1}{L(\tau)} \sum_{k=1}^{L(\tau)} x(t_k)\, y^*(t_k + \tau) \tag{2.17}$$

in which $L(\tau)$-- the number of steps available for averaging -- varies with the delay time. The relevant relationship is given by:

$$L(\tau) = L_{tot} - \frac{\tau}{t_k} \tag{2.18}$$

where L_{tot} is the total number of steps and τ must be an integer multiple of t_k. A corollary of Eq. (2.18) is that the statistical uncertainty in $C_{xy^*}(\tau)$ increases as a function of τ due to the linear drop in sample size. Hence, the time scale of the MD simulation may need to greatly exceed the characteristic time scale of the phenomenon under investigation, depending upon the desired degree of certainty.

The reader should be aware that correlation functions (in the present work and in general scientific literature) are often written using the following shorthand notation:

$$C_{xy} = f\left(\left\langle x(0)\, y(t)\right\rangle\right) \tag{2.19}$$

where $f\left(\left\langle x(0)\, y(t)\right\rangle\right)$ is defined as some function of the thermal average of the product $x(0)\cdot y(t)$. Two distinct features of Eq. (2.19) are noteworthy:

1. The time origin, $t = 0$, is arbitrary given that the system is in thermal equilibrium. Therefore, t actually refers to the delay time.
2. If the ergodic hypothesis holds, then the system is assumed to sample all accessible thermal states in its time evolution, and the thermal average, $\left\langle x(0)\, y(t)\right\rangle$, is wholly identical to the time average of Eq. (2.17).

2.4.2 Cross-Correlation Theorem

The calculation of correlation functions from Eq. (2.17) ordinarily entails on the order of N^2 operations. When the signal size is large (more than, say, $10^4 - 10^5$ points), this represents a significant computational burden, especially when multiple evaluations of the correlation function are required. Through implementation of the cross-correlation theorem, the number of operations can be reduced to *NlogN* with no loss in generality. As will be demonstrated later, cross section calculations can involve the computation of many thousands of correlation functions, and so the efficiency gain can be tremendous.

Extending Eq (2.16) into the negative time domain and replacing the variables in the integrand with their corresponding Fourier transform expressions:

$$x * y = \int_{-\infty}^{\infty} \left[\int_{-\infty}^{\infty} X(\omega) \exp(-2\pi i \omega t)\, d\omega \int_{-\infty}^{\infty} Y^*(\omega') \exp\left(2\pi i \omega' (t+\tau)\right) d\omega' \right] dt \tag{2.20}$$

where $x*y$ is the cross correlation of x and y, and X and Y are their Fourier conjugate variables. Combining the integrals on the RHS of Eq. (2.20),

$$\begin{aligned} x * y &= \int_{-\infty}^{\infty} \int_{-\infty}^{\infty} \int_{-\infty}^{\infty} X(\omega) Y^*(\omega') \exp(-2\pi i \omega t) \exp\left(2\pi i \omega' (t+\tau)\right) d\omega\, d\omega'\, dt \\ &= \int_{-\infty}^{\infty} \int_{-\infty}^{\infty} X(\omega) Y^*(\omega') \exp(2\pi i \omega' \tau) \left[\int_{-\infty}^{\infty} \exp\left(2\pi i t (\omega' - \omega)\right) dt \right] d\omega\, d\omega' \\ &= \int_{-\infty}^{\infty} \int_{-\infty}^{\infty} X(\omega) Y^*(\omega') \exp(2\pi i \omega' \tau) \delta(\omega' - \omega)\, d\omega\, d\omega' \\ &= \int_{-\infty}^{\infty} X(\omega) Y^*(\omega) \exp(2\pi i \omega \tau)\, d\omega \end{aligned} \tag{2.21}$$

which is simply the inverse Fourier transform of the product of the individual transforms of x and y. If $x = y$, then Eq. (2.21) is equivalent to the Wiener-Khinchin theorem:

$$x * x = \int_{-\infty}^{\infty} \left| X(\omega) \right|^2 \exp(2\pi i \omega \tau)\, d\omega \tag{2.22}$$

which yields the autocorrelation of x.

Chapter 3

Thermal Neutron Scattering

3.1 Theory

3.1.1 Derivation from First Principles

In the thermal scattering regime, the neutron and scattering system both must be treated quantum mechanically. This is true because the wave properties of the neutron influence the scattering phenomenon (as is most obvious in coherent scattering), and also because the phonon energy exchange between the neutron and lattice is discretized in accordance with the energy levels of a network of quantum harmonic oscillators.

The state of the neutron is given by the Schrödinger equation [42]:

$$i\hbar\frac{\partial\psi(\vec{r},t)}{\partial t} = -\frac{\hbar}{2M}\nabla^2\psi(\vec{r},t) + V(\vec{r},t)\psi(\vec{r},t) \tag{3.1}$$

where $V(\vec{r},t)$ is the potential and $\psi(\vec{r},t)$ is the wave function, the square of which is proportion to the probability of finding the particle at location $\vec{r}$ at time *t*. It can be shown that the wave function of a free particle (such as a traveling neutron), for which $V(\vec{r},t)$ = 0, is given by:

$$\psi_{free}(\vec{r},t) = \frac{1}{(2\pi)^{3/2}}\exp\left(i\vec{k}\cdot\vec{r} - i\omega t\right) \tag{3.2}$$

where *k* is the wave vector. The state of the scattering system, $\lambda(\vec{r},t)$, is also governed by the Schrödinger equation; in the time-independent case this becomes a partial differential eigenvalue equation over 3(N+N_e) variables, where *N* and N_e and the number of nuclei and electrons respectively. Solving $\lambda(\vec{r})$ for a system of interacting atoms is the subject of the *ab-initio* technique and density functional theory, in which the dimensionality of the problem is reduced considerably through a series of approximations. In general, however, the evaluation of $\lambda(\vec{r},t)$ is an intractable endeavor that, for the purposes of the present work, shall be deemed surmountable only in principle.

Interaction between the neutron and scattering system alters the physical state of both entities, and the neutron scattering process can be conceptualized in terms of a differential cross section [43]:

$$\left(\frac{d\sigma}{d\Omega}\right)_{\lambda\to\lambda'} = \frac{1}{\Phi d\Omega}\sum_{\vec{k}'} W_{\vec{k},\lambda\to\vec{k}',\lambda'} \tag{3.3}$$

that is proportional to the probability of transitioning from state $|\vec{k},\lambda\rangle$ to the set of states $|\vec{k}',\lambda'\rangle$, where $\vec{k}'$ is constrained to lie within the solid angle dΩ. If the transition matrix, *W*, is defined as the number of transitions occurring from $|\vec{k},\lambda\rangle$ to $|\vec{k}',\lambda'\rangle$ per second, then the incident flux, Φ, appears as the normalization factor that renders Eq. (3.3) an intrinsic property. An analytic expression for *W* may be obtained by invoking Fermi's Golden Rule, which states that:

$$\sum_{\vec{k}'} W_{\vec{k},\lambda\to\vec{k}',\lambda'} = \frac{2\pi}{\hbar}\rho_{k'}\left|\left\langle \vec{k}'\,\lambda'\middle|V\middle|\vec{k}\,\lambda\right\rangle\right|^2 \tag{3.4}$$

$$= \int \psi_{k'}^{*}\chi_{\lambda}^{*} V \psi_k \chi_\lambda d\vec{r} d\vec{R}_1 d\vec{R}_2 ... d\vec{R}_N$$

where V is the nuclear potential acting on the neutron and $\rho_{k'}$ is the density of momentum states at *k*' about dΩ. To proceed further, an explicit expression for the neutron-nucleus potential is needed. The neutron, being an uncharged particle, interacts with the nucleus through the strong nuclear force, which is negligible beyond femtometer-scale separations. It is reasonable, therefore, to represent the potential as a delta function centered about the position of the nucleus as:

$$V(\vec{r}) = a\delta(\vec{r}) \tag{3.5}$$

where, for a single fixed nucleus, the constant *a* is given by the exact expression:

$$V(\vec{r}) = \frac{2\pi\hbar^2 b}{m}\delta(\vec{r}) \tag{3.6}$$

in which *b*, the scattering length, is a property of the nucleus that depends primarily on the details of the actual neutron-nucleus potential. The scattering length exhibits almost no systematic correlation with atomic number or mass number, and its value may be considered constant in the thermal scattering regime – a consequence of the extremely short-ranged nature of the potential. The form of the potential given in Eq. (3.6) is referred to as the *Fermi pseudopotential*, and its justification follows from the fact that, in conjunction with Fermi's Golden Rule, the necessary outcome of isotropic scattering is obtained for a single fixed nucleus.

Combining the results of Eqs. (3.3)- (3.6), the differential cross section becomes:

$$\left(\frac{d\sigma}{d\Omega}\right)_{\lambda\to\lambda'} = \frac{k'}{k}\left|\sum_j b_j \left\langle \lambda' \left| \exp\left(i\vec{\kappa}\cdot\vec{R}_j\right) \right| \lambda \right\rangle\right|^2 \tag{3.7}$$

where $\kappa = k' - k$ is the change in the neutron wave vector due to scattering. Extension of this formula to the double differential cross section is straightforward – the energy of the scattering system plus neutron must be conserved during the scattering process; that is,

$$E_\lambda + E_k = E_{\lambda'} + E_{k'} \tag{3.8}$$

and the conservation of energy condition may be introduced as a delta function:

$$\left(\frac{d^2\sigma}{d\Omega dE'}\right)_{\lambda\to\lambda'} = \frac{k'}{k}\left|\sum_j b_j \left\langle \lambda' \left| \exp\left(i\vec{\kappa}\cdot\vec{R}_j\right) \right| \lambda \right\rangle\right|^2 \delta\left(E_{\lambda'} + E_{k'} - E_\lambda - E_k\right) \tag{3.9}$$

which is automatically normalized over energy. Now, at any given time, a realistic scattering system exists in one of many possible states (i.e. assumes one of an *ensemble* of states that are all consistent with the relevant conservation conditions). A well-known result of statistical mechanics [44] is that, at a constant temperature *T*, the probability of finding the system at energy E_λ is:

$$p_\lambda = \frac{\exp\left(E_\lambda / k_B T\right)}{Z} = \frac{\exp\left(E_\lambda / k_B T\right)}{\sum_\lambda \exp\left(E_\lambda / k_B T\right)} \tag{3.10}$$

where *Z* is the partition function. Converting the delta function of Eq. (3.9) to integral form through the relation:

$$\delta\left(E_{\lambda'} + E_{k'} - E_\lambda - E_k\right) = \frac{1}{2\pi\hbar}\int_{-\infty}^{\infty} \exp\left[\frac{i\left(E_{\lambda'} - E_\lambda\right)t}{\hbar}\right] \exp\left(-i\omega t\right) dt \tag{3.11}$$

and noting that:

$$\exp\left[\frac{-iE_\lambda t}{\hbar}\right]|\lambda\rangle = \exp\left[\frac{-i\hat{H}t}{\hbar}\right]|\lambda\rangle \tag{3.12}$$

where $\hat{H}$ is the Hamiltonian of the scattering system, the double differential cross section may be condensed into the following useful form:

$$\frac{d^2\sigma}{d\Omega dE'} = \frac{k'}{2\pi\hbar k}\sum_{j,j'} b_j b_{j'} \int_{-\infty}^{\infty} \left\langle \exp\left[-i\vec{\kappa}\cdot\vec{R}_{j'}(0)\right]\exp\left[i\vec{\kappa}\cdot\vec{R}_j(t)\right]\right\rangle \exp(-i\omega t)dt \tag{3.13}$$

with the atomic positions now defined as Heisenberg operators of the form:

$$\vec{R}_j(t) = \exp\left(\frac{i\hat{H}t}{\hbar}\right)\vec{R}_j \exp\left(\frac{-i\hat{H}t}{\hbar}\right) \tag{3.14}$$

in which the details of the scattering system are confined to the position operator and scattering lengths. Significantly, the nuclear component of the differential cross section has been separated completely from the lattice dynamical component. This consequence of the Fermi pseudopotential approximation enables one to speak of thermal neutron scattering in terms of the dynamics of the scattering system.

The fundamental implication of Eq. (3.13) is that the double differential cross section is derivable from the time-dependent atomic positions of the scattering system. It should be emphasized that the position vectors of Eq. (3.13) are, in fact, quantum mechanical operators that do not directly correspond to the classical atomic positions. This constitutes the primary obstacle in linking Eq. (3.13) to classical MD trajectories.

Assuming that the system of interest contains a large number of nuclei, which is nearly always true in practice, the scattering length product may be substituted with a corresponding averaged value:

$$b_j b_{j'} \to \langle b_j b_{j'} \rangle$$

and, if no correlations exist among the scattering lengths of different nuclei, then:

$$\langle b_j b_{j'} \rangle = \langle b_j \rangle \langle b_{j'} \rangle = \langle b \rangle^2 \qquad \text{if } j' \neq j \tag{3.15}$$

$$\langle b_j b_{j'} \rangle = \langle b^2 \rangle \qquad \text{if } j' = j \tag{3.16}$$

thereby causing Eq. (3.13) to split into two terms:

$$\frac{d^2\sigma}{d\Omega dE'} = \frac{k'}{2\pi\hbar k}\langle b \rangle^2 \sum_{j,j'} \int_{-\infty}^{\infty} \left\langle \exp\left[-i\vec{\kappa}\cdot\vec{R}_{j'}(0)\right] \exp\left[i\vec{\kappa}\cdot\vec{R}_j(t)\right] \right\rangle \exp(-i\omega t) dt \tag{3.17}$$

$$+\frac{k'}{2\pi\hbar k}\left(\langle b^2 \rangle - \langle b \rangle^2\right) \sum_{j} \int_{-\infty}^{\infty} \left\langle \exp\left[-i\vec{\kappa}\cdot\vec{R}_j(0)\right] \exp\left[i\vec{\kappa}\cdot\vec{R}_j(t)\right] \right\rangle \exp(-i\omega t) dt$$

Now, defining $\sigma_{coh} = 4\pi \langle b \rangle^2$ and $\sigma_{inc} = 4\pi\left(\langle b^2 \rangle - \langle b \rangle^2\right)$, the two terms on the RHS are seen to correspond to the coherent and incoherent cross section respectively:

$$\left(\frac{d^2\sigma}{d\Omega dE'}\right)_{coh} = \frac{\sigma_{coh} k'}{2\pi\hbar k} \sum_{j,j'} \int_{-\infty}^{\infty} \left\langle \exp\left[-i\vec{\kappa}\cdot\vec{R}_{j'}(0)\right] \exp\left[i\vec{\kappa}\cdot\vec{R}_j(t)\right] \right\rangle \exp(-i\omega t) dt \tag{3.18}$$

$$\left(\frac{d^2\sigma}{d\Omega dE'}\right)_{inc} = \frac{\sigma_{inc} k'}{2\pi\hbar k} \sum_{j} \int_{-\infty}^{\infty} \left\langle \exp\left[-i\vec{\kappa}\cdot\vec{R}_j(0)\right] \exp\left[i\vec{\kappa}\cdot\vec{R}_j(t)\right] \right\rangle \exp(-i\omega t) dt \tag{3.19}$$

in which the incoherent part involves only the (self) correlation between the position of an atom at $t = 0$ and the position of the same atom at a later time. The coherent part accounts for

self correlations in addition to correlations among all of the distinct atomic pairs in the system.

3.1.2 Thermal Scattering Correlation Functions

Defining the *intermediate scattering function* as:

$$I(\kappa,t)=\frac{1}{N}\sum_{j,j'}\left\langle \exp\left[-i\vec{\kappa}\cdot\vec{R}_{j'}(0)\right]\exp\left[i\vec{\kappa}\cdot\vec{R}_{j}(t)\right]\right\rangle \tag{3.20}$$

and further defining the *scattering law*, or *dynamic structure factor*, as the time Fourier transform of the intermediate function:

$$S(\kappa,\omega)=\frac{1}{2\pi\hbar}\int_{-\infty}^{\infty}I(\kappa,t)\exp(-i\omega t)\,dt \tag{3.21}$$

Eqs. (3.18) and (3.19)can be expressed as:

$$\left(\frac{d^2\sigma}{d\Omega dE'}\right)_{coh}=\frac{\sigma_{coh}k'}{k}S(\kappa,\omega) \tag{3.22}$$

$$\left(\frac{d^2\sigma}{d\Omega dE'}\right)_{inc}=\frac{\sigma_{inc}k'}{k}S_s(\kappa,\omega) \tag{3.23}$$

with the total cross section equal to:

$$\left(\frac{d^2\sigma}{d\Omega dE'}\right)=\frac{k'}{k}\left[\sigma_{coh}S(\kappa,\omega)+\sigma_{inc}S_s(\kappa,\omega)\right] \tag{3.24}$$

where the scattering law has been divided into a self and distinct part as:

$$S(\kappa,\omega)=S_s(\kappa,\omega)+S_d(\kappa,\omega) \tag{3.25}$$

in which the self term (associated with incoherent effects) arise from the $j = j'$ portion of the summation while the distinct term (associated with coherent effects) arise from all $j \neq j'$ terms.

The inverse transform of Eq. (3.20) in position yields the *dynamic pair correlation* function:

$$G(\vec{r},t) = \frac{1}{(2\pi)^3}\int_{-\infty}^{\infty} I(\vec{\kappa},t)\exp\left(-i\vec{\kappa}\cdot\vec{r}\right)d\vec{\kappa} \tag{3.26}$$

$$= \frac{\hbar}{(2\pi)^3}\int_{-\infty}^{\infty} S(\vec{\kappa},\omega)\exp\left(-i\left(\vec{\kappa}\cdot\vec{r}-\omega t\right)\right)d\vec{\kappa}d\omega$$

which is specifiable in terms of measurable quantities and may be endowed with a simple physical interpretation in the absence of quantum effects. This is apparent from the full expression for $G(\vec{r},t)$:

$$G(\vec{r},t) = \frac{1}{N(2\pi)^3}\int_{-\infty}^{\infty}\exp\left(-i\vec{\kappa}\cdot\vec{r}\right)d\vec{\kappa}\left[\sum_{j,j'}\left\langle\exp\left[-i\vec{\kappa}\cdot\vec{R}_{j'}(0)\right]\exp\left[i\vec{\kappa}\cdot\vec{R}_{j}(t)\right]\right\rangle\right] \tag{3.27}$$

Combining the complex exponential terms and utilizing the integral form of the Dirac delta function, this formula reduces to:

$$G(\vec{r},t) = \frac{1}{N}\sum_{j,j'}\int_{-\infty}^{\infty}\left\langle\delta\left(\vec{r}-\vec{R}_{j'}(0)\right)\delta\left(\vec{r}\,'+\vec{r}-\vec{R}_{j}(t)\right)\right\rangle d\vec{r}\,' \tag{3.28}$$

and if the position operators $R_{j'}(0)$ and $R_{j}(t)$ are taken as the classical atomic positions (i.e. allowed to commute), then a straightforward integration of Eq. (3.28) gives:

$$G^{cl}(\vec{r},t) = \frac{1}{N}\sum_{j,j'}\left\langle\delta\left(\vec{r}+\vec{R}_{j'}(0)-\vec{R}_{j}(t)\right)\right\rangle \tag{3.29}$$

where, for each atom *j'*, $\left\langle \delta\left(\vec{r}+\vec{R}_{j'}(0)-\vec{R}_j(t)\right)\right\rangle$ is the probability that an atom *j* is located at position $\vec{r}$ at time t, given that the atom *j'* was initially at the origin. By extension, $\sum_j \left\langle \delta\left(\vec{r}+\vec{R}_{j'}(0)-\vec{R}_j(t)\right)\right\rangle$ is the probability of finding *any* atom at position $\vec{r}$ at time t, given an atom *j'* initially at the origin. This expression for G(r,t) can be defined so as to include all possible atomic combinations (resulting in G(r,t)), to include only $j \neq j'$ terms (resulting in $G_d(r,t)$), or allowing solely for $j = j'$ terms (resulting in $G_s(r,t)$).

Classical analogues of I(κ,t) and S(κ,ω) similarly follow by allowing the atomic positions to commute. The Fourier transform relations among G(r,t), I(κ,t) and S(κ,ω) are valid in both the classical and quantum cases. Significantly, G(r,t) and I(κ,t) are complex functions, whereas $G^{cl}(r,t)$ and $I^{cl}(\kappa,t)$ are always real. The complex nature of these functions serves to introduce asymmetry into S(κ,ω).

Physically, the scattering law may be conceptualized in terms of lattice waves. Associated with any solid-state array of atoms is a dispersion relation, ω(*k*), detailing the allowed frequencies of vibrational modes along wave vector *k*. S(κ,ω) is effectively proportional to the "weight" of these vibrational modes in relation to neutron scattering interactions. Thus, for a thermal neutron propagating through the material, the probability of scattering from wave vectors *k* to *k'*, with an accompanying energy exchange of $\hbar\omega$, is proportional to S(κ,ω).

In $S_s(\kappa,\omega)$, this weight is modulated by the *density* of allowed states (a property of the material structure) as well as the *occupancy* factor, which varies with the system temperature. For each atom in the system, both properties are determinable from the position of that individual atom as a function of time. $S_d(\kappa,\omega)$, on the other hand, includes interference effects from the correlated motions of atoms occupying different lattice sites. Thermal occupancy is still an important factor within $S_d(\kappa,\omega)$; however, there no explicit relationship between $S_d(\kappa,\omega)$ and the bulk density of states.

3.1.3 Symmetry Relations

From the properties of Fourier transforms, it can be shown that the classical scattering law is symmetric in ω and therefore fails to satisfy the detailed balance equation. Relations of detailed balance are, fundamentally, a product of microscopic reversibility at thermal equilibrium. For processes that alter the energy state of the system, detailed balance can be expressed mathematically as:

$$p(E)\, f(E \to E') = p(E')\, f(E' \to E) \tag{3.30}$$

where *p(E)* is the probability of state *E* and $f(E \to E')$ represents the transition probability (or rate) from states *E* to *E'*. In the thermal scattering of neutrons, phonons serve as the relevant vehicle of energy exchange. Therefore, *p(E)* can be identified as the Boltzmann factor, and $f(E \to E')$ becomes the scattering law associated with an energy exchange of *E'-E*. Here, the sign of the energy exchange indicates whether phonons have been *absorbed* or *emitted* by the neutron. Substituting the Boltzmann factor and scattering law into Eq.

(3.30), the detailed balance relation governing thermal neutron scattering processes is recognized to be:

$$S\left(\vec{\kappa},\omega\right)=\exp\left(\hbar\omega/k_BT\right)S\left(-\vec{\kappa},-\omega\right) \tag{3.31}$$

which, in terms of the Van Hove formula of Eq. (3.21), arises numerically through the balance between the real (symmetric) and imaginary (anti-symmetric) parts of the intermediate function, where the imaginary part is associated with quantum effects. The scattering law itself can be broken up into symmetric and anti-symmetric parts as:

$$\bar{S}\left(\vec{\kappa},\omega\right)=\int\exp\left(-i\omega t\right)I_R\left(\vec{\kappa},t\right)dt \tag{3.32}$$

$$\hat{S}\left(\vec{\kappa},\omega\right)=i\int\exp\left(-i\omega t\right)I_I\left(\vec{\kappa},t\right)dt \tag{3.33}$$

where $\bar{S}\left(\vec{\kappa},\omega\right)$ is the symmetric component and $\hat{S}\left(\vec{\kappa},\omega\right)$ is the antisymmetric component. These are related to the full scattering law by:

$$\bar{S}\left(\kappa,\omega\right)=\frac{1}{2}\left[1+\exp\left(-\frac{\hbar\omega}{k_BT}\right)\right]S\left(\kappa,\omega\right) \tag{3.34}$$

and:

$$\hat{S}\left(\kappa,\omega\right)=\frac{1}{2}\left[1-\exp\left(-\frac{\hbar\omega}{k_BT}\right)\right]S\left(\kappa,\omega\right) \tag{3.35}$$

Combining Eqs. (3.34) and (3.35) with the detailed balance condition gives:

$$\tilde{S}\left(\vec{\kappa},\omega\right)=\bar{S}\left(\vec{\kappa},\omega\right)\tanh\left(\frac{\hbar\omega}{2k_BT}\right) \tag{3.36}$$

Expanding the hyperbolic tangent, taking the inverse Fourier transform, and recombining the resulting terms, it can also be shown that:

$$I_I(\kappa,t) = \tan\left(\frac{\hbar}{2k_BT}\frac{d}{dt}\right) I_R(\kappa,t) \tag{3.37}$$

which is exact, given that I_R is the real part of the *quantum* intermediate function (and not simply the classical function). An important observation is that the real and imaginary parts of I(κ,t) are not independent, but rather are related in the manner prescribed in Eq. (3.37). This equation (categorized as a fluctuation-dissipation type relation) will prove useful later in the development of quantum corrections to the classical scattering functions.

3.1.4 Moment Rules

The scattering law obeys a series of moment rules of the form [43]:

$$S_n(\kappa) = \int_{-\infty}^{\infty} d(\hbar\omega) S(\kappa,\omega)(\hbar\omega)^n \tag{3.38}$$

where *n* is the moment order and, in general:

$$S_n(\kappa) = (-i\hbar)^n \left(\frac{\partial^n}{\partial t^n} I(\kappa,t)\right)\Big|_{t=0} \tag{3.39}$$

The two lowest order moments of the scattering law possess the unique property of being independent of the dynamics or structure of the scattering system. Namely, for incoherent scattering:

$$\int_{-\infty}^{\infty} d\omega S_s(\kappa,\omega) = 1 \tag{3.40}$$

and:

$$\int_{-\infty}^{\infty} d\omega \cdot \omega S_s(\kappa,\omega) = \frac{\hbar\kappa^2}{2M} \tag{3.41}$$

While, for the total scattering law (self + distinct):

$$\int_{-\infty}^{\infty} d\omega \cdot S(\kappa,\omega) = S(\kappa) \tag{3.42}$$

where S(κ) is the static structure factor. Strictly speaking, Eq. (3.41) is premised on the validity of the Born approximation as well as the velocity independence of the interatomic potential energy [45]. Both conditions are met in all situations considered in the present work. The first-order moment of the distinct scattering law is zero, and so Eq. (3.41) applies to the total function as well. The (always symmetric) classical scattering law also obeys the normalization rule of Eq. (3.40), but, of course, has no nonzero odd moments. Instead, the classical function conforms to a second-order relation of the form:

$$\int_{-\infty}^{\infty} d\omega \cdot \omega^2 S_s(\kappa,\omega) = \frac{k_B T \kappa^2}{M} \tag{3.43}$$

which is independent of $\hbar$, as must be true in the classical limit.

3.1.5 Differential Cross Section from S(κ,ω)

Once I(κ,t) is known, the scattering law follows from the transformation relation of Eq. (3.21), at which point S(κ,ω) has dimensions of time or, equivalently, inverse frequency. It is standard practice throughout much of the thermal scattering community to work with the dimensionless function S(α,β), where:

$$\alpha = \frac{\hbar^2\kappa^2}{2Mk_BT} = \frac{E'+E-2\sqrt{EE'}\mu}{Ak_BT} \tag{3.44}$$

$$\beta = \frac{\hbar\omega}{k_BT} = \frac{E'-E}{k_BT} \tag{3.45}$$

are the dimensionless momentum and energy transfer respectively [46], where μ is the cosine of the scattering angle. S(α,β) is related to the original scattering function through a simple scaling factor as:

$$S(\alpha,\beta) = \frac{k_BT}{\hbar} S(\kappa,\omega) \tag{3.46}$$

and the differential cross section is then succinctly expressible as:

$$\frac{d\sigma(E,E',\mu)}{dE'd\mu} = \frac{\sigma_b}{2k_BT}\sqrt{\frac{E'}{E}} S(\alpha,\beta) \tag{3.47}$$

By integrating the double differential cross section over μ and performing a transformation of variables, the single differential spectra are seen to be given by:

$$\frac{d\sigma(E,E')}{dE'} = \frac{\sigma_b A}{4E}\int_{\alpha_{\min}}^{\alpha_{\max}} S(\alpha,\beta)d\alpha \tag{3.48}$$

where *A* is the scatterer-to-neutron mass ratio and the limits of integration are:

$$\alpha_{\min} = \frac{E'+E-2\sqrt{EE'}}{Ak_BT} \tag{3.49}$$

$$\alpha_{\max} = \frac{E'+E+2\sqrt{EE'}}{Ak_BT} \tag{3.50}$$

Integrating Eq. (3.48) over all secondary energies yields the total inelastic scattering cross section:

$$\sigma(E) = \int_0^{\infty} \frac{d\sigma(E,E')}{dE'} dE' \tag{3.51}$$

which is readily determinable experimentally. It should be emphasized that the detailed dynamics of the scattering system are containing within S(α,β), and, as with all integral quantities, information is lost in moving from S(α,β) to σ(E,E') to σ(E). Benchmarking will therefore be carried out at all stages of the S(α,β) → σ(E) reduction.

3.2 Computational Methods

The standard methodology for evaluating the thermal neutron scattering cross section is to make use of the Gaussian and incoherent approximations to arrive at an analytic form of $S_s(\kappa,\omega)$. This is the procedure implemented in the LEAPR module of NJOY [9], for instance. The utility of this approach is that the scattering law is made solely dependent upon the phonon density of states, ρ(ω), with the detailed time evolution of the system being of no real consequence. Thus, the problem of calculating the scattering law is transformed into the simpler task of determining ρ(ω) accurately. Of course, since the incoherent approximation limits the calculation to $S_s(\kappa,\omega)$, coherent inelastic effects are intrinsically excluded. This is not a serious limitation for predominantly incoherent scatterers such as hydrogen, but certain atoms (including carbon) do exhibit strong coherent effects. In the specific case of graphite, coherent scattering is responsible for as much as 20 – 25 % of the thermal inelastic scattering cross section at room temperature.

Two distinct avenues exist for the computation of $S(\kappa,\omega)$ through MD simulation. In one, the density-density correlation function is evaluated from the (classical) time-dependent atomic positions, and important quantum effects are added through some imposed correction. In the other, $\rho(\omega)$ is extracted from the MD velocity autocorrelation function and $S_s(\kappa,\omega)$ follows after invoking the Gaussian and incoherent approximations. The proposed procedures are summarized in Fig. 3-1. By no means is the velocity autocorrelation function the only route to $\rho(\omega)$; alternatives will be discussed later in this section.

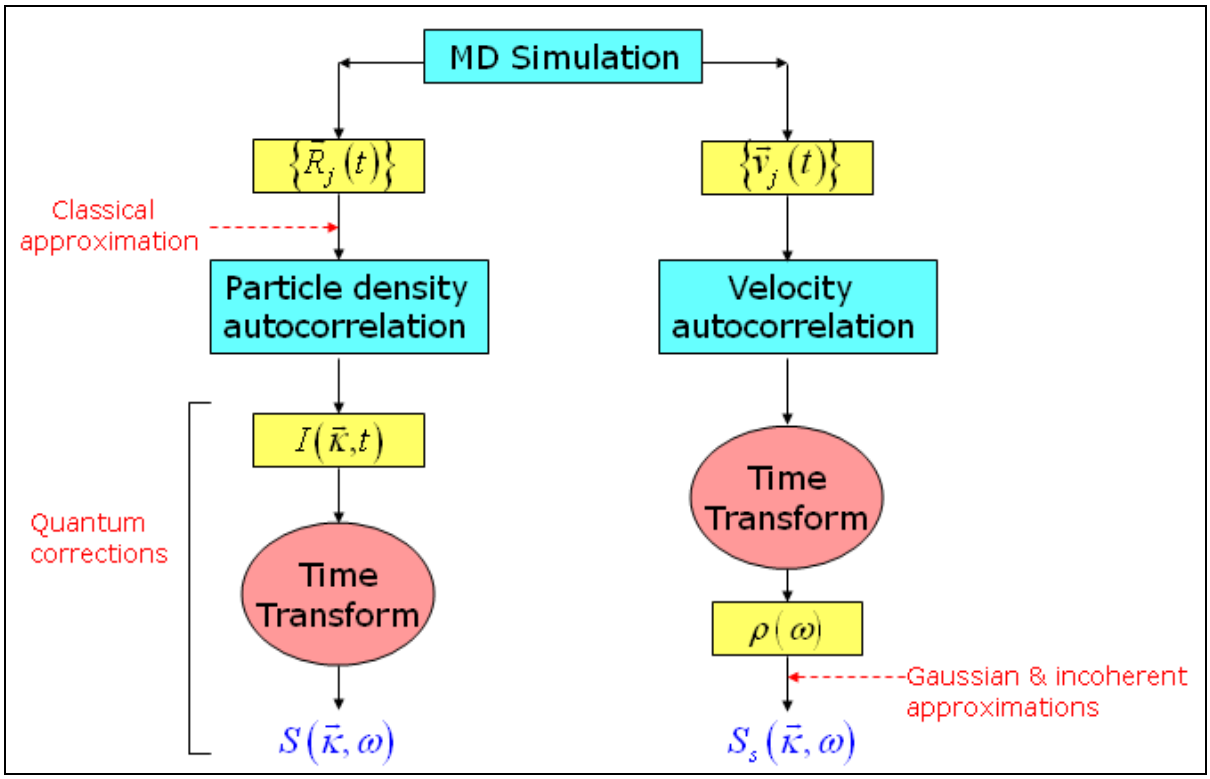

Fig. 3-1. Two approaches to computing $S(\kappa,\omega)$ from basic MD data

3.2.1 S(κ,ω) from ρ(ω)

Starting from the basic Van Hove relation:

$$S\left(\vec{\kappa},\omega\right)=\frac{1}{2\pi\hbar}\int_{-\infty}^{\infty}G\left(\vec{r},t\right)\exp\left(i\left(\vec{\kappa}\cdot\vec{r}-\omega t\right)\right)d\vec{r}dt \tag{3.52}$$

the goal is to express S(κ,ω) analytically as a function of ρ(ω). In many cases, the self part of the dynamic pair correlation function is well approximated by a Gaussian of the form:

$$G_s\left(\vec{r},t\right)=\frac{1}{\left(2\pi\sigma^2\left(t\right)\right)^{3/2}}\exp\left(\frac{-r^2}{2\sigma^2\left(t\right)}\right) \tag{3.53}$$

where $\sigma^2\left(t\right)$ is related to the mean squared displacement by:

$$\left\langle r^2\left(t\right)\right\rangle=3\sigma^2\left(t\right) \tag{3.54}$$

and no assumption has been made about how $\left\langle r^2\left(t\right)\right\rangle$ varies with time, which depends upon the state of matter of the system. In fact, Eq. (3.53) is valid for solids, liquids, or gases given that the Gaussian functional form is appropriate. It should be noted that the Gaussian approximation of $G_s\left(\vec{r},t\right)$ is rigorously correct for an ideal gas, or in the limit of extremely short or long times.

The Fourier transform of Eq. (3.53) over volume yields a simple analytical form for the intermediate function:

$$I_s\left(\kappa,t\right)=\exp\left(-\frac{\kappa^2\sigma^2\left(t\right)}{2}\right) \tag{3.55}$$

such that:

$$S\left(\vec{\kappa},\omega\right)=\frac{1}{2\pi\hbar}\int_{-\infty}^{\infty}dt\exp\left(-\frac{\kappa^2\sigma^2\left(t\right)}{2}\right)\exp\left(-i\omega t\right) \tag{3.56}$$

In order to proceed further, a closed expression for the mean-squared displacement is needed. To this end, it is assumed that the atoms comprising the scattering system behave as perfect harmonic oscillators for which:

$$\sigma^2\left(t\right)=\frac{\hbar}{M}\int_{0}^{\infty}d\omega\frac{\rho\left(\omega\right)}{\omega}\left[\coth\left(\frac{\hbar\omega}{2k_BT}\right)\left(1-\cos\left(\omega t\right)\right)-i\sin\left(\omega t\right)\right] \tag{3.57}$$

Since ρ(ω) is an even function of ω, the limits of integration can be extended to span the entire frequency domain, giving:

$$\sigma^2\left(t\right)=\frac{\hbar}{M}\int_{-\infty}^{\infty}d\omega\frac{\rho\left(\omega\right)\exp\left(\frac{\hbar\omega}{2k_BT}\right)}{2\omega\sinh\left(\frac{\hbar\omega}{2k_BT}\right)}\left[1-\exp\left(i\omega t\right)\right] \tag{3.58}$$

and therefore:

$$S\left(\vec{\kappa},\omega\right)=\frac{1}{2\pi\hbar}\int_{-\infty}^{\infty}dt\exp\left(-i\omega t\right)\cdot\exp\left(-\frac{\hbar\kappa^2}{2M}\int_{-\infty}^{\infty}d\omega\frac{\rho\left(\omega\right)\exp\left(\frac{\hbar\omega}{2k_BT}\right)}{2\omega\sinh\left(\frac{\hbar\omega}{2k_BT}\right)}\left[1-\exp\left(i\omega t\right)\right]\right) \tag{3.59}$$

which is equivalent to the form of S(κ,ω) implemented in LEAPR. Once ρ(ω) is known, the computation of S(κ,ω) becomes purely a mathematical exercise. The problem now hinges on the extraction of ρ(ω) from atomistic data, for which two well-established methodologies exist – diagonalization of the dynamical matrix and transformation of the velocity

autocorrelation function. A comparison of the relative merits of these approaches is reserved for Chapter 4.

3.2.1.1 Dynamical Matrix

One method of generating the frequency distribution is to evaluate the net forces arising from an appropriate set of static displacements. If one considers the system potential energy as a function of the instantaneous atomic positions:

$$\Phi = \Phi\left(\vec{r}_1, \vec{r}_2, \vec{r}_3, ..., \vec{r}_j\right) \tag{3.60}$$

then the potential energy can be expanded in terms of the displacements from equilibrium, *{u}*, as:

$$\Phi = \Phi_o + \sum_{l,d,\eta} \left.\frac{\partial \Phi}{\partial u_\eta\left(l,d\right)}\right|_{u_\eta(l,d)=0} u_{\eta(l,d)} \tag{3.61}$$

$$+\frac{1}{2}\sum_{\substack{l,d,\eta,\\ l',d',\theta}} \left.\frac{\partial^2 \Phi}{\partial u_\eta\left(l,d\right)\partial u_\theta\left(l',d'\right)}\right|_{\substack{u_\eta(l,d)=\\ u_\theta(l',d')=0}} u_\eta(l,d)u_\theta(l',d') \ + ...$$

where Φ_o is the potential energy of the unperturbed structure, η and θ denote Cartesian axes, *l* is the unit cell index, *d* is the atomic index (within the selected unit cell), and:

$$\Phi_{\eta\theta}\left(l,d;l',d'\right) = \left.\frac{\partial^2 \Phi}{\partial u_\eta\left(l,d\right)\partial u_\theta\left(l',d'\right)}\right|_{\substack{u_\eta(l,d)=\\ u_\theta(l',d')=0}} \tag{3.62}$$

is the force constant tensor acting between atoms *d* and *d'* of unit cells *l* and *l'* respectively.

Noting that the second term on the RHS of Eq. (3.61) is zero by definition of "equilibrium", and presupposing a plane wave solution, Newton's 2nd law can be used to show that:

$$u_\eta(l,d) = \frac{1}{\sqrt{M_d}} u_\eta(d) \exp\left[-i\left(\omega t - \vec{q}\cdot\vec{R}(l)\right)\right] \tag{3.63}$$

where M is mass, $u_\eta(d)$ is an amplitude independent of l, and **R**(l) is the position of unit cell l. With $\{u\}$ as given by Eq. (3.63), an eigenvalue equation of the form:

$$\omega_j^2(\vec{q})\vec{e}_{\eta dj}(\vec{q}) = \sum_{d',\theta} D_{\eta\theta}(\vec{q};d,d')\vec{e}_{\theta d' j}(\vec{q}) \tag{3.64}$$

exists between the eigenvectors $\vec{e}_{dj}$ and the eigenvalues ω_j, where the dynamical matrix, D, is defined by:

$$D_{\eta\theta}(\vec{q},d,d') = \frac{1}{\sqrt{M_d M_{d'}}} \sum_{l'} \Phi_{\eta\theta}(l,d;l',d') \exp\left[-i\vec{q}\cdot\left\{\vec{R}(l)-\vec{R}(l')\right\}\right] \tag{3.65}$$

and the phonon density of states is then taken as a histogram over the Brillouin zone of the crystal as:

$$\rho(\omega) = \int_{\vec{q}\in BZ} d\vec{q}\,\delta\left(\omega - \omega_j(\vec{q})\right) \tag{3.66}$$

which may be evaluated numerically through Monte Carlo sampling of reciprocal space vectors. As long as the system lacks crystallographic defects, only the basis atoms must be displaced because all other atoms are equivalent by symmetry. A*b-initio* simulation is quite feasible in this scenario and generally provides accurate phonon information. MD simulations produce analogous force data and are, therefore, entirely compatible with the dynamical matrix approach.

3.2.1.2 Velocity Autocorrelation Function

In situations where the system symmetry is broken (for example, by defects), the interatomic force constants are no longer determinable from a small number of displacements, and the dynamical matrix can become laborious to formulate. In principle, any defect reduces the system symmetry to P1 (the lowest-symmetry space group) such that every atom in the system must be displaced in order to construct the dynamical matrix. This would be tedious in MD and extremely costly in large-scale *ab-initio* simulations.

Fortunately, the frequency distribution is also extractable from the atomic trajectories at equilibrium, such that no artificial manipulations are necessary. The relevant function is the velocity autocorrelation function:

$$C(t) = \langle \vec{v}(0) \cdot \vec{v}(t) \rangle = \frac{1}{N} \sum_{j=1}^{N} \vec{v}_j(0) \cdot \vec{v}_j(t) \tag{3.67}$$

and its Fourier transform over time is proportional to the phonon frequency distribution as:

$$\rho(\omega) = \frac{M}{3\pi k_B T} \int_{-\infty}^{\infty} C(t) \exp(-i\omega t)\, dt \tag{3.68}$$

where $\vec{v}_j(t)$ is the velocity vector of atom *j* at time *t*. In signal processing terminology, the function C(t) is symmetric in time and the Fourier transform is therefore equivalent to the cosine transform, which returns a real function, ρ(ω), as output. Again, the time origin, t = 0, is arbitrary and C(t) should be averaged over all available origins. The computational cost of C(t) is independent of symmetry; therefore, the velocity autocorrelation function is an especially efficient vehicle for evaluating the phonon frequency distribution of a damaged

system. As a side note, the diffusion coefficient is proportional to the integral of the velocity autocorrelation function over all delay times as:

$$D = \frac{1}{3}\int_0^\infty \left\langle \vec{v}(0)\cdot\vec{v}(t)\right\rangle dt \tag{3.69}$$

where, in practice, the integration is taken until v(0) and v(t) become uncorrelated. The length of the correlated time interval depends on several factors including temperature and state of matter.

3.2.2 S(κ,ω) from Atomic Positions

Attention is now directed to the left-hand side of the flowchart of Fig. 3-1, where the atomic positions are utilized directly to compute the Van Hove correlation functions. To evaluate the classical version of S(κ,ω) without *a-prioi* knowledge of the dispersion relation or density of states, one could envision the following procedure. A wave vector is selected, and time-dependent correlations of particle density are calculated along that wave vector, producing the function I(κ,t). Next, a Fourier transformation operation is undertaken to ascertain the frequency content of the density correlations, which defines the allowable vibrational modes along vector κ in combination with the associated weight of those modes (i.e. the differential area under S(κ,ω) as a function of ω). Expanding this procedure to a system-wide average, one arrives at the scattering law of the system.

From a computational standpoint, it is convenient to circumvent the function G(r,t) and proceed directly from the intermediate scattering function, written now as a discrete time correlation function of the form:

$$I^{cl}\left(\vec{\kappa},\tau\right)=\frac{1}{NL\left(\tau\right)}\sum_{k=1}^{L(\tau)}\sum_{j,j'}\exp\left[-i\vec{\kappa}\cdot\vec{R}_{j'}\left(t_k\right)\right]\exp\left[i\vec{\kappa}\cdot\vec{R}_{j}\left(t_k+\tau\right)\right] \tag{3.70}$$

which includes self (j = j') and distinct ($j \neq j'$) terms. The position vectors, $\{R(t)\}$, originate from an atomistic simulation (classical or *ab-initio*), while the momentum transfer κ functions as an input variable. The grid of κ vectors may be spaced either linearly or logarithmically depending upon the purpose of the calculation and the details of the system. Since the thermal scattering cross section is highly sensitive to the behavior of the scattering law at small momentum transfers, a logarithmic scale is more appropriate in this context. In the present work, an intermediate function is computed for each atom in the scattering system, and the aggregate function corresponds to an average over all atoms.

By writing the atomic positions as c-numbers rather than Heisenberg operators, the classical approximation has already been invoked implicitly. Supplementary quantum correction schemes are the subject of a later section. Unlike the analytic intermediate function derived previously for a system of harmonic oscillators, Eq. (3.70) is not premised on the Gaussian or incoherent approximations, although the computational cost is greatly reduced if these approximations are made. MD calculations of the scattering law could proceed in accordance with any of the following combinations of approximations, which will be implemented computationally in Chapter 4:

(1) Classical + Incoherent + Gaussian Approximation

The Gaussian approximation, when applicable, is computationally time-saving because of the separation of the time and momentum transfer variables, which are normally embedded together in the particle density operator. Eq. (3.54) is still valid; however, the mean-squared displacement is now determined numerically from the atomic positions. This can be done either directly from the definition of (2.10), or by rewriting the MSD in terms of correlation functions and applying the cross-correlation theorem (as outlined by Kneller [47]).

(2) Classical + Incoherent Approximation

Under the incoherent approximation alone, Eq. (3.70) is evaluated explicitly with the condition $j = j'$, which is equivalent to averaging the diagonal elements of the I(κ,t) matrix. The momentum transfer and time variables are no longer separable, and the intermediate function is found by averaging the density correlation function over those vectors κ sharing the same modulus $|\kappa|$. The sample over κ must be large enough to account adequately for anisotropy in $\{R_j(t)\}$without unduly weighting any particular direction. Typically, a sample size of 100 or more randomly generated κ-vectors is sufficient for this purpose. Calculation of the intermediate function now requires one correlation function per atom per κ-point, thereby increasing the computational cost significantly over the Gaussian approximation.

(3) Classical + Gaussian Approximation

Relaxing the incoherent approximation, all $j \neq j'$ terms are now incorporated into the thermally averaged density correlation function. If the local forces on each atom are

assumed to be distributed as Gaussian random variables, then the displacements will also be Gaussian-distributed [48] and:

$$\left\langle \exp\left[i\vec{\kappa}\cdot\left(r_j(t) - r_{j'}(0)\right)\right]\right\rangle \cong \exp\left[\frac{-\kappa^2}{6}\left\langle \left(r_j(t) - r_{j'}(0)\right)^2\right\rangle\right] \tag{3.71}$$

which is analogous to the Gaussian approximation of the incoherent intermediate function. Unlike the "self" mean squared displacement, the thermal average on the RHS depends not only on fluctuations about the equilibrium lattice sites, but also on the mean distance separating the sites. An intuitive deduction is that the contribution to the coherent cross section tends to diminish as the atomic pair separation distance increases. Furthermore, at small values of κ, more distant pairs of atoms can contribute significantly. This is also intuitive in the sense that the opposite limit (very large κ) is associated with the purely "self" (incoherent) recoil effect.

(4) Classical Approximation Only

The computational procedure is similar to the incoherent case, except that, when $j \neq j'$, the cross-correlation is evaluated instead of the autocorrelation. A useful property of cross correlations is that:

$$C_{xy}(t) = C_{yx}^{*}(-t) \tag{3.72}$$

such that only half of the distinct *j,j'* combinations need to be considered. In the parlance of matrices, only the upper or lower triangular portion of the I(κ,t) matrix is necessary to formulate all off-diagonal elements. Consequently, the calculation of the intermediate function involves N autocorrelations and $(N^2-N)/2$ cross-correlations per κ point, where N is

the number of atoms. Given a typical MD supercell of hundreds or thousands of atoms, the presence of the geometrical term can increase the computational cost by orders of magnitude over the incoherent approximation.

An intriguing possibility is the execution of the exact ("classical only") calculation over short distances followed by a switch-over to the coherent Gaussian approximation at longer distances. Such an approach takes advantage of the fact that the atomic motions become de-correlated as separation distance increases.

It is worth noting that computations of $I(\kappa,t)$ may be performed efficiently on parallel processors, regardless of the approximations employed. This becomes apparent from the observation that the position correlations of each atom in $I_s(\kappa,t)$ are independent of all other atoms, and the pair correlations of $I_d(\kappa,t)$ are independent of all other pairs. Thus, after each processor is assigned a set of atoms or atomic pairs to analyze, the only additional communicational overhead originates from the acquisition of a final, global average of $I(\kappa,t)$. For this reason, all modules of the cross section code developed in the present work were written in parallel.

3.3 Liquid Argon $S(\kappa,\omega)$ Benchmark

Throughout the history of classical molecular dynamics, argon (in liquid or solid form) has been among the most thoroughly studied systems. There are several reasons for the

particular suitability of argon in this respect. The high atomic mass of the argon atom (relative to typical moderators) greatly diminishes the importance of quantum effects, and the absence of chemical reactivity allows for the interatomic potential to be expressed accurately in a simple two-body (Van der Waals) form. Near or above the melting temperature of 85 K, the scattering law of argon is nearly identical to its classical counterpart except at very large momentum transfers. Therefore, argon is an excellent benchmark against which validate the proposed algorithm for computation of the scattering law.

Two cases are examined: incoherent scattering in liquid argon-40 at 85.5 K with density 1.374 g/cm^3, and coherent scattering in liquid argon-36 at 120 K with density 1.043 g/cm^3. It should be recalled that the coherent scattering law is the sum of the self and distinct parts.

The Materials Explorer program [49] was employed in both cases to extract the time-dependent positions of the argon system. Interatomic interactions were modeled through a 12-6 Lennard-Jones potential using the empirical parameters proposed by Rahman [50]. Incoherent simulations were carried out for 81.9 picoseconds, and coherent simulations were run for 655.4 picoseconds at a time step of 5 femtoseconds in both cases. The temperature was held constant through rescaling of the atomic velocities every four steps. Because the liquid argon system has no long-ranged order (as is true of any liquid), important features of the distinct scattering law are dominated by close neighbor interactions and a minimal supercell was found to be sufficient. The supercell size was set to 864 atoms in the incoherent case and 16 atoms in the coherent case.

Results for the incoherent and coherent MD scattering law are compared against measured data from Skold [51] in Fig. 3-2 and Van Well [52] in Fig. 3-3 respectively. Due to the constant migration of atoms across the periodic boundaries of the supercell, the input k-mesh for the coherent scattering law was limited to the reciprocal lattice vectors of the cell, which give a density term, $\exp\left(i\kappa R_j\left(t\right)\right)$, that is continuous with respect to translations across the periodic boundary.

It is apparent that, for liquid argon, the classical form of the scattering law matches its quantum mechanical equivalent quite closely. Further confirmation is found in the zeroth order moment of the coherent scattering law, governed by Eq. (3.42). The 0^{th} moment of the MD scattering function, shown in Fig. 3-4, exhibits good agreement with the measured structure factor of liquid Ar-36 at 120 K.

While liquid-state neutron moderators are certainly of practical and academic interest, the present work is concerned with solids and, specifically, the nuances of graphite moderation. For solids, a simple equivalence of $S^{cl}(\kappa,\omega)$ to $S(\kappa,\omega)$ cannot be established except near the melting point, which is never approached in standard reactor operation. The next section focuses on failures of the classical formulation and the means of addressing these shortcomings.

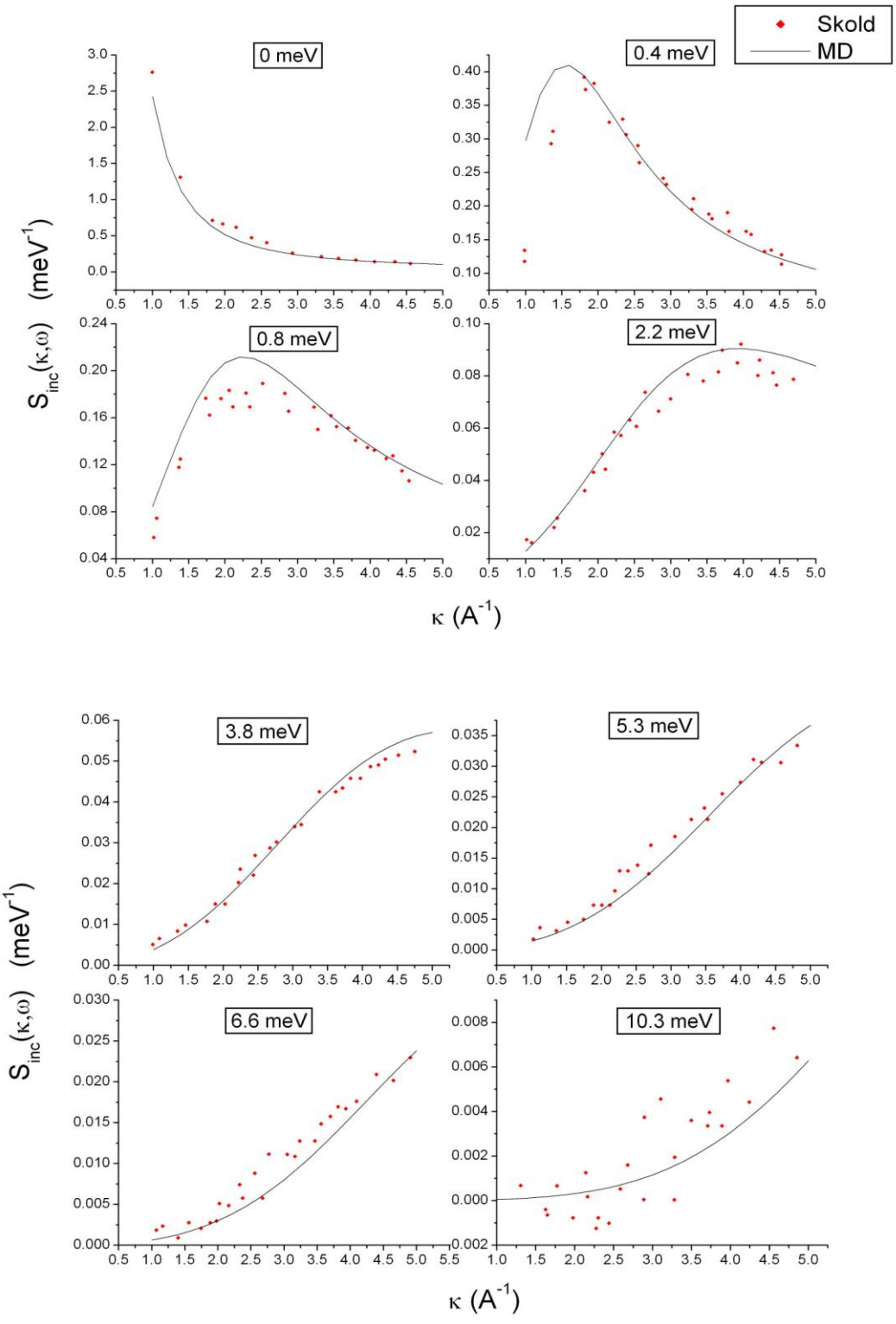

Fig. 3-2. Incoherent scattering law of Argon-40 at T = 85.5 K and ρ = 1.374 g/cm^3

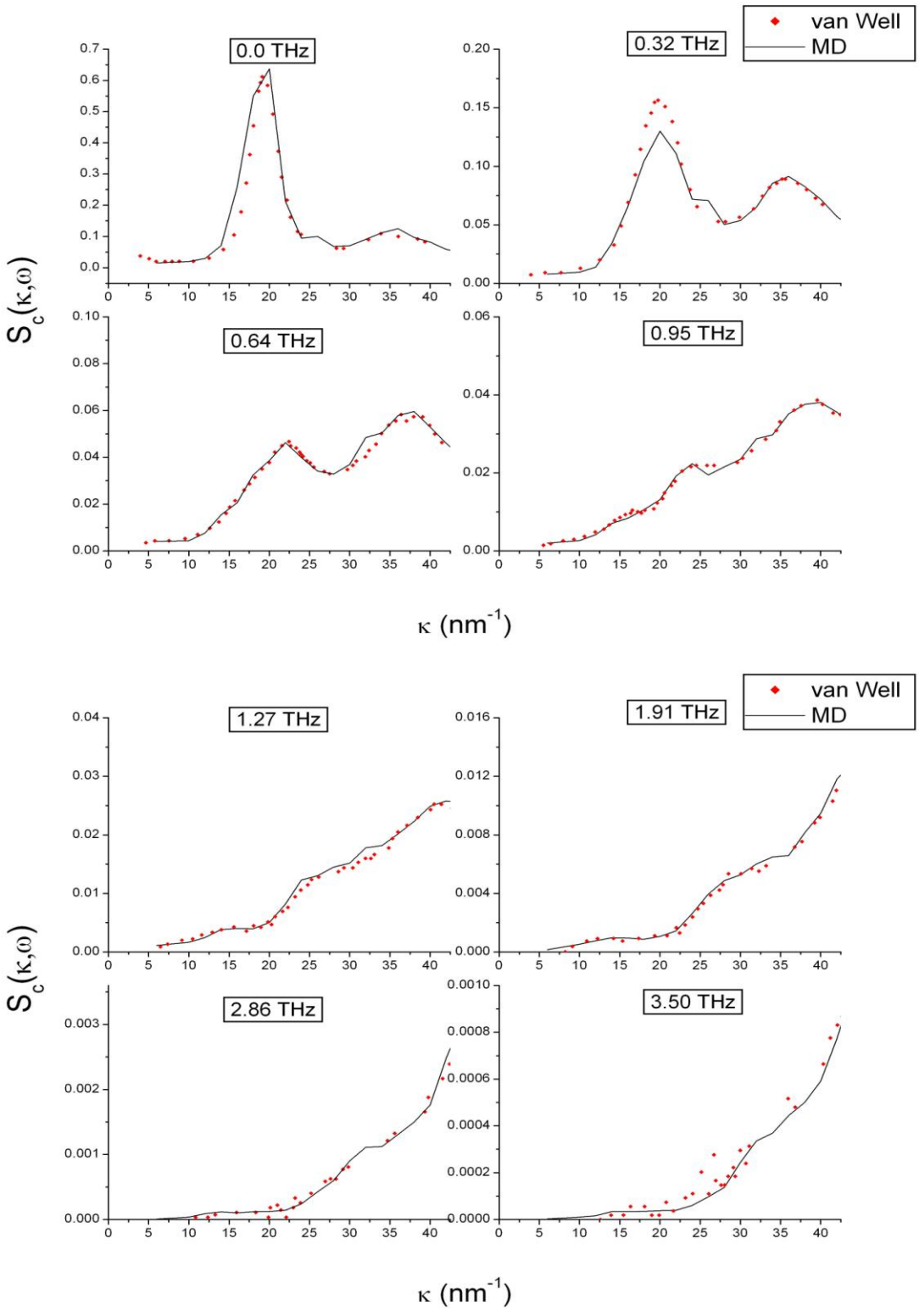

Fig. 3-3. Coherent scattering law of Argon-36 at T = 120 K and ρ = 1.043 g/cm^3.

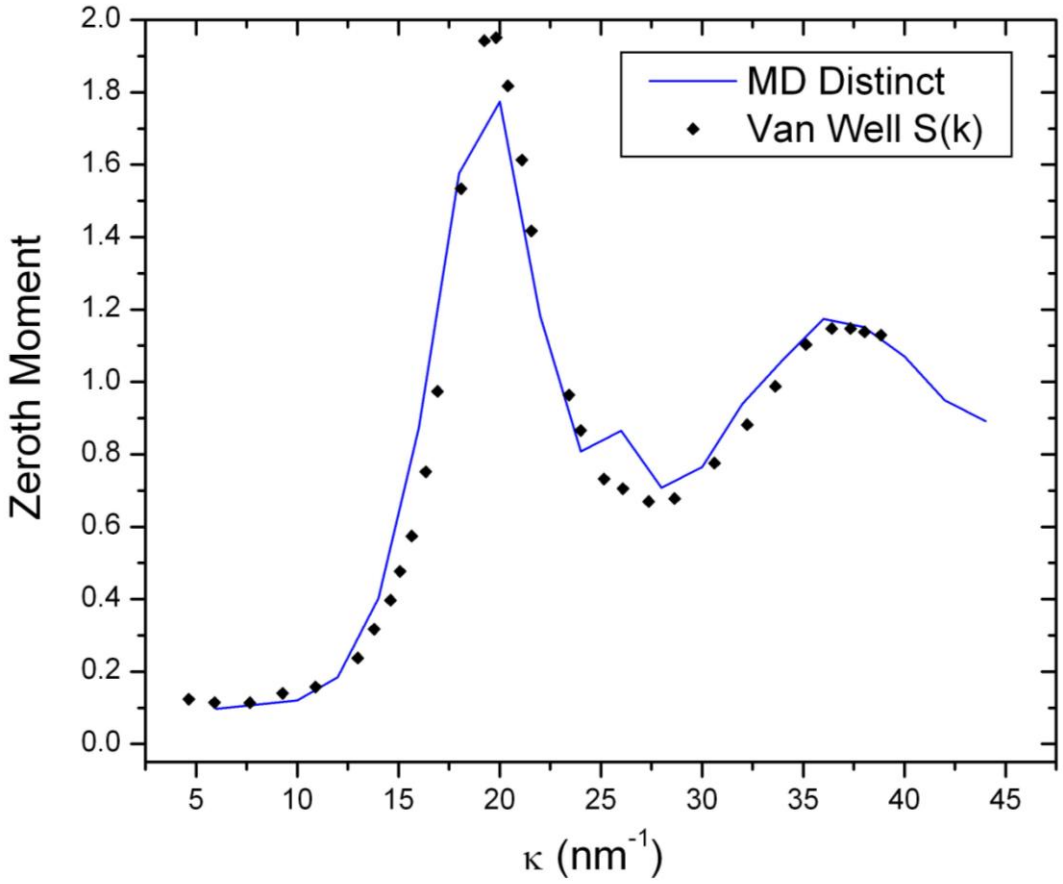

Fig. 3-4. Zeroth moment of the liquid Argon-36 coherent scattering law at 120 K.

3.4 Failure of Classical Formulation

The classical incoherent inelastic scattering cross section of graphite is shown in Fig. 3-5 alongside the benchmarked *ab-initio* / lattice dynamical result. Two deficiencies of the classical MD model are immediately apparent. First, the MD cross section is consistently larger than the *ab-initio* based cross section throughout the entire range of incident energies (and especially at low energies). Second, the classical cross section converges to the bound atom cross section rather than the free atom cross section.

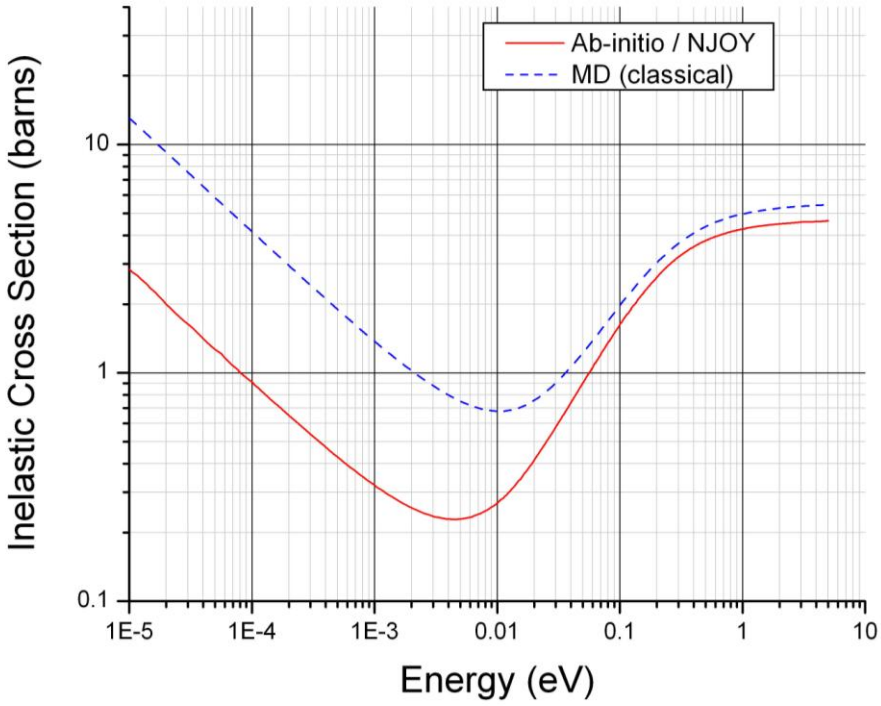

Fig. 3-5. The inelastic incoherent cross section of graphite versus its classical MD counterpart

General overestimation: The classical scattering law is symmetric in β; therefore, phonon emission and absorption are given equal weighting regardless of the incident energy. In reality, the proportion of emission to absorption is modulated by the detailed balance factor, which stipulates that the probability of finding the system in a higher energy state is lower by a factor of $\exp\left(\hbar\omega / k_B T\right)$ than the probability of finding it in a lower energy state. Phonon absorption represents a transition in the scattering system from higher to lower energy, and since this is the dominant mechanism for energy transfer at low incident neutron energies, the classical scattering law is seen to generate a cross section that is too high. For example, the differential energy spectrum at E_{inc} = 1E-5 eV, shown in Fig. 3-6, mirrors the shape of the

phonon frequency distribution yet does not reflect the actual occupancy of the various phonon states. In other words, unoccupied energy states are erroneously contributing to the cross section. To remedy the situation, detailed balance must be enforced properly.

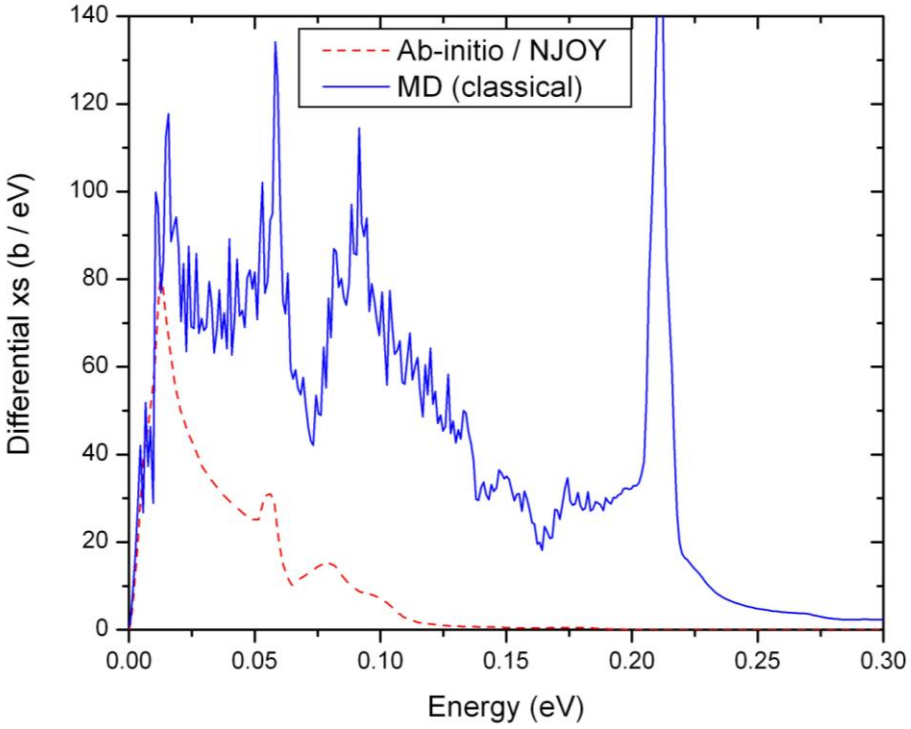

Fig. 3-6. Differential energy spectrum of graphite at E_{inc} = 1E-5 eV

Atomic recoil: In evaluating the scattering law from classical MD atomic positions, information is lost regarding the perturbation to the scattering system caused by neutron interaction. This perturbation appears numerically in the imaginary part of the density-density correlation function, and its presence is responsible for the quantum 1st order moment (recoil) rule. The 1st order moment is intimately related to the convergence of the cross

section to the free atom limit [45]; therefore, the failure of the classical formulation in this regard is not surprising.

The differential energy spectrum at incident energy 5.1 eV (near the free atom limit) is shown in Fig. 3-7. Since the recoil response is inadequately treated in $S^{cl}(\kappa,\omega)$ and the atom cannot receive appreciable energy from the neutron, the classical distribution is highly peaked about small energy transfers whereas the *ab-initio* / NJOY distribution covers a much larger range of energy transfers. As mentioned before, the symmetry of the classical scattering law in β results in an equal weighting of energy gain or loss. Hence, the classical cross section is also symmetric about E_{inc}, which is clearly unphysical due to the overwhelming preference for phonon emission (downscattering) in this regime.

An intuitive corollary of this argument is that the quantum correction is less important for heavy atoms that exhibit little recoil. This is consistent with the well-known fact that, at a given temperature, the impact of quantum effects scales inversely with the atomic mass number. Clearly, the missing quantum effects are critical to the investigation of thermal neutron scattering in graphite. Therefore, a major objective of this work is to supplement the classical MD formalism with appropriate corrections.

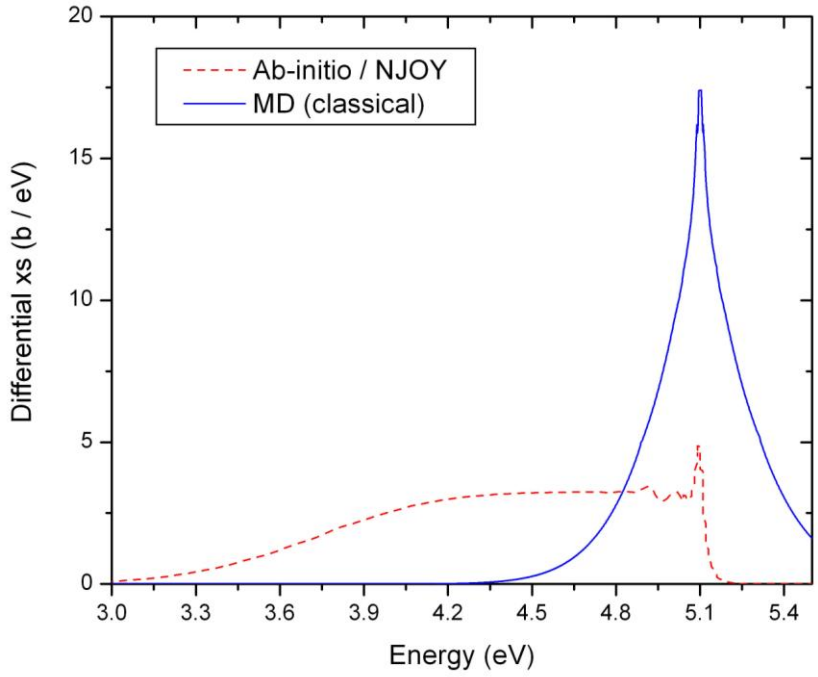

Fig. 3-7. Differential energy spectrum of graphite at E_{inc} = 5.1 eV

3.4.1 Semiclassical Corrections

Much past effort has been directed towards the derivation of a general semiclassical correction function of the form:

$$Q(\kappa,\omega) = \frac{S(\vec{\kappa},\omega)}{S^{cl}(\vec{\kappa},\omega)} \tag{3.73}$$

that imposes the proper degree of asymmetry into the scattering law. The idea is effectively to simulate the imaginary part of I(κ,t) by introducing a skew in S(κ,ω) resembling that which would follow naturally from a complex intermediate function. Several correction functions have been discussed in literature (see, for example, [53]), all demonstrating the necessary detailed balance relation between Q(κ,ω) and Q(κ ,-ω). The simplest approach,

attributed to *Schofield* [54], is to utilize the exponential factor relating the quantum symmetric and quantum asymmetric scattering laws:

$$Q_{sc}(\omega) = \exp(\hbar\omega / 2k_B T) \tag{3.74}$$

This version of the correction factor obviously preserves detailed balance but is not the only function capable of doing so; for example, the *harmonic* correction factor [55], given by:

$$Q_h(\omega) = \left[\frac{(\hbar\omega / k_B T)}{1 - \exp(-\hbar\omega / k_B T)} \right] \tag{3.75}$$

also fulfills detailed balance but is drastically different from the Schofield correction at high frequencies. The harmonic form – so called because it generates the exact quantum result from classical correlation functions that are linearly dependent on the position and / or momentum variables [56] – follows from the expansion terms (up to first order) of the tangent in Eq. (3.37) after converting to the frequency domain and applying Eq. (3.35).

Yet another candidate form of $Q(\omega)$ is found by simply setting $S^{cl}(\kappa,\omega) = \bar{S}(\kappa,\omega)$, yielding:

$$Q_{st}(\omega) = \frac{2}{1 + \exp\left(-\frac{\hbar\omega}{k_B T}\right)} \tag{3.76}$$

which is labeled the *standard approximation* in literature [57]. Because of the lack of an ω term in the numerator, $Q_{st}(\omega)$ asymptotically approaches a finite number as $\omega \to \infty$ in

contrast to the other correction functions which increase without limit. The functions $Q_{sc}(\omega)$, $Q_h(\omega)$ and $Q_{st}(\omega)$ are displayed together in Fig. 3-8.

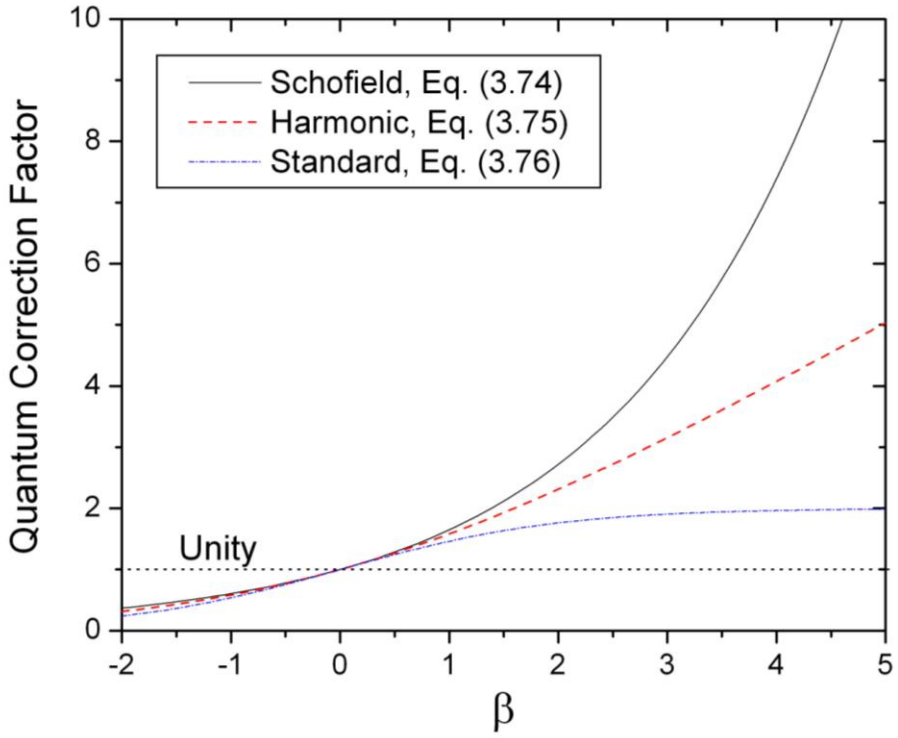

Fig. 3-8. Profiles of the Schofield, harmonic, and standard correction factors. All converge to unity at β=0.

Egorov [53] has examined the suitability of Eqs. (3.74) - (3.76) for various physical systems that are analytically solvable. Perhaps not surprisingly, there is no single factor that universally outperforms all others. The present study is focused on graphite, and so the question of immediate interest is: Which of these factors is most justifiable for solid-state systems? This question will be a subject of investigation in Chapter 4. Attention is now directed towards the alternative approach for the inclusion of quantum corrections: evaluation of the imaginary part of I(κ,t).

3.4.2 Imaginary part of I(κ,t)

Turner, in an early work [58], recognized that the intermediate function could be written in terms of an expansion over $\hbar$ as:

$$I(\kappa,t)=\frac{1}{N}\sum_{n=0}^{\infty}\hbar^{2n}\left\langle\sum_{j,j'}\exp\left(-i\kappa\cdot r_{j'}(0)\right)\exp\left(i\kappa\cdot r_j(t)\right)A_{2n}\right\rangle \tag{3.77}$$

$$-i\frac{1}{2N}\sum_{n=0}^{\infty}\hbar^{2n+1}\left\langle\sum_{j,j'}\exp\left(-i\kappa\cdot r_{j'}(0)\right)\cdot i\kappa\frac{\partial}{\partial p_j(0)}\exp\left(i\kappa\cdot r_j(t)\right)A_{2n}\right\rangle$$

where p_j is the impulse on atom j and $A_0 = 1$. $I^{cl}(\kappa,t)$ therefore corresponds to the *zeroth* order term in $\hbar$. The higher order coefficients are increasingly cumbersome to evaluate and are of little practical interest. The two lowest-order terms in $\hbar$, however, hold special physical significance. Namely, atomic recoil is associated with the expression of order $\hbar$, and quantum statistical effects arise in the order $\hbar^2$ term [59]. If only the first-order term is included in the summation, it can be shown that:

$$I(\kappa,t)=I^{cl}\left(\kappa,t+\frac{i\hbar}{2k_BT}\right) \tag{3.78}$$

which is directly implementable only in cases where the intermediate function varies explicitly with time. This expression is of theoretical interest, however, because it expansion (to 1st order in time) is formally equivalent to the Schofield semiclassical correction of Eq. (3.74).

For systems that obey classical statistics to an overwhelming extent (gases, liquids and high-temperature solids, for example) the $\hbar^2$ term can be safely disregarded. Recoil, on the other hand, will always be an important physical process when the neutron-to-atom momentum transfer is large in comparison with the thermal energy of the atom. In the regime of low-temperature solids, both effects impact the thermal scattering cross section appreciably. Quantum statistics enter the picture through the thermal occupancy of the phonon modes, where, in classical MD, all modes are excited regardless of temperature. The breakdown of classical statistics is responsible, for example, for the well-known failure of the Dulong-Petit heat capacity law at low temperatures, later remedied in the Debye model through introduction of an appropriate occupancy factor (the Planck distribution). In neutron scattering theory, the occupancy factor is closely related to the detailed balance condition.

Sunakawa, Nishigori, and Yamasaki (in [60],[61], and [62]) further developed the relationship between the real and imaginary parts of $I(\kappa,t)$ through utilization of the quantum-classical correspondence principle. The basic idea is that, instead of treating the position operators, $\{R_j(t)\}$, merely as the classical atomic positions, the non-commutation of $R_j(0)$ with $R_j(t)$ is recognized and the scattering formulae are allowed to retain information regarding the response of the scattering system to neutron interactions.

In general, given two operators *A* and *B*:

$$\exp(A)\exp(B) = \exp(A + B + C) \tag{3.79}$$

where:

$$C = \frac{1}{2}\left[A,B\right] + \frac{1}{12}\left[\left[A,B\right],B\right] + \frac{1}{12}\left[\left[B,A\right],A\right] + \frac{1}{24}\left[\left[\left[B,A\right],A\right],B\right] + \ldots \tag{3.80}$$

The density correlation function has exactly the same form as Eq. (3.79), indicating that a similar expansion is possible; namely:

$$I\left(\kappa,t\right) = \frac{1}{N}\sum_{j,j'}\left\langle \exp\left[i\left(\vec{\kappa}\cdot\left(\vec{r}_{j'}\left(t\right) - \vec{r}_{j}\left(0\right)\right) - K^{c}_{jj'}\left(t\right)/\hbar\right)\right]\right\rangle \tag{3.81}$$

in which:

$$K^{c}_{jj'}\left(t\right) = \frac{\hbar}{i}\frac{1}{2}\left[pr_{j'}\left(0\right), pr_{j}\left(t\right)\right] + \frac{\hbar}{i}\frac{1}{12}\left[\left[pr_{j'}\left(0\right), pr_{j}\left(t\right)\right], pr_{j}\left(t\right)\right] \tag{3.82}$$

$$-\frac{\hbar}{i}\frac{1}{12}\left[\left[pr_{j}\left(t\right), pr_{j'}\left(0\right)\right], pr_{j'}\left(0\right)\right] + \ldots$$

In simple systems, the 2nd order and greater terms are zero. A well-known result of quantum mechanics is that [42]:

$$\frac{1}{i\hbar}\left[A,B\right] \;\rightarrow\; \left\{A,B\right\} \tag{3.83}$$

where $\left\{\ \right\}$ denotes the classical Poisson brackets, defined by:

$$\left\{A,B\right\} = \sum_{k}\left(\frac{\partial A}{\partial q_k}\frac{\partial B}{\partial p_k} - \frac{\partial B}{\partial q_k}\frac{\partial A}{\partial p_k}\right) \tag{3.84}$$

in which q_k and p_k are components of the generalized positions and momenta. Keeping the first-order term of Eq. (3.82) and expanding:

$$K^{c}_{jj'}\left(t\right) = \frac{1}{2}\left\{ pr_{j}\left(0\right), pr_{j'}\left(t\right)\right\} = \frac{1}{2}\left[\frac{\partial\left(pr_{j}\left(0\right)\right)}{\partial p_{j}\left(0\right)}\frac{\partial\left(pr_{j'}\left(t\right)\right)}{\partial r_{j}\left(0\right)} - \frac{\partial\left(pr_{j'}\left(t\right)\right)}{\partial p_{j}\left(0\right)}\frac{\partial\left(pr_{j}\left(0\right)\right)}{\partial r_{j}\left(0\right)}\right] \tag{3.85}$$

$$= -\frac{1}{2}\left[\frac{\partial\left(pr_{j'}(t)\right)}{\partial p_j(0)}\,p\right]$$

where p is the momentum exchange. The factor $K^c_{jj'}(t)$ therefore describes the change in trajectory experienced by atom j in response to an external impulse on atom j' (e.g. due to neutron interaction). Although the cross terms ($j \neq j'$) can be nontrivial for atoms in close proximity, only the $j = j'$ (self) term is considered in the present work.

Some overlap can be seen between the $K^c_{jj'}(t)$ correction and the expansion over $\hbar$ developed by Turner. Retaining the two lowest-order terms of Eq. (3.77) and carrying out the partial differentiation, Turner's equation becomes:

$$I(\kappa,t) = I_{cl}(\kappa,t)\cdot\left[1+\frac{ip^2}{\hbar}\left\langle\frac{\partial r_j(t)}{\partial p_j(0)}\right\rangle\right] \tag{3.86}$$

$$= I_{cl}(\kappa,t)\cdot\left[1-\frac{i}{\hbar}K^c_{jj}(t)\right]$$

where:

$$I_{cl}(\kappa,t) = \left\langle\sum_{j,j'}\exp\left(-i\kappa\cdot r_{j'}(0)\right)\cdot\exp\left(i\kappa\cdot r_j(t)\right)\right\rangle \tag{3.87}$$

and Eq. (3.86) is seen to be identical to the first two terms of the Taylor expansion of Eq. (3.81) over $K^c_{jj}(t)$.

Generally speaking, the system response is quite sensitive to the magnitude of the external impulse, p_j, which can range from a slight perturbation to complete dislodgement of an atom.

The response term, $K_{jj'}$, is exactly derivable for certain simple systems. Two such systems are of particular interest in the present work:

Free atom

A free atom responds to an external impulse by traversing a straight line trajectory at constant velocity as:

$$\vec{r}(t) = \vec{r}_o + \frac{\vec{p}(0)}{M} t \tag{3.88}$$

where r_o is the initial position and $\vec{p}$ is the external impulse vector. In this case, Eq. (3.85) gives:

$$K^c(t) = \frac{1}{2}\{pr(0), pr(t)\} = \frac{p^2}{2M} t \tag{3.89}$$

and the intermediate function becomes:

$$I(\kappa, t) = I^{cl}(\kappa, t) \cdot \exp\left(\frac{-i\hbar\kappa^2}{2M} t\right) \tag{3.90}$$

which is quite generally correct at very large values of the momentum transfer, κ.

Harmonic Oscillator

A simple harmonic oscillator responds to an impulse as:

$$\vec{r}(t) = \vec{r}_o \cos(\omega t) + \frac{\vec{p}(0)}{M} \sin(\omega t) \tag{3.91}$$

and the corresponding Poisson brackets are:

$$K^c(t) = \frac{1}{2}\{pr(0), pr(t)\} = \frac{p^2}{2M\omega}\sin(\omega t) \tag{3.92}$$

which reduces to the free atom case (Eq. (3.90)) in the limit of ω → 0. In real systems, atomic vibrations occur over a distribution of frequencies rather than at one specific frequency. Eq. (3.92) can be generalized to a system of interacting harmonic oscillators by including the density of states and occupation factors:

$$\bar{K}^c(t) = \int_0^\infty d\omega \cdot \rho(\omega) \cdot \left[\frac{1}{\exp\left(\hbar\omega / k_B T\right) - 1}\right] \frac{p^2}{2M\omega}\sin(\omega t) \tag{3.93}$$

$$= \int_0^\infty d\omega \cdot \frac{\rho(\omega) \cdot \exp\left(\frac{-\hbar\omega}{2k_B T}\right)}{2\sinh\left(\frac{\hbar\omega}{2k_B T}\right)} \frac{p^2}{2M\omega}\sin(\omega t)$$

so that the intermediate function becomes:

$$I(\kappa, t) = I^{cl}(\kappa, t) \cdot \exp\left[\frac{-i\hbar\kappa^2}{2M}\int_{-\infty}^{\infty} \frac{\rho(\omega)\sin(\omega t)\exp\left(\frac{-\hbar\omega}{2k_B T}\right)}{2\omega\sinh\left(\frac{\hbar\omega}{2k_B T}\right)} d\omega\right] \tag{3.94}$$

where the exponential factor is seen to be equivalent to the imaginary argument of the intermediate function for a system of quantum harmonic oscillators, as given by Eqs. (3.55) and (3.58). $I^{cl}(\kappa, t)$ is *not* equivalent to the real part of Eq. (3.55), however, as $I^{cl}(\kappa, t)$ and Re($I(\kappa, t)$) are identical only to zeroth order [63].

Chapter 4

Results for Perfect Graphite

4.1 ρ(ω) from MD

4.1.1 Dynamical matrix vs. velocity autocorrelation

A property of great relevance to S(κ,ω) as well as the benchmarking of the MD potential is the phonon density of states, ρ(ω), which can be established either through static displacements (via the dynamical matrix) or through dynamical correlations at equilibrium. ρ(ω) is closely related to the incoherent scattering properties of the system and also reveals fundamental information about the details of interatomic binding.

The graphite unit cell is hexagonal with 2 non-equivalent atoms, and so a total of 6 displacements (3 for each atom) are sufficient to construct the dynamical matrix. Starting from the relaxed MD supercell at 0 K, each basis atom was displaced by a distance D = 0.02 Å along the following directions:

Displacement 1: $\Delta\vec{r} = D\left[\cos(\pi/3), \sin(\pi/3), 0\right]$

Displacement 2: $\Delta\vec{r} = D[1,0,0]$

Displacement 3: $\Delta\vec{r} = D[0,0,1]$

where the magnitude of the displacement is kept well within the linear response (harmonic) regime. In general, all atoms in the system will experience some nonzero net force as a consequence of the displacement, though atoms sufficiently far from the displacement will be

affected negligibly. Computationally, the size of the supercell limits the maximum range of the atomic interactions – an important consideration in *ab-initio* simulations. The requisite MD supercell size, on the other hand, is dictated by the cutoff distance of the potential energy function. This is due to the fact that, in MD, no additional information is discerned by increasing the system size beyond the potential function cutoff range.

For the velocity autocorrelation calculation, $\langle v(0)v(t) \rangle$ was evaluated from the velocities of 288 atoms located near the center of an 8000 atom MD supercell, with the velocities recorded over 131072 steps (65.5 picoseconds). Of particular concern is the effect of the Van der Waals forces on $\rho(\omega)$ at low frequencies. First, the simplest case was examined – modeling long-ranged forces using only the anisotropic cutoff function discussed in Chapter 2 (and with no L-J potential). The system temperature was set to 300 K, although, well below the melting point, the MD density of states is insensitive to temperature. This is true because the phonon states of a classical system are not subject to the thermal factor that attenuates the occupancy of high energy vibrational modes.

Fig. 4-1 shows a comparison of the graphite density of states (frequency distribution) determined using the dynamical matrix and the velocity autocorrelation methods. The PHONON code [64] was used to process the dynamical matrix from the input MD force file. Dynamical matrix results are shown with and without the condition of rotational / translational invariance (RTI), which is commonly imposed in *ab-initio* / lattice dynamics

calculations. The dispersion relation, also computed from the dynamical matrix, is given in Fig. 4-2.

Evidently, the dynamical matrix calculation with RTI generates a smooth parabolic region at low frequency, whereas the Fourier transform of the velocity autocorrelation function exhibits a gap below 2.5 THz where few vibrational modes exist. Specifically, the low frequency end of the vibrational spectrum is collapsed into a single, narrow peak. From the partial (in-plane and out-of-plane) density of states, plotted in Fig. 4-3, the gap is seen to be associated exclusively with the out-of-plane modes.

When the RTI condition is removed, the PHONON calculation is brought into much better agreement with the transform of the velocity autocorrelation. Since the velocity autocorrelation function acts as a direct, dynamical measure of the frequency content of the system, the observed inconsistency is seen to result from a deficiency in the RTI condition as applied to this particular system. Effectively, RTI alters the Hellmann-Feynman forces such that the acoustical modes are compelled to demonstrate Debye behavior about $\omega = 0$. This treatment is generally appropriate for solids; however, there is no guarantee that an empirical MD potential function will produce a Debye-type relation at low ω. Based on these findings, it is recommended that the RTI condition be used cautiously in systems that are subject to short-ranged empirical potentials. Because the low-ω regime affects the thermal cross section to a far greater extent than other frequencies, the relevant components of the graphite potential energy function must be reconciled with the expected Debye behavior.

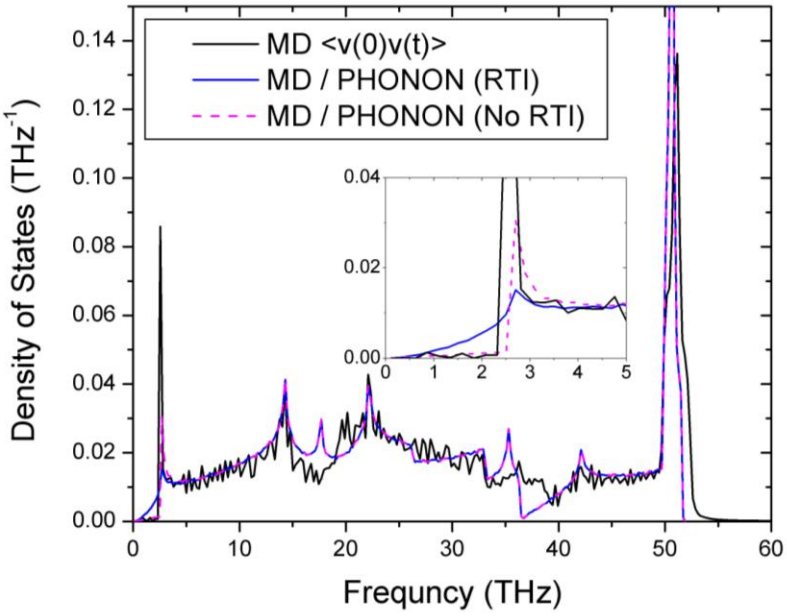

Fig. 4-1. Phonon density of states of the MD graphite system. Out-of-plane motion is restricted only through the anisotropic cutoff function. MD / PHONON results are shown with and without the rotational / translational invariance (RTI) condition.

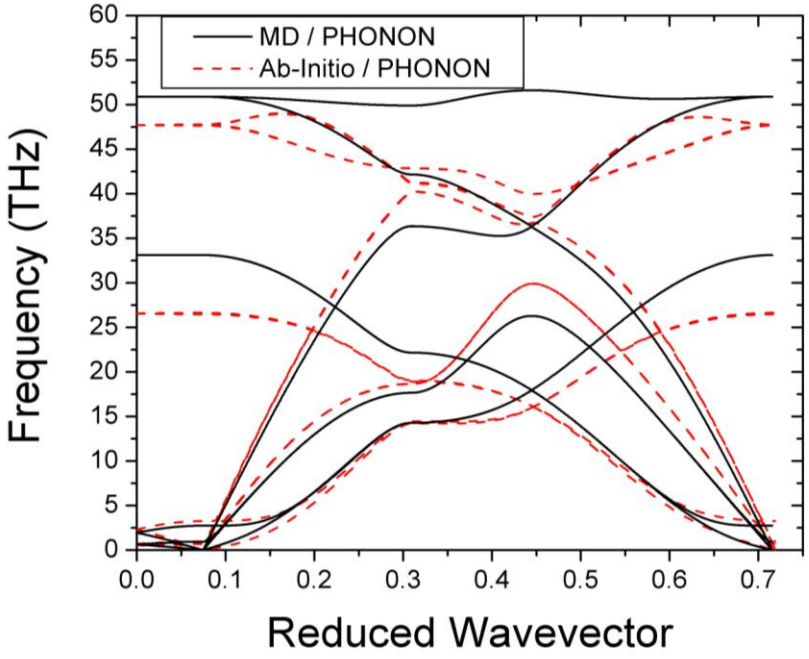

Fig. 4-2. Phonon dispersion relation of the MD graphite system.

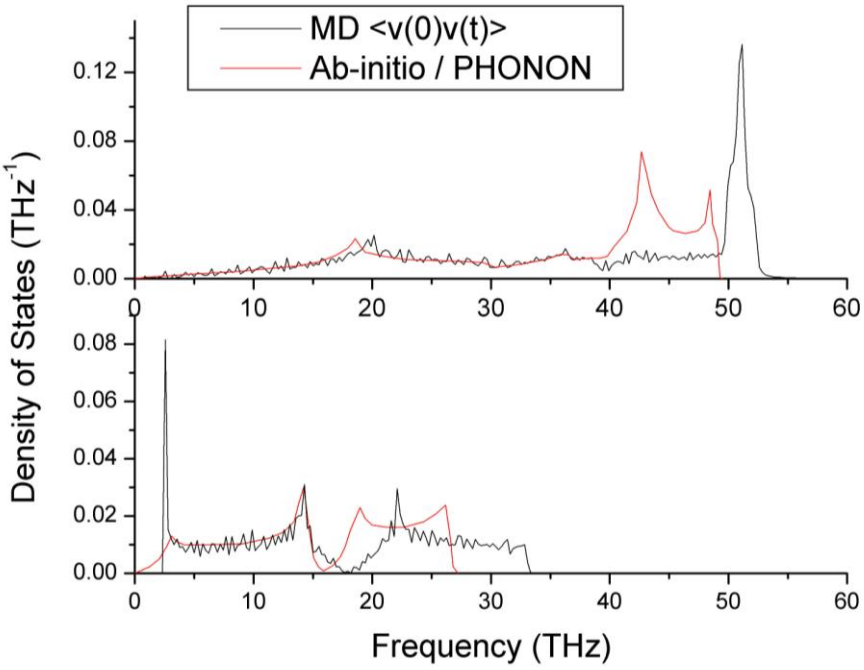

Fig. 4-3. In-plane (top panel) and out-of-plane (bottom panel) partial frequency spectra of the MD graphite system. Out-of-plane motion is restricted only through the anisotropic cutoff function.

4.1.2 Mismatch at Low Frequency

In Fig. 4-3, a gap was observed in the low-frequency out-of-plane vibrational modes of $\rho(\omega)$. Several components of the potential function contribute to out-of-plane vibrations; these include the pairwise attractive and repulsive functions, the torsional term, and the c-axis cutoff function. With the exception of the c-axis cutoff, all of the aforementioned terms act on neighboring atoms within the same plane. Evidently, the c-axis cutoff function, when used alone, causes all atoms to oscillate at a very specific frequency (~ 2.5 THz) along the c-axis rather than generating the frequency distribution that would arise in reality through direct interplanar interactions. The solution, therefore, is to explicitly incorporate interplanar

interactions into the potential function, as per the long range Lennard-Jones potential discussed in section 2.3.1.

To test this hypothesis, the frequency distribution of graphite was computed from <v(0)v(t)> under the Lennard-Jones model of the Van der Waals forces. Without explicit long-range interactions, the distribution exhibits a single peak around 2.5 THz and an absence of vibrational modes below that point. With Lennard-Jones interactions added to the REBO potential, the density of states from MD matches the *ab-initio* distribution fairly well, as shown in Fig. 4-4. The Lennard-Jones potential does not impact higher energy modes significantly, supporting the earlier assertion that long-ranged, interplanar forces are associated with the lowest frequency modes in graphite. All MD results presented hereafter pertain to the potential energy model developed in Chapter 2, which incorporates the Lennard-Jones potential in combination with the anisotropic cutoff function.

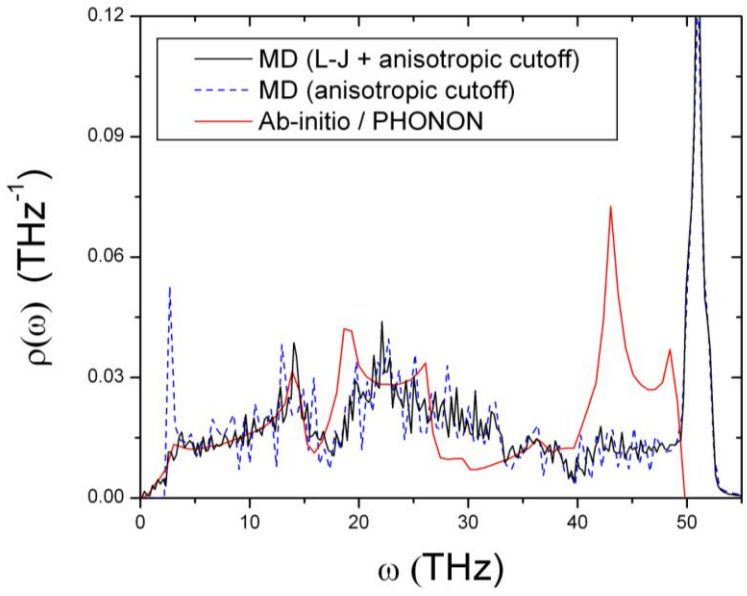

Fig. 4-4. Impact of the long-range force term on the graphite density of states

4.2 Heat Capacity

The specific heat capacity, C_V, is a useful benchmark against which to test ρ(ω) distributions obtained from atomistic simulation since the generated distribution should be *predictive* of C_V , and also because C_V is straightforward to measure experimentally. The specific heat capacity is defined as the amount of thermal energy required to raise the temperature of a unit mass by one degree. Knowing the heat transferred to a substance as well as the resulting temperature change, the heat capacity (averaged over the temperature change) is then:

$$\bar{C}_V = \frac{\Delta Q}{m\Delta T} \tag{4.1}$$

where ΔQ is the heat transferred, ΔT is the change in temperature, and *m* is the mass. Experimental observations have long revealed that the heat capacity of a solid is approximately constant at high temperatures. Under the assumption that $k_B T \gg \hbar\omega$ in the system, French physicists Dulong and Petit proved that C_V, for simple solids, is given by the compact expression:

$$C_V = rN_A M k_B \tag{4.2}$$

in which *r* is the number of degrees of freedom, N_A is Avogadro's number and *M* is the molar mass. Thus, the high-temperature limit of the specific heat capacity of a solid is a universal constant equal to about 25 J/mol-K.

Not all phonon modes are excited at low temperatures, however, and corresponding adjustments to the theoretical treatment are required in this case. A more general expression

was derived by Debye, who demonstrated that [65]:

$$C_V = rk_B \int_0^\infty d\omega \rho(\omega) \left(\frac{\hbar\omega}{k_B T}\right)^2 \exp\left(\frac{\hbar\omega}{k_B T}\right) \cdot \left[\exp\left(\frac{\hbar\omega}{k_B T}\right) - 1\right]^{-2} \tag{4.3}$$

which leads to a value of $C_V = 0$ at $T = 0$ followed by a $C_V \propto T^3$ region at very low temperature. In the classical limit, Eq. (4.3) reduces to the Dulong-Petit law.

Fig. 4-5 shows the heat capacity calculated from Eq. (4.3) using the MD density of states, as compared against measured data from DeSorbo [66]. Agreement is generally quite good, although a small but significant difference is evident above 400 K. This may be due to the high-frequency modes of the MD distribution, which require a higher temperature for excitation and also diverge considerably from *ab-initio* calculations (see Fig. 4-3).

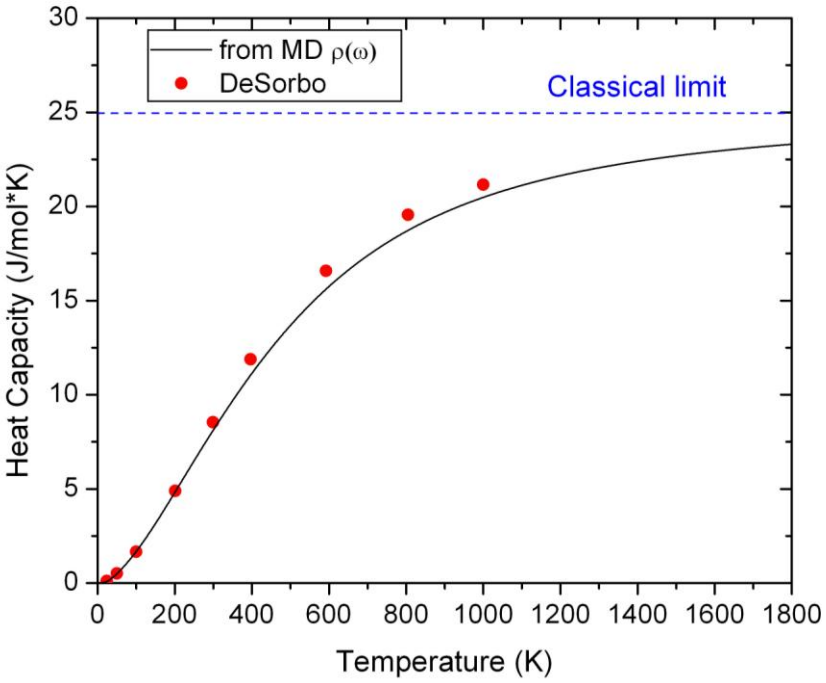

Fig. 4-5. Heat capacity of graphite, evaluated from the MD ρ(ω)

4.3 Dynamic Pair Correlation Function

Among the various MD correlation functions, the dynamic pair correlation, $G^{cl}(\vec{r},t)$, is one of the simplest to develop and interpret. $G^{cl}(\vec{r},t)$ contains a wealth of dynamical information; in fact, an exact knowledge of $G^{cl}(\vec{r},t)$ implies an awareness of the distribution of atomic displacements at all times. Because $\vec{r}$ is defined as the displacement between two atoms, the coordinates of the lattice sites are lost in compiling $G^{cl}(\vec{r},t)$ although this information is rarely pertinent to dynamical properties.

In the limit of long delay times, $G^{cl}(\vec{r},\infty)$ essentially provides a snapshot of the magnitude and variance of displacements in the supercell, as shown in Fig. 4-6 for graphite at various temperatures. Assuming the condition of thermal equilibrium, $G^{cl}(\vec{r},t)$ is characterized by a series of Gaussian-type peaks – one for each coordination shell – which, at large displacements, merge together as a continuum due to the shrinking distance between neighboring shells.

For a perfectly crystalline system at 0 K, $G^{cl}(\vec{r},t)$ would be represented as a series of delta functions located at the coordination shell positions. The effect of temperature is to broaden these peaks and decrease the distance at which continuum behavior becomes apparent. One implication of this phenomenon is that distinctive features of the coherent scattering cross section are also broadened as temperature increases.

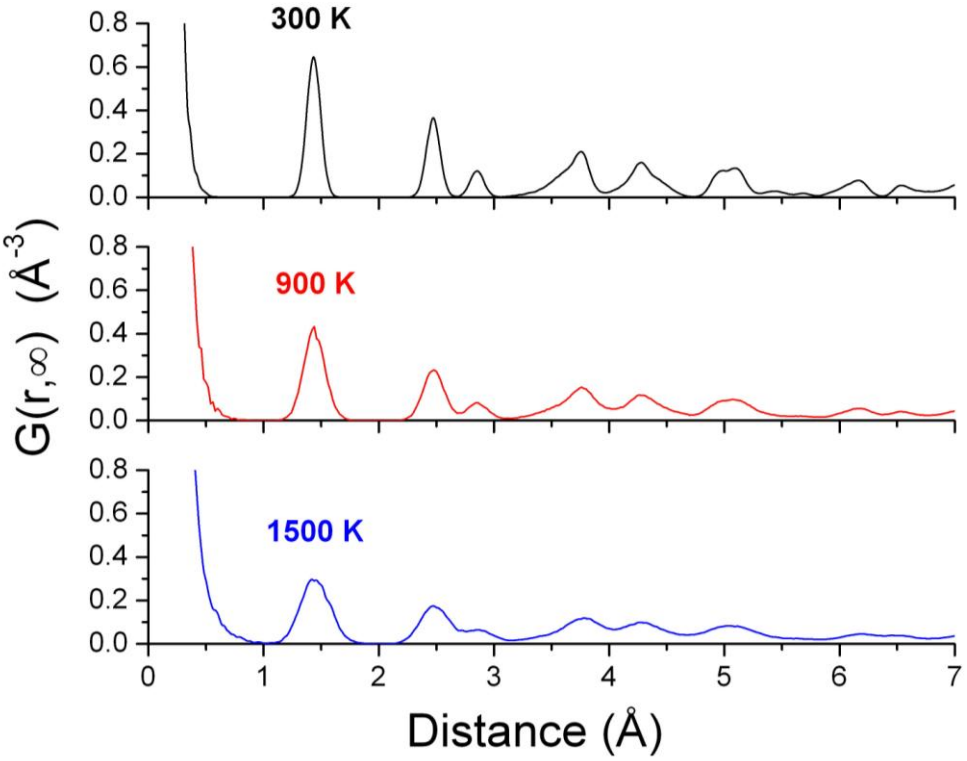

Fig. 4-6. Long-time limit of the classical dynamic pair correlation function of perfect graphite

In spite of peak broadening, the normalization integral over $\vec{r}$ is constant as per the relations:

$$\int_0^\infty G_s^{cl}\left(\vec{r},t\right)d\vec{r}=1 \tag{4.4}$$

$$\int_0^\infty G^{cl}\left(\vec{r},t\right)d\vec{r}=N \tag{4.5}$$

where N is the number of atoms in the supercell and $d\vec{r}=4\pi r^2 dr$. $G_s^{cl}\left(\vec{r},t\right)$ also obeys a second-order moment rule:

$$\left\langle r^2\left(t\right)\right\rangle=\int_0^\infty r^2 G_s^{cl}\left(\vec{r},t\right)d\vec{r} \tag{4.6}$$

that yields the mean-squared displacement. Eq. (4.6) can be generalized to the mean squared displacement between any two atoms in the system via the expression:

$$\left\langle r_{j-j'}^2(t)\right\rangle = \int_0^\infty r^2 G_{d,j-j'}^{cl}(\vec{r},t)\,d\vec{r} \tag{4.7}$$

where $G_{d,j-j'}^{cl}(\vec{r},t)$ is the *j,j'* component of the distinct pair correlation summation.

Time Dependence

Fluctuations in $G^{cl}(\vec{r},t)$ with respect to time arise primarily in the form of small-scale oscillations about the $G^{cl}(\vec{r},\infty)$ values plotted in Fig. 4-6. For a sufficiently large system, the shape of the $G_d^{cl}(\vec{r},t)$ functions displayed in that figure is correct even at *t* = 0, since the atoms, at thermal equilibrium, will already be distributed randomly about their equilibrium sites.

$G_s^{cl}(\vec{r},t)$ behaves quite differently, however, in that the displacements are referenced to the *same* atom, and $G_s^{cl}(\vec{r},0)$ must therefore be a delta function located at $\vec{r}=0$. Consequently, the time dependence of $G_s^{cl}(\vec{r},t)$ is far more dramatic. Indeed, as illustrated in Fig. 4-7 for graphite, $G_s^{cl}(\vec{r},t)$ undergoes significant changes over time, collapsing from a delta function to a broadening Gaussian peak whose center shifts away from the origin over time. In the case of a liquid or gas, the broadening process proceeds ad infinitum.

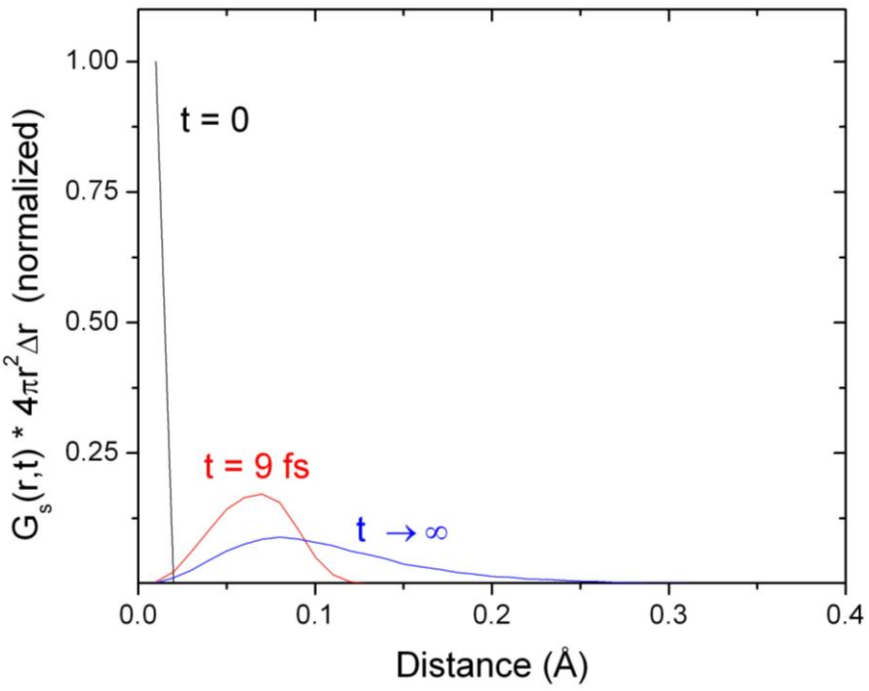

Fig. 4-7. Time dependence of the self part of G(r,t) at 300K. The displacement bin interval, Δr, is 0.01 Å.

4.4 Incoherent Thermal Scattering in Graphite

Numerical Fourier transformation of $G^{cl}(\vec{r},t)$ over time and space produces the dynamic structure factor, S(κ,ω). In the present work, S(κ,ω) is evaluated from the time Fourier transform of I(κ,t) directly such that κ is specifiable as an input variable. Otherwise, values of κ would be dictated by the range and bin spacing of r in the $G^{cl}(\vec{r},t)$ histogram.

Molecular dynamic simulations of perfect graphite were carried out initially at 300 K under the NVT ensemble (constant number, volume, and temperature). For cross section calculation purposes, the time-dependent positions of the centermost atoms (256 in number)

were recorded following a period of equilibration lasting 10 picoseconds. System temperature was held constant using a thermal bath along the outer edge of the supercell (and therefore at a location significantly removed from those atoms involved in cross section analysis). Jumps in the atomic positions due to periodic boundary conditions were removed in a post-processing program. From the positions of the atoms over a period of 131,072 time steps (65.5 picoseconds), the intermediate function, scattering law, differential cross section, and total inelastic cross section were assessed.

At the chosen time step of 0.5 femtoseconds (dictated by the stability of the numerical integration algorithm), the maximum discernable frequency in any derived quantity would be:

$$\omega_{\max} = \frac{1}{2\Delta t} = 1000\ THz \tag{4.8}$$

which is termed the *Nyquist frequency* in the parlance of discrete Fourier transformation. The most energetic vibrational modes of graphite are known to oscillate at approximately 50 THz, and so the selected time step is certainly small enough for comprehensive analysis of $S(\kappa,\omega)$. Given Δt and the total number of steps, the nominal frequency bin width will be:

$$\Delta\omega = \frac{1}{2N\Delta t} = 0.0076\ THz \tag{4.9}$$

for the specific case discussed above. Because this $\Delta\omega$ is much finer than what is needed to investigate significant features of the scattering law, $S(\kappa,\omega)$ is collapsed onto a courser mesh along the frequency axis. The rationale for the coarsening operation is statistical; by summing individual estimates of the transform, the variance of the summed estimate is

reduced by a factor of $1/N$, where N is the number of values in the summation [67]. This reduces the noise inherent in individual $S(\kappa,\omega)$ data points , while also purging spurious negative values of $S(\kappa,\omega)$.

The classical moment rules are a useful initial check on the accuracy of the MD intermediate function and Fourier transformation procedure. An analysis of the calculated 0^{th} and 2^{nd} moments in Fig. 4-8 reveals good agreement with the exact theoretical relations of Section 3.1.4. These moment rules were found to be satisfied regardless of temperature or state of matter, given that no discontinuities exist in the atomic positions (e.g. due to period boundary conditions).

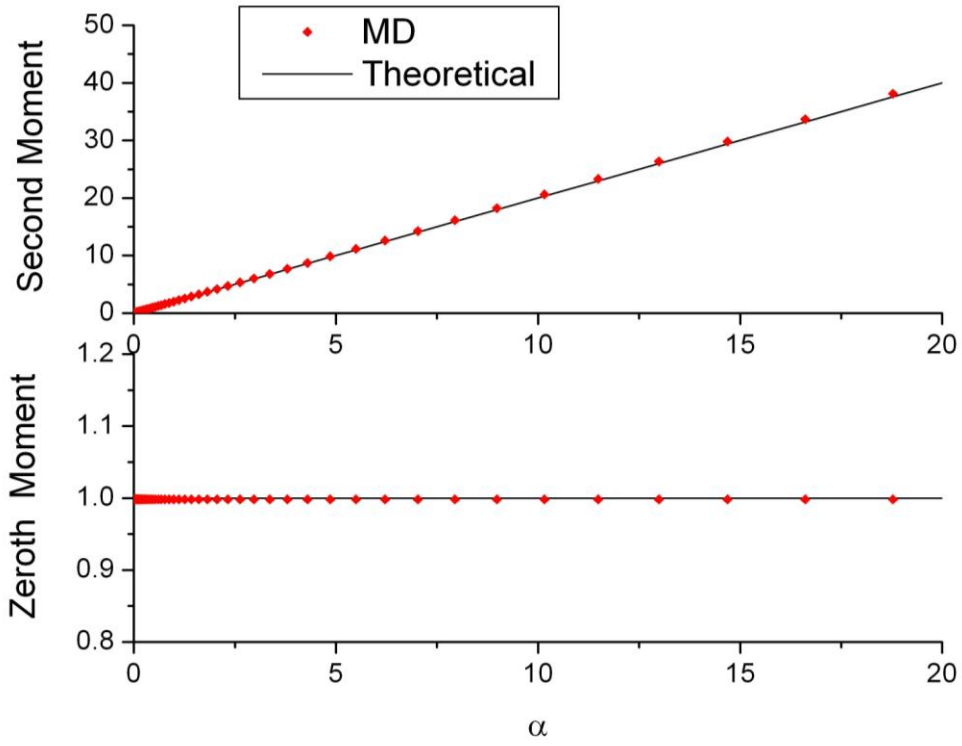

Fig. 4-8. Classical moments of the MD-derived $S^{cl}(\kappa,\omega)$ at 300 K

Another useful check is the low-α limit of $S_s(\alpha,\beta)$ (either classical or quantum), which is proportional to the phonon density of states.

4.4.1 ρ(ω) from S(α,β)

The density of states, in this case, is a byproduct of the scattering law calculation. Assuming a Gaussian shape for I(κ,t), the relevant relation is:

$$\rho(\omega) = \frac{2M\hbar\omega^2}{k_B T}\lim_{\kappa\to 0}\left[\frac{S_s^{cl}(\kappa,\omega)}{\kappa^2}\right] = \frac{\hbar}{k_B T}\beta^2 \lim_{\alpha\to 0}\left[\frac{S_s^{cl}(\alpha,\beta)}{\alpha}\right] \tag{4.10}$$

where *M* is the scatterer mass. In the MD correlation function approach, the S_s of Eq. (4.10) is essentially the classical scattering law to which quantum or semiclassical corrections have not yet been applied. It should be noted that the form of the S(κ,ω) → ρ(ω) relation is dependent upon the system model under consideration. For example, if the system is composed of interacting quantum harmonic oscillators, then

$$\rho(\beta) = \left(\frac{\hbar}{k_B T}\right) 2\beta \sinh\left(\beta/2\right) \lim_{\alpha\to 0}\left[\frac{\tilde{S}_s(\alpha,\beta)}{\alpha}\right] \tag{4.11}$$

is the appropriate equation, where $\tilde{S}_s$ is now the symmetrized quantum incoherent scattering law. A step-by-step derivation of Eqs. (4.10) and (4.11) is provided in Appendix B. These relations are, in fact, identical in the classical limit of small beta (i.e. high temperature)

The density of states determined from Eq. (4.10) is shown in Fig. 4-9. From this figure, it is seen that ρ(ω) as the low-α limit of $S_s(\alpha,\beta)$ agrees almost exactly with ρ(ω) from the velocity

autocorrelation function. To the extent that the computed $S_s(\alpha,\beta)$ is consistent with the low-order moment rules, $\rho(\omega)$ from Eqs. (4.10) and (4.11) automatically exhibits the proper normalization. The importance of coarsening the frequency mesh is also apparent in Fig. 4-9; collapsing $S_s(\alpha,\beta)$ by a factor of 32 transforms $\rho(\omega)$ from a noisy, unrecognizable signal to a lucid distribution.

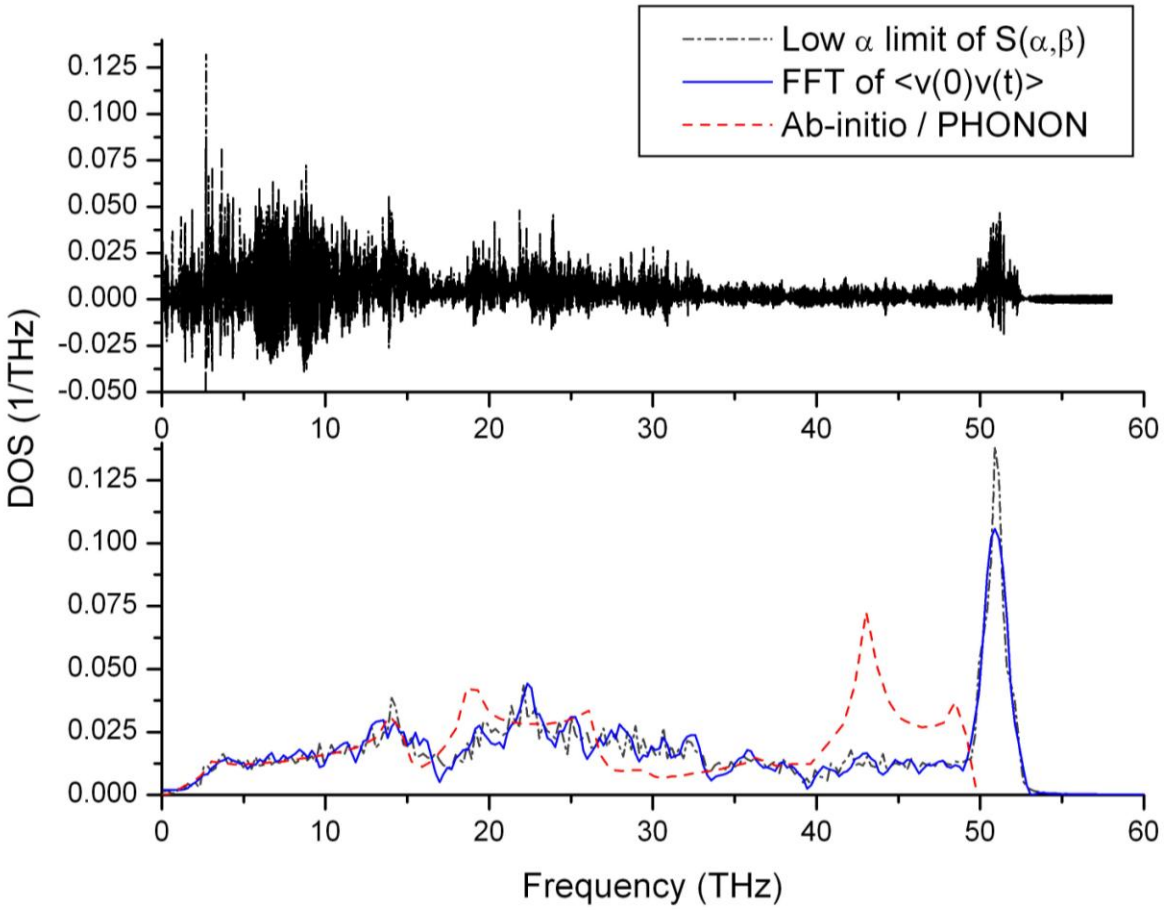

Fig. 4-9. Phonon density of states as the low alpha limit of S(κ,ω) before collapsing the frequency domain (top panel) and after collapsing by a factor of 32 (bottom panel).

The scattering cross section is extremely sensitive to the behavior of $S(\kappa,\omega)$ as low frequencies, and this region consequently requires special consideration. Since low frequency vibrations require more time for the completion of a cycle, the low-ω portion of $S(\kappa,\omega)$ is statistically the least sampled portion of the function,. On theoretical grounds, the incoherent scattering law is expected to be flat in the immediate vicinity of $\omega = 0$ and $\kappa = 0$; this is equivalent, in the limit of small momentum transfers, to an exactly parabolic trend in the lowest energy portion of the phonon density of states. A parabolic fitting procedure has been performed previously in conjunction with *ab-initio* / PHONON / NJOY calculations of the graphite cross section [14]. In that work, a parabolic cutoff of 5.606 meV (1.36 THz) was justified physically and was furthermore demonstrated to generate good agreement with experimental cross section data. The stated parabolic range corresponds to a "flat-top" extrapolation of the scattering law below $\omega = 1.36$ THz, which was used as a guideline in all MD calculations of $S_s(\kappa,\omega)$.

4.4.2 Effect of Semiclassical Corrections

The classical scattering law was shown to lack critical information regarding thermal occupancy and atomic recoil, therefore bringing about severe discrepancies in the differential energy spectra. A reasonable first approach to correcting this problem is to introduce the semiclassical correction factors discussed in Chapter 3, which are simple to implement in frequency space. To this end, the impact of each of the proposed correction factors on the

inelastic cross section is now assessed. Cross section calculations were carried out in accordance with the following procedural chain:

$$\left\{\vec{r}_j\right\} \rightarrow I_s^{cl}\left(\kappa,t\right) \rightarrow S_s^{cl}\left(\kappa,\omega\right) \rightarrow Q\left(\omega\right)\cdot S_s^{cl}\left(\kappa,\omega\right) \rightarrow \frac{d\sigma}{dE'} \rightarrow \sigma\left(E\right)$$

where the selected reciprocal-space grid spans 120 points that are spaced logarithmically between 1.0 nm^{-1} and 1500.0 nm^{-1}. In all cases, the DC (elastic) component of the time Fourier transform was subtracted from the scattering law. The total inelastic cross section associated with each semiclassical correction formula is displayed in Fig. 4-10, and the corresponding 1st order moments are plotted in Fig. 4-11.

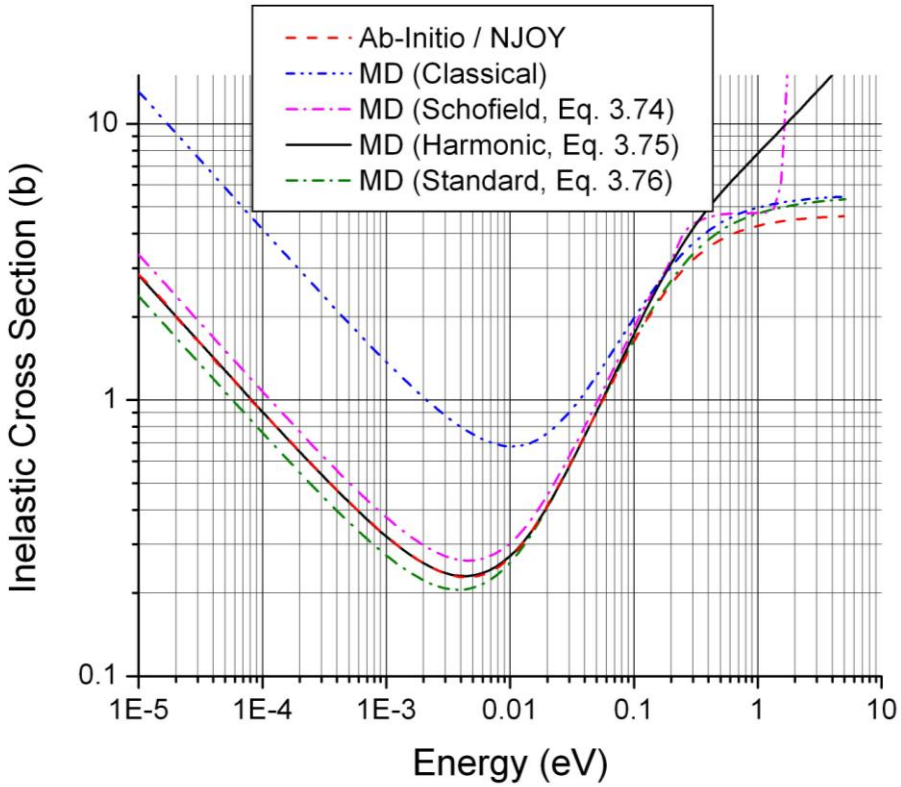

Fig. 4-10. Inelastic incoherent cross section at 300 K, with and without semiclassical corrections to $S^{cl}(\alpha,\beta)$.

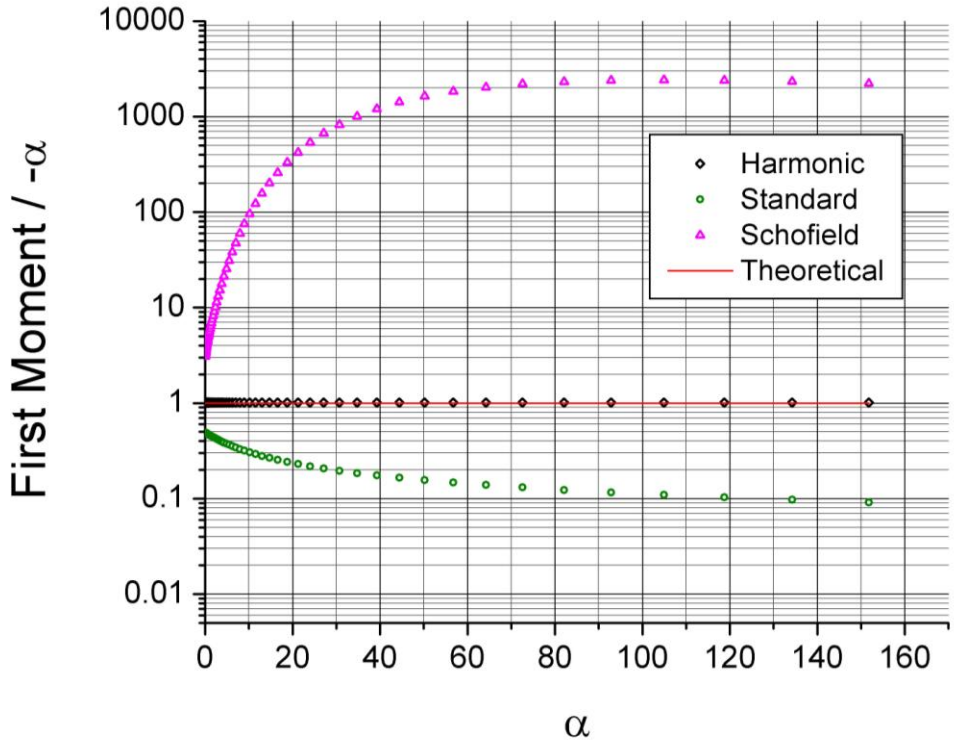

Fig. 4-11. First moment of $S_s(\alpha,\beta)$, normalized to the theoretical value.

From Fig. 4-10, it is clear that all of the semiclassical correction functions result in improved agreement with the *ab-initio* based cross section at energies below 0.1 eV. None of the semiclassical functions, however, steers the cross section to the correct free atom limit. Still, some perform better than others in graphite, and the harmonic correction in particular is seen to match *ab-initio* / lattice dynamical calculations remarkably well up to 0.1 eV. The Schofield-modified cross section blows up above 1 eV due the exponential growth it induces in the scattering law at large, positive values of beta. Divergence from the free atom cross section is also observed following application of the harmonic correction factor, which scales linearly with positive beta at large beta. The standard correction function, on the other hand,

asymptotically approaches a constant value as $\beta \to \infty$, and the resulting cross section saturates to a constant (σ_B) as well.

An important question is: Why does the harmonic correction fit *ab-initio* based results particularly well below 0.1 eV relative to the other semiclassical factors? To answer this question, it is productive to first consider the position correlation function of a system of harmonic oscillators, defined as:

$$C(t) = \langle q(t) q(0) \rangle \tag{4.12}$$

in which q is the collective coordinate:

$$q = \sum_k c_k \left(b_k^* + b_k \right) \tag{4.13}$$

where c_k are the expansion coefficients, b_k^* is the creation operator and b_k is the annihilation operator. In this case, the exact quantum correlation function:

$$C(t) = \int_0^\infty d\omega \rho(\omega) \left[\left(\frac{\exp\left(\frac{\hbar\omega}{k_B T} \right)}{\exp\left(\frac{\hbar\omega}{k_B T} \right) - 1} \right) \exp(-i\omega t) + \left(\frac{1}{\exp\left(\frac{\hbar\omega}{k_B T} \right) - 1} \right) \exp(i\omega t) \right] \tag{4.14}$$

and the classical function:

$$C^{cl}(t) = \frac{2k_B T}{\hbar} \int_0^\infty d\omega \frac{\rho(\omega)}{\omega} \cos(\omega t) \tag{4.15}$$

are related through a simple derivative:

$$C_I(t) = \frac{\hbar}{2k_B T} \frac{d}{dt} C^{cl}(t) \tag{4.16}$$

which is equivalent to the time-domain expression for the harmonic correction. In fact, a more general statement can be made that the harmonic correction is exact when the quantity being correlated is a linear function of the particle positions or momenta [56]. The particle density operator, $\exp\left(i\vec{\kappa}\cdot\vec{R}_j(t)\right)$, is linearly dependent on position only when κ is small. This applies in the linear response regime, where a momentum transfer from the neutron to the scattering system constitutes a mere perturbation to the atomic trajectories. Therefore, the harmonic correction produces the correct cross section at low incident energies for which the momentum transfer is small, and subsequently breaks down at higher energies where the scattered atom recoils strongly. This suggests that additional correction is needed at large κ where recoil is dominant.

Interestingly, the harmonic correction represents a well-defined classical limit of generic quantum time correlation functions. This is demonstrable through the Kubo transform of the correlated operators. In general, for operators $\hat{x}$ and $\hat{y}$, the quantum correlation function is defined by [68]:

$$C_{xy}(t) = Tr\left(\hat{x}'\frac{1}{Z}\exp\left[\frac{i\hat{H}t}{\hbar}\right]\hat{y}\exp\left[\frac{-i\hat{H}t}{\hbar}\right]\right) \tag{4.17}$$

where:

$\hat{x}' = \exp\left(\frac{\hat{H}}{k_B T}\right)\hat{x}$ generates the standard asymmetric function

$\hat{x}' = \exp\left(\frac{-\hat{H}}{2k_B T}\right)\hat{x}\exp\left(\frac{-\hat{H}}{2k_B T}\right)$ generates the symmetrized function

$\hat{x}' = k_B T \int_0^{1/k_B T} d\varepsilon \exp\left(-\left[\frac{1}{k_B T} - \varepsilon \right] \hat{H} \right) \hat{x} \exp\left(-\varepsilon \hat{H} \right)$ produces the Kubo transformed function

in which *Z* is the partition function. These three versions of the correlation function are related, in frequency space, by multiplicative factors as:

$$\frac{\frac{\hbar\omega}{k_B T}}{1 - \exp\left(-\frac{\hbar\omega}{k_B T} \right)} C_{xy}^{Kubo}(\omega) = C_{xy}(\omega) = \exp\left(\frac{\hbar\omega}{2k_B T} \right) C_{xy}^{sym}(\omega) \tag{4.18}$$

where, substituting the particle density operators in place of $\hat{x}$ and $\hat{y}$, it is apparent that the scattering law is one possible form of the function $C_{xy}(\omega)$. In the classical limit, the Kubo transform of an operator becomes the classical expression for that operator [69]. Therefore, to the extent that the classical limit is valid (for example at high temperatures or for small energy and momentum transfers):

$$S(\kappa,\omega) \cong \frac{\frac{\hbar\omega}{k_B T}}{1 - \exp\left(-\frac{\hbar\omega}{k_B T} \right)} S^{cl}(\kappa,\omega) \tag{4.19}$$

$$= C(\omega) S^{cl}(\kappa,\omega)$$

where the scaling factor, $C(\omega)$, is identical to the harmonic correction of Eq. (3.75).

The MD asymmetric scattering law, with the inclusion of the harmonic correction term, is compared against its *ab-initio* / NJOY counterpart in Fig. 4-12. Agreement at large β is particularly noteworthy because this is precisely the region that is most influenced by the

specific form of the semiclassical correction. In general, the performance of the harmonic correction is quite satisfactory except at high incident energies.

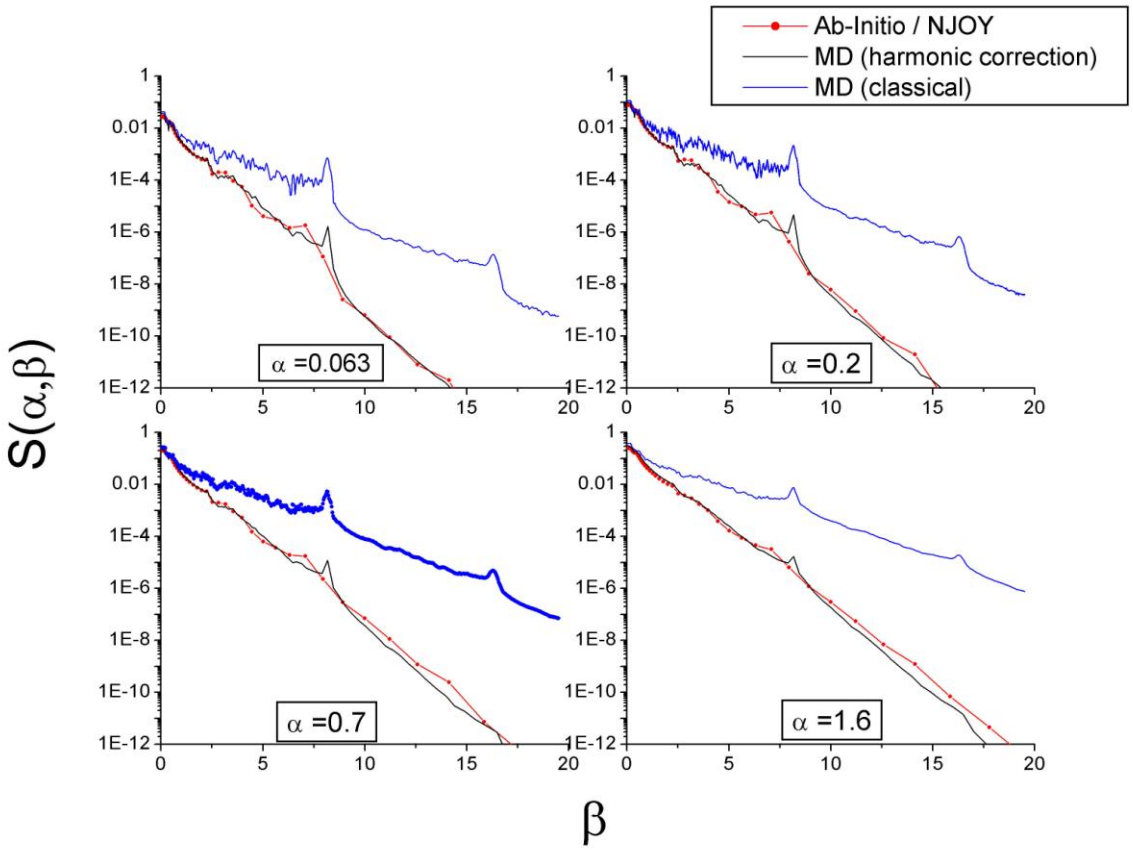

Fig. 4-12. Asymmetric scattering law as a function of positive beta, at select values of alpha. The harmonic semiclassical correction has been applied to $S_s(\alpha,\beta)$.

In the case of an ideal harmonic oscillator, exact formulae are known for the classical, quantum, and semiclassical scattering law, and Kaplan and Zweifel [70] have established a range of validity for the semiclassical approximation. By expanding the quantum scattering law and comparing against the semiclassical version, they have shown that the latter is justified when α 12. This result accords well with the observed non-functionality of the harmonic correction at high incident energies where the recoil effect dominates.

4.4.3 Classical / Quantum I(κ,t) Relation

The harmonic correction is numerically robust and transferable to any solid state system; however, the breakdown of semiclassical corrections at high α remains a severe impediment to its implementation. To the extent that atoms in the MD system oscillate about well-defined lattice positions, which is quite true except near the melting point, a comprehensive time-domain transformation between the classical and quantum functions can, in fact, be devised. This is demonstrable from the analytic $I_s^{cl}(\kappa,t)$ expression for a harmonic oscillator system, given by:

$$I_s^{cl}(\kappa,t) = \exp\left(-\frac{k_B T \kappa^2}{M}\int_0^\infty \frac{d\omega\rho(\omega)}{\omega^2}\left[1-\cos(\omega t)\right]\right) \tag{4.20}$$

or, in terms of dimensionless quantities:

$$I_s^{cl}(\kappa,t') = \exp\left(-\alpha\int_{-\infty}^{\infty} \frac{d\beta\rho(\beta)}{\beta^2}\left[1-\cos(\beta t')\right]\right) \tag{4.21}$$

where t' is time in units of $\hbar/k_B T$ seconds. The exact quantum function, in comparison, is given by:

$$I_s(\kappa,t') = \exp\left(-\alpha\int_{-\infty}^{\infty} \frac{d\beta\rho(\beta)\exp(\beta/2)}{2\beta\sinh(\beta/2)}\left[1-\cos(\beta t')-i\sin(\beta t')\right]\right) \tag{4.22}$$

as was derived in Chapter 3. Significant differences between the classical and quantum functions include the presence of the sine term and:

$$\frac{1}{\beta^2} \rightarrow \frac{\exp(\beta/2)}{2\beta\sinh(\beta/2)} \tag{4.23}$$

in the integrand, where the RHS reduces to the LHS in the low-β limit. The procedure for transforming the classical function to the corresponding quantum version is then as follows.

A function $f(\beta)$ is defined as:

$$f(\beta) = \rho(\beta)/\beta^2 \tag{4.24}$$

and the integral in the RHS of Eq. (4.21) is isolated by taking the logarithm of both sides:

$$\frac{\ln\left[I_s^{cl}(\kappa,t')\right]}{-\alpha} = \int_{-\infty}^{\infty} d\beta f(\beta)\left[1-\cos(\beta t')\right] \tag{4.25}$$

$$= \lambda - \int_{-\infty}^{\infty} d\beta f(\beta)\cos(\beta t')$$

where:

$$\lambda = \int_{-\infty}^{\infty} d\beta f(\beta) \tag{4.26}$$

is the classical analogue of the Debye-Waller lambda. Integrating through by $\cos(\mu t')$, where μ is a dummy variable:

$$\int_{-\infty}^{\infty} dt'\lambda\cos(\mu t') - \int_{-\infty}^{\infty} d\beta f(\beta)\int_{-\infty}^{\infty} dt'\left[\cos(\mu t')\cos(\beta t')\right] \tag{4.27}$$

$$= \int_{-\infty}^{\infty} dt'\lambda\cos(\mu t') - \int_{-\infty}^{\infty} d\beta f(\beta)\left[\frac{\sin\left((\mu-\beta)t'\right)}{2(\mu-\beta)} + \frac{\sin\left((\mu+\beta)t'\right)}{2(\mu+\beta)}\right]_{t'=-\infty}^{t'=\infty}$$

$$= \int_{-\infty}^{\infty} dt'\lambda\cos(\mu t') \; + \; f(\mu)$$

so that:

$$f(\mu) = \int_{-\infty}^{\infty} dt' \cos(\mu t') \left(\frac{\ln\left[I_s^{cl}(\kappa, t') \right]}{-\alpha} - \lambda \right) \tag{4.28}$$

where the RHS depends solely on MD trajectory data. From relation (4.23), the quantum version of $f(\mu)$ is defined as:

$$f^q(\mu) = \frac{\mu \exp(\mu/2)}{2\sinh(\mu/2)} f(\mu) \tag{4.29}$$

which, substituted back into Eq. (4.22), gives:

$$I_s(\kappa, t') = \exp\left(-\alpha \int_{-\infty}^{\infty} d\mu f^q(\mu) \left[1 - \cos(\mu t') - i \sin(\mu t') \right] \right) \tag{4.30}$$

where the sinusoidal integrals on the RHS can evaluated from the real (cosine) and imaginary (sine) components of discrete Fourier transforms. The quantum factors $f^q(\mu)$ and $i\sin(\mu t')$ may be interpreted in the following way: $f^q(\mu)$ transforms the classical version of the occupancy factor (i.e. the phonon equivalent of the Rayleigh-Jeans distribution) to the Planck distribution, while $i\sin(\mu t')$ defines the system response due to an external impulse. These attributions are made clear through an examination of the derivation of Eq. (3.94), in which the classical-quantum correspondence principle was utilized to replace the quantum mechanical commutator with classical Poisson brackets. Specifically, the sinusoidal term originates from Eq. (3.92), whereas the function $f^q(\mu)$ follows by taking the ratio of the bracketed term of Eq. (3.93) to its classical analogue.

In summary, the real and imaginary parts of the quantum intermediate scattering function have been expressed as a transformation of the classical (MD-derived) function. The Fourier transform of Eq. (4.30) over time yields the quantum-corrected scattering law, which satisfies both detailed balance and the first-order moment rule. Fulfillment of the detailed balance condition is shown explicitly in Fig. 4-13. In the limit of small α, the proposed classical-to-quantum transformation of $I^{cl}(\kappa,t)$ reduces to the harmonic semiclassical correction of Eq. (3.75). This is proven in Appendix C.

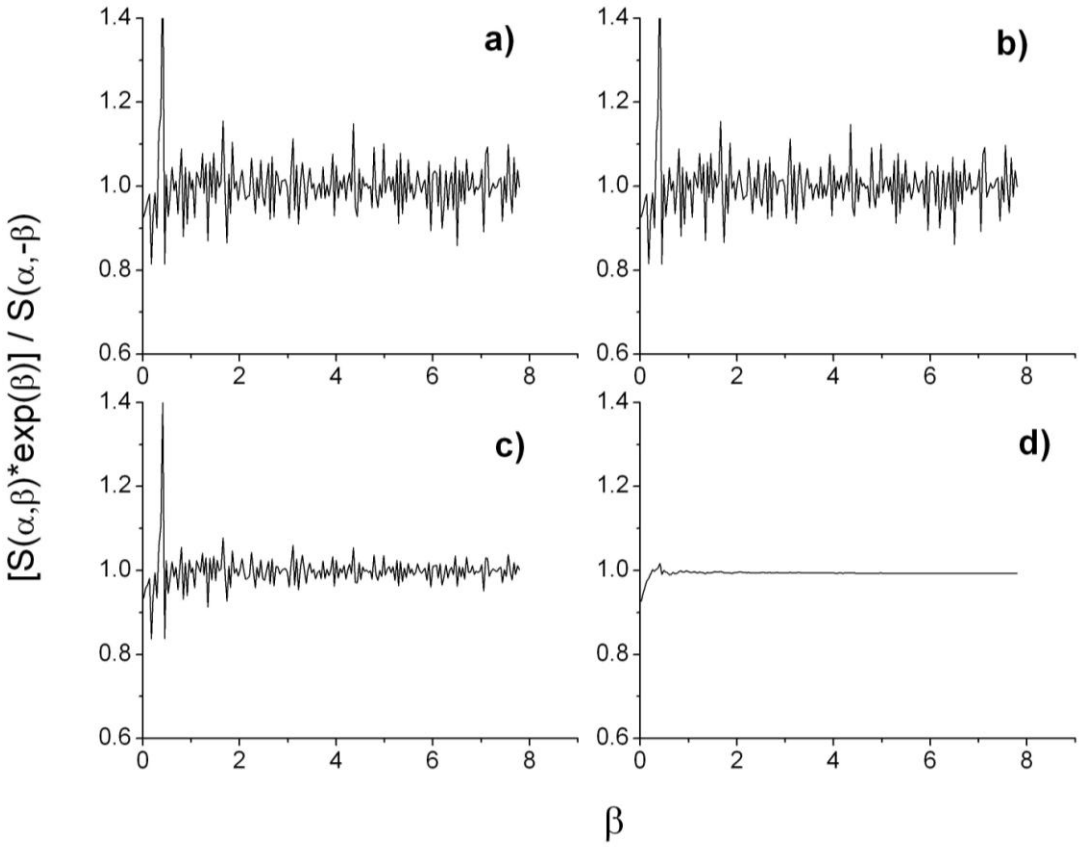

Fig. 4-13. Detailed balance ratio at a) α = 1E-4; b) α = 1E-3 ; c) α = 1 ; and d) α = 10. A ratio of unity indicates agreement with the detailed balance relation.

4.4.3.1 Intermediate Function

As quantum effects are incorporated into the real, classical intermediate function, the reaction of the scattering system to the neutron interaction is manifested in the imaginary part of $I(\vec{\kappa},t)$. The detailed nature of this response formally depends upon both the direction and magnitude of the momentum transfer; however, in general terms, the system response would be expected to increase in magnitude with $|\kappa|$ and approach the free atom limit as $|\kappa|$ becomes very large. Fig. 4-14 shows the real and imaginary parts of $I(\vec{\kappa},t)$ at 300 K, as a function of $|\kappa|$ and *t*. The behavior of $I(\vec{\kappa},t)$ at very large $|\kappa|$ is displayed separately in Fig. 4-15.

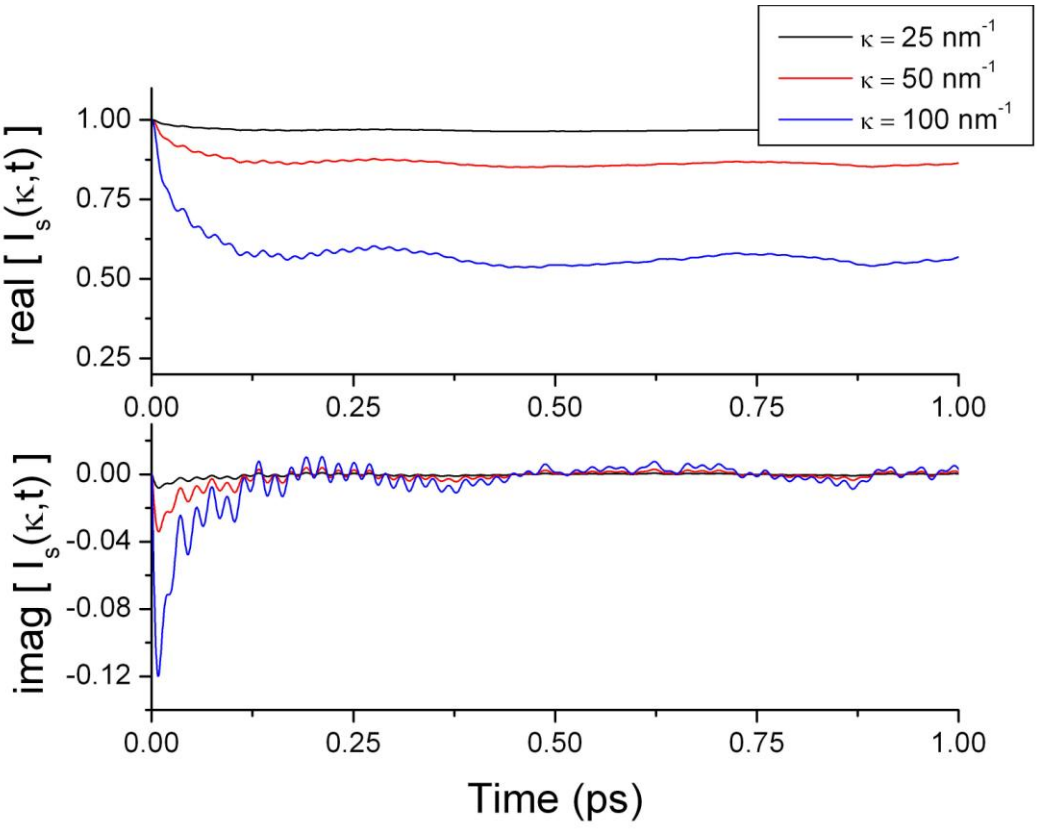

Fig. 4-14. Time dependence of the real and imaginary parts of $I_s(\kappa,t)$, Eq. (4.30), at 300 K.

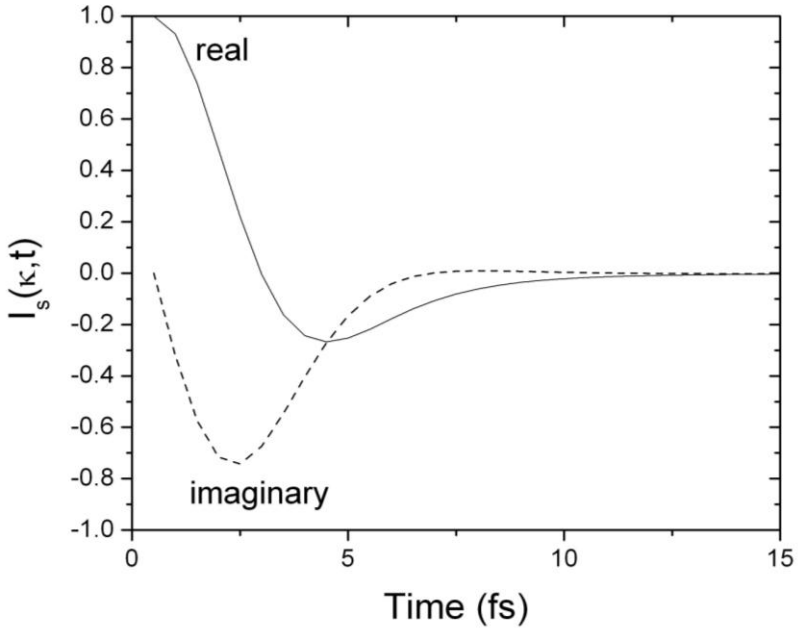

Fig. 4-15. Time dependence of the real and imaginary parts of $I_s(\kappa,t)$, Eq. (4.30), at κ=500 nm^{-1} (in the free atom response regime of κ).

As anticipated, the imaginary part of $I(\vec{\kappa},t)$ increases monotonically with $|\kappa|$, eventually approaching the same magnitude as the real part. At all values of $|\kappa|$, the imaginary part scales linearly with *t* at short times in accordance with the exact free atom relation of Eq. (3.90). This is especially evident at very large $|\kappa|$ where the density autocorrelation dies out quickly and small-scale oscillations in $I(\vec{\kappa},t)$ are overshadowed by the transient, short-time response.

The convergence of the imaginary part of $I(\vec{\kappa},t)$ to the free-atom Poisson bracket equation is numerically demonstrable. At short times, the exact free atom expression for the imaginary part of $I(\vec{\kappa},t)$ simplifies to:

$$I_I(\kappa,t) \;=\; imag\left\{ I_s^{cl}(\kappa,t)\exp\left[\frac{i\hbar\kappa^2 t}{2M}\right]\right\} \;\cong\; \frac{-\hbar\kappa^2 t}{2M} \tag{4.31}$$

where $I_s^{cl}(\kappa,t) \cong 1$ in the aforementioned limit. Consistency with Eq. (4.31) can be validated by ascertaining the slope of the computed intermediate function with respect to time (at various momentum transfers) and comparing against the analytic expression of the free atom. The short-time behavior of $I_I(\kappa,t)$ is shown in Fig. 4-16, and an analysis of the fitted slopes is given in Fig. 4-17. Agreement with Eq. (4.31) is indeed observed, signifying that the proposed classical-quantum transformation expression reduces to the expected free atom limit. On a side note, the striking similarity between the free atom prefactor ($\hbar\kappa^2/2M$) and the 1st-moment sum rule is not coincidental, since both relate to the scattering system response.

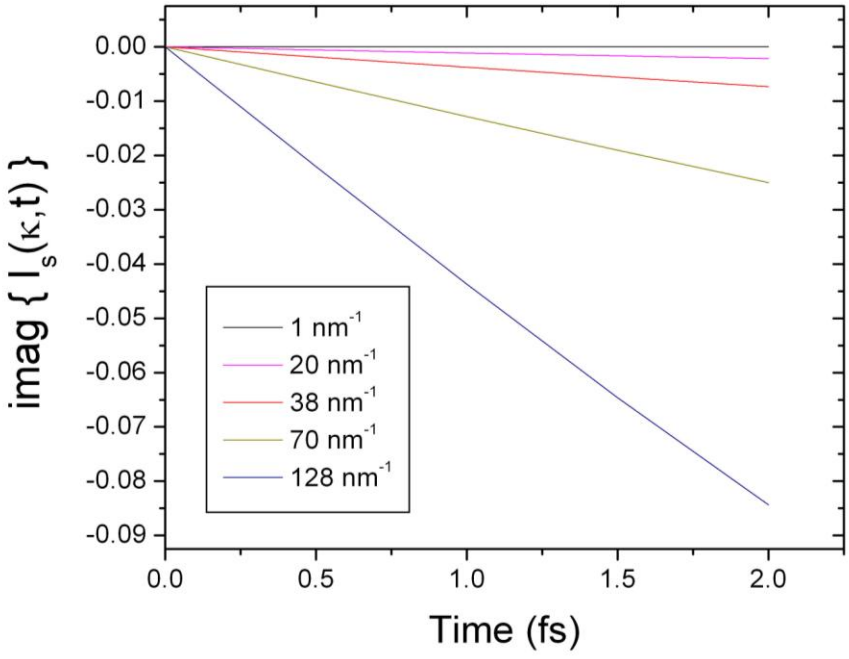

Fig. 4-16. Imaginary part of $I_s(\kappa,t)$, Eq. (4.30), in the short time limit

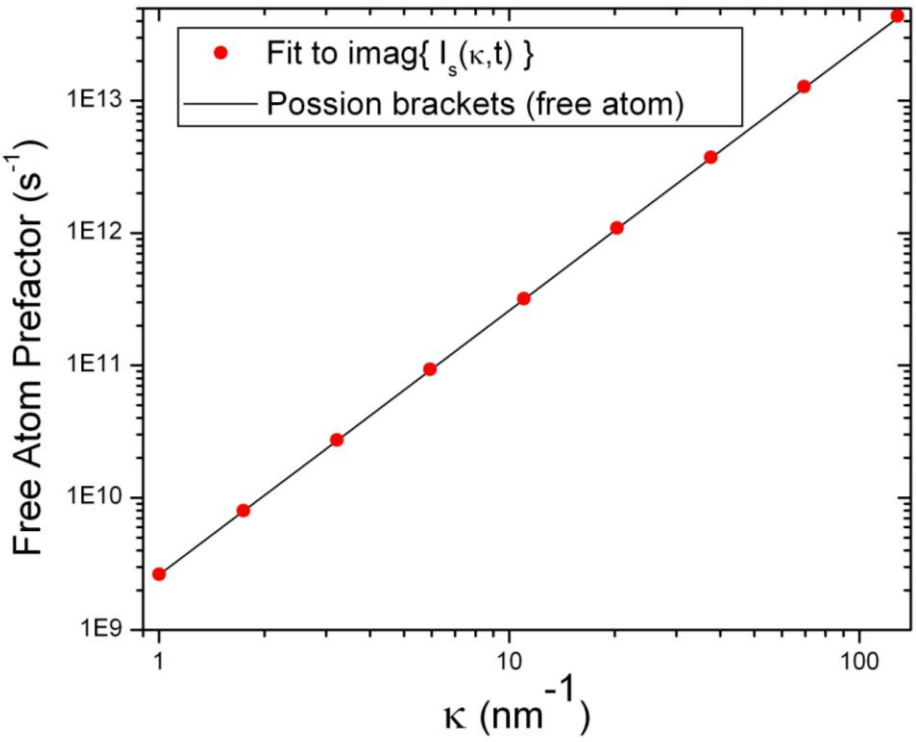

Fig. 4-17. Slope of the imaginary part of $I_s(\kappa,t)$, Eq. (4.30), in the short time limit vs. the predicted slope from the free atom Poisson bracket expression.

4.4.3.2 Scattering Law

The quantum-corrected MD scattering law at 300 K is plotted in Fig. 4-18 alongside *ab-initio* / NJOY calculations as well as the ENDF/B-VII standard. All are seen to converge in the high alpha limit, but significant differences exist at lower values of alpha due to disparities between the *ab-initio* and Young-Koppel (ENDF) densities of state. MD scattering law calculations follow the validated *ab-initio* derived results quite closely through a wide range of alpha and beta, demonstrating the suitability of both the quantum correction methodology and the (classical) dynamics of the MD graphite system.

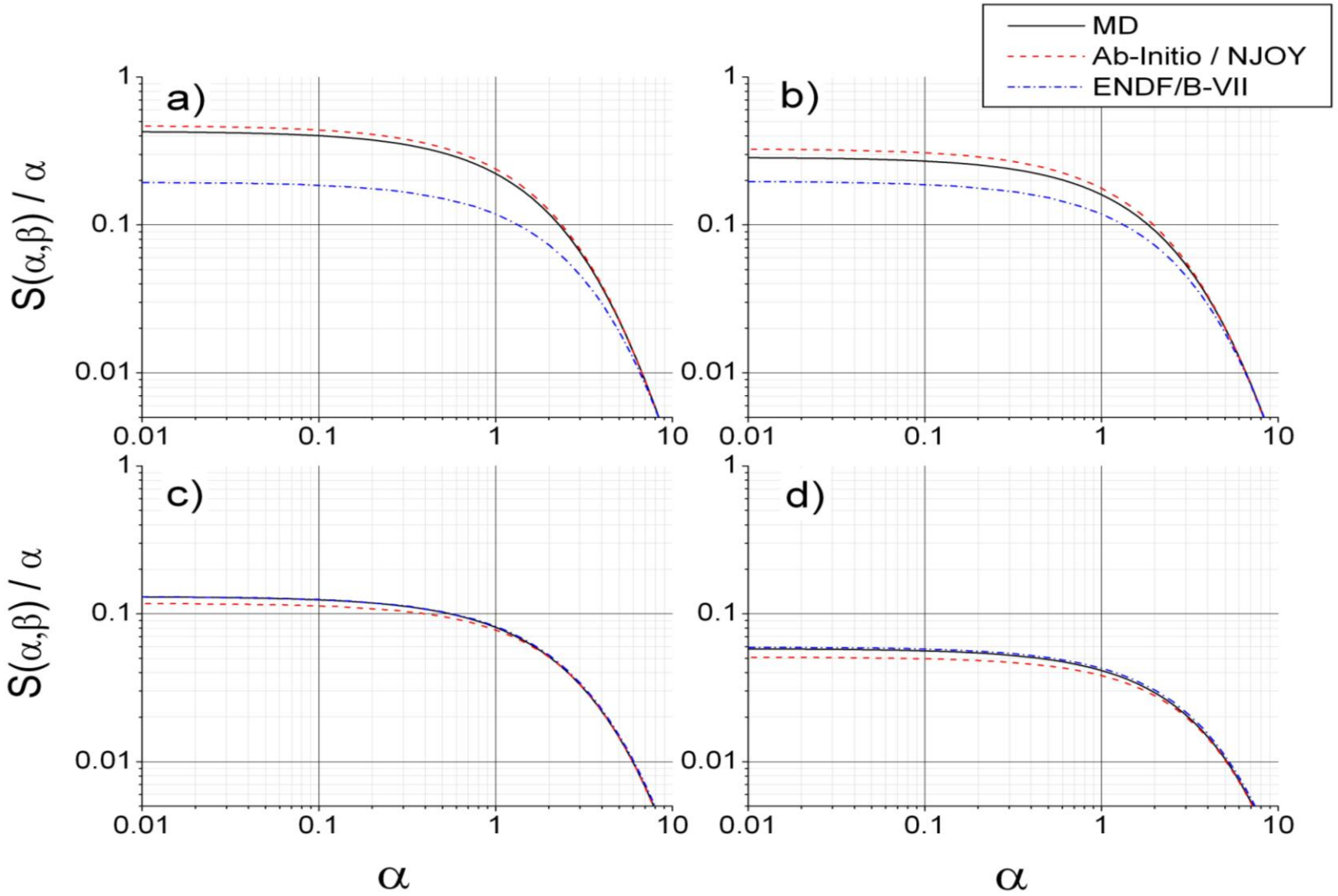

Fig. 4-18. Symmetric scattering law at 300 K and a) β = 0.2 ; b) β = 0.4 ; c) β = 0.8 ; and d) β = 1.

4.4.3.3 Cross Section

The proposed real-imaginary I(κ,t) transformation has been proven to obey the detailed balance and free atom relations in the appropriate limits. Fig. 4-19 and Fig. 4-20 show the derived total and differential scattering cross sections as compared to the semiclassical harmonic correction, in which the relevant quantum effects were introduced through a frequency-domain adjustment factor. The real-imaginary I(κ,t) transformation is observed to produce differential cross sections that are consistent with the *ab-initio* / NJOY standard at all incident energies. Thus, the classical scattering functions – which severely overestimate the graphite cross section – have been brought into line with experimental data through the incorporation of the imaginary components of G(r,t) and I(κ,t).

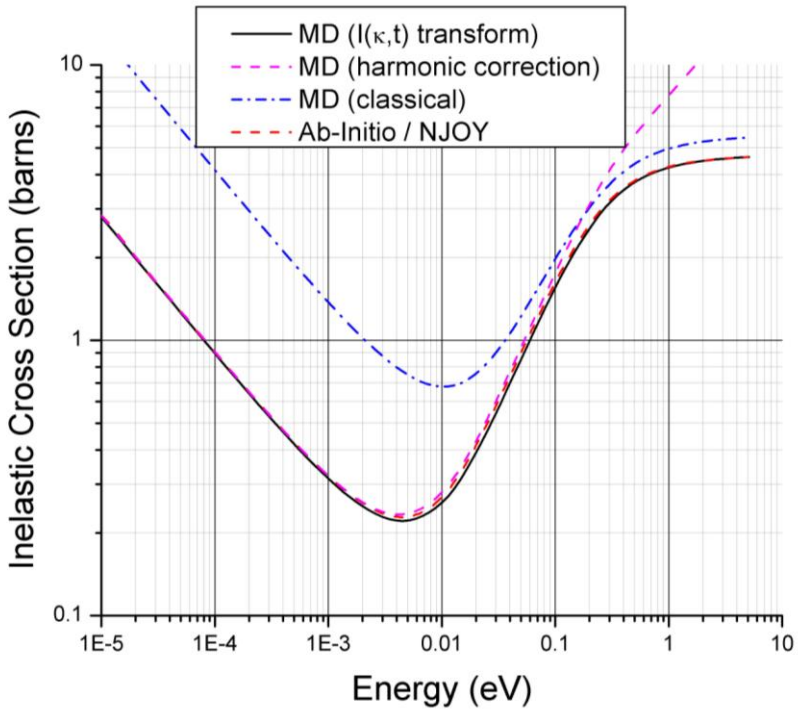

Fig. 4-19. Comparison of the total cross section generated under the proposed harmonic semiclassical and I(κ,t) transform schemes.

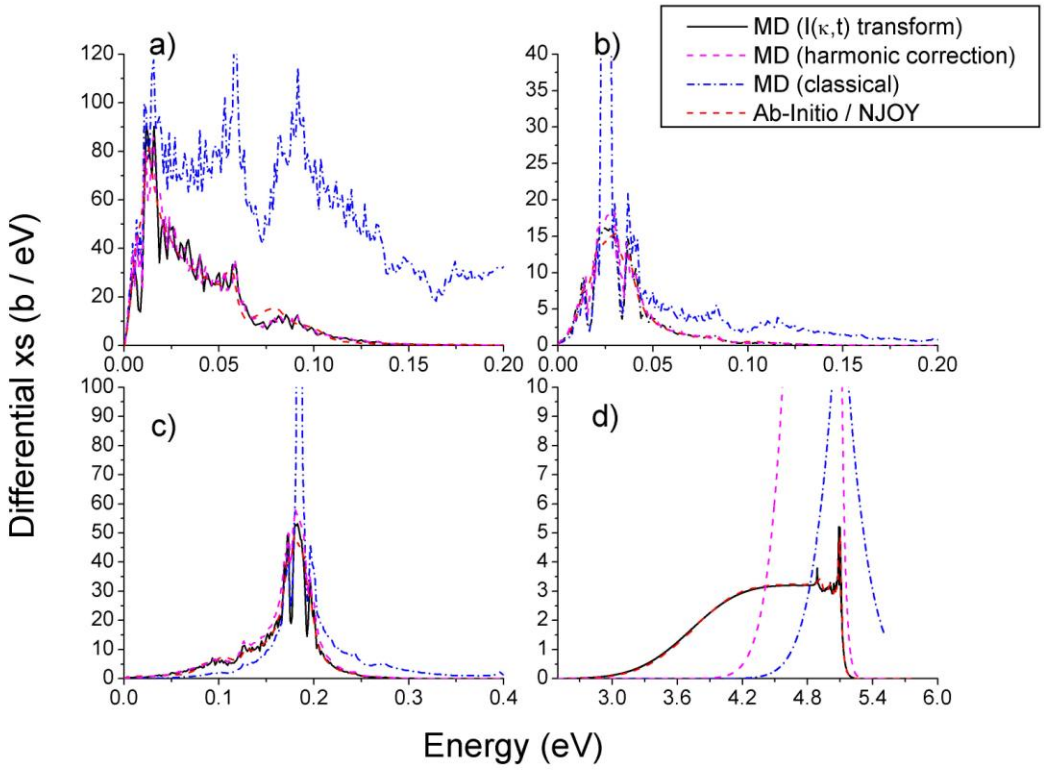

Fig. 4-20. Comparison of the differential cross sections generated under the proposed harmonic semiclassical and I(κ,t) transform schemes at a) 1E-5 eV, b) 0.0253 eV, c) 0.184 eV and d) 5.1 eV.

4.4.4 Moment Analysis

The zeroth and first order moments of the scattering law, in dimensionless form, are governed by the following general relations:

$$\int_{-\infty}^{\infty} d\beta \cdot S(\alpha,\beta) = 1 \qquad [\textit{with elastic peak}] \tag{4.32}$$

$$\int_{-\infty}^{\infty} d\beta \cdot S(\alpha,\beta) = 1 - \exp(-\lambda\alpha) \quad [\textit{without elastic peak}] \tag{4.33}$$

$$\int_{-\infty}^{\infty} d\beta \cdot \beta \cdot S(\alpha,\beta) = -\alpha \tag{4.34}$$

where λ is the Debye-Waller lambda, defined by:

$$\lambda = \int_{-\infty}^{\infty} \frac{d\beta \cdot \rho(\beta) \exp\left(-\beta/2\right)}{2\beta \sinh\left(\beta/2\right)} \tag{4.35}$$

which is related to the relative contribution of the elastic peak to the zeroth moment. Since the elastic peak is of no interest in the present work, the appropriate version of the zeroth moment is that given in Eq. (4.33). This is also the version that is implemented, for example, in the LEAPR code.

Insight into the MD Debye-Waller λ can be gleaned by fitting the zeroth moment (without elastic peak) to Eq. (4.33), where λ is the sole fitting parameter. This fit is shown in Fig. 4-21 alongside the calculated moments of the MD scattering law. The RHS of Eq. (4.33) is seen to match the MD data rather well, producing a best fit value of 0.891 for λ. By comparison, the direct computation of λ using the *ab-initio* frequency distribution results in a value of 0.897 for λ – a deviation of less than 1% from the MD value.

The first-order moment of the MD scattering function is seen to agree with theoretical expectations, matching Eq. (4.34) to within a few percent except at extremely high alpha. Due to the close interrelation between quantum effects and the first-order moment, agreement with Eq. (4.34) is viewed as essential in validating the MD quantum correction scheme developed here. In the absence of such agreement, the cross section does not converge to the correct free atom limit.

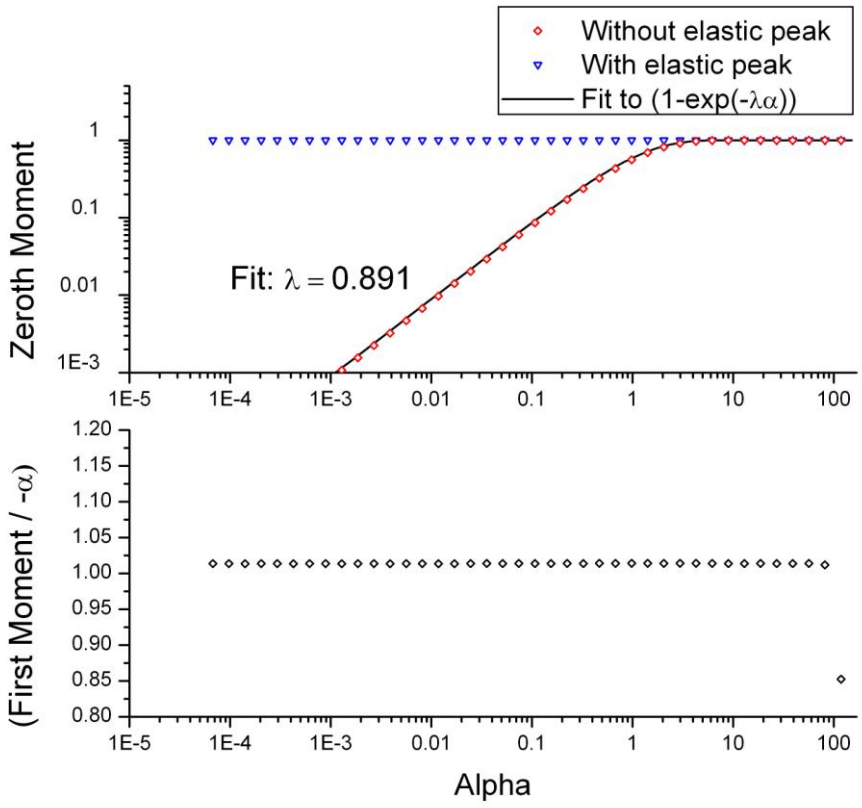

Fig. 4-21. Computed moments of the MD scattering law. The first-order moment has been normalized by its theoretical value.

4.4.5 Relaxing the Gaussian Approximation

With the MD scattering law and cross section validated against *ab-initio* / NJOY calculations, the Gaussian approximation may now be relaxed with confidence. This entails evaluating the intermediate function directly as:

$$I^{cl}\left(\vec{\kappa},\tau\right)=\frac{1}{NL\left(\tau\right)}\sum_{k=1}^{L(\tau)}\sum_{j,j'}\exp\left[-i\vec{\kappa}\cdot\vec{R}_{j'}\left(t_k\right)\right]\exp\left[i\vec{\kappa}\cdot\vec{R}_{j}\left(t_k+\tau\right)\right] \qquad (4.36)$$

without reducing it to a function of the mean-squared displacement alone. Since the variable κ retains its vector status in this situation, the intermediate function is determined by

averaging over those vectors κ having the same modulus $|\kappa|$, where the input κ vectors are randomly generated.

Using a set of 100 random κ vectors for each shell of $|\kappa|$, the incoherent cross section was computed again using the classical-to-quantum conversion routine discussed in section 4.5.4. The total cross sections, shown in Fig. 4-22, change little under the removal of the Gaussian approximation, thus revealing that the Gaussian approximation is generally accurate for graphite. The differential spectra, displayed in Fig. 4-23, are impacted slightly at small values of the energy transfer, although no significant changes are observed in the shape of the secondary distributions.

While the impact of the Gaussian approximation on the differential and total cross section appears minimal, it should be noted that these are integral quantities; information of greater fundamentality is obtainable from a direct comparison of $I_s(\kappa,t)$. To this end, the time-averaged fractional deviation of the Gaussian-approximated $I_s(\kappa,t)$ function relative to the κ-sampled $I_s(\kappa,t)$ function, given by:

$$R_G(\kappa) = \left\langle \left| \frac{I_s^G(\kappa,t) - I_s(\kappa,t)}{I_s(\kappa,t)} \right| \right\rangle_t \tag{4.37}$$

is plotted in Fig. 4-24. An R_G value of zero indicates that the functions are identical on the investigated domain.

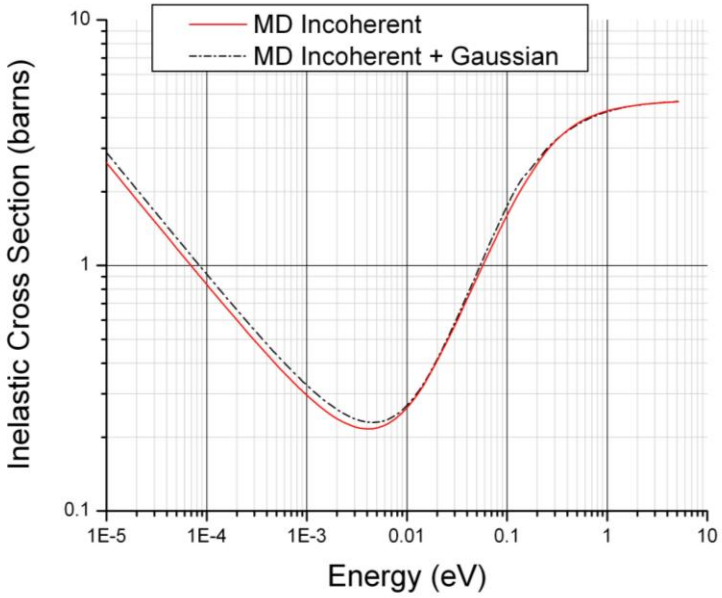

Fig. 4-22. Incoherent inelastic scattering cross section at 300 K, with and without the Gaussian approximation

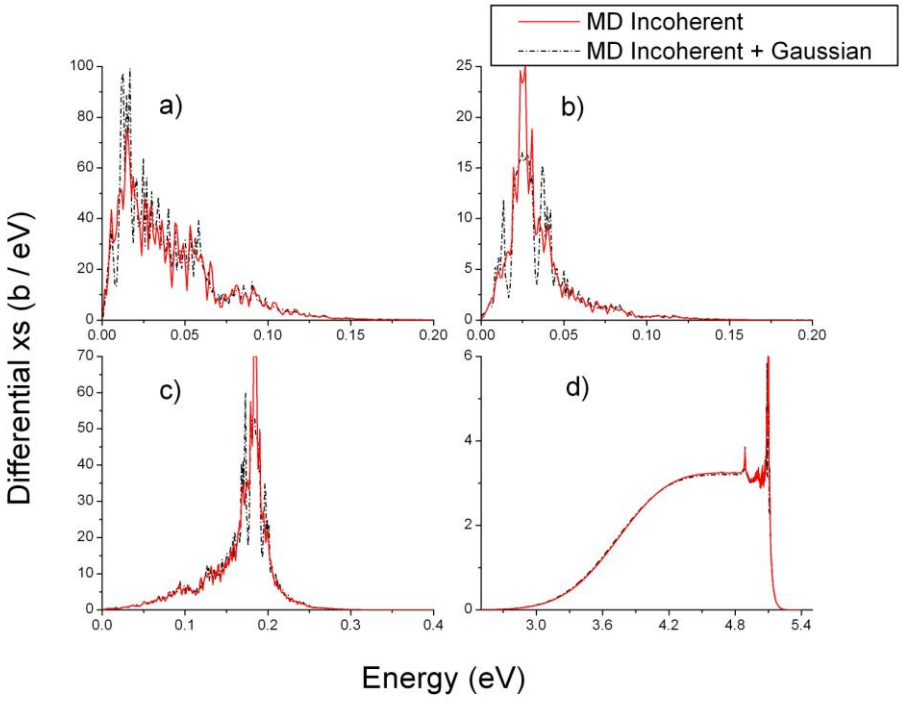

Fig. 4-23. Incoherent inelastic cross section at 300 K, with and without the Gaussian approximation, at a) 1E-5 eV, b) 0.0253 eV, c) 0.184 eV and d) 5.1 eV.

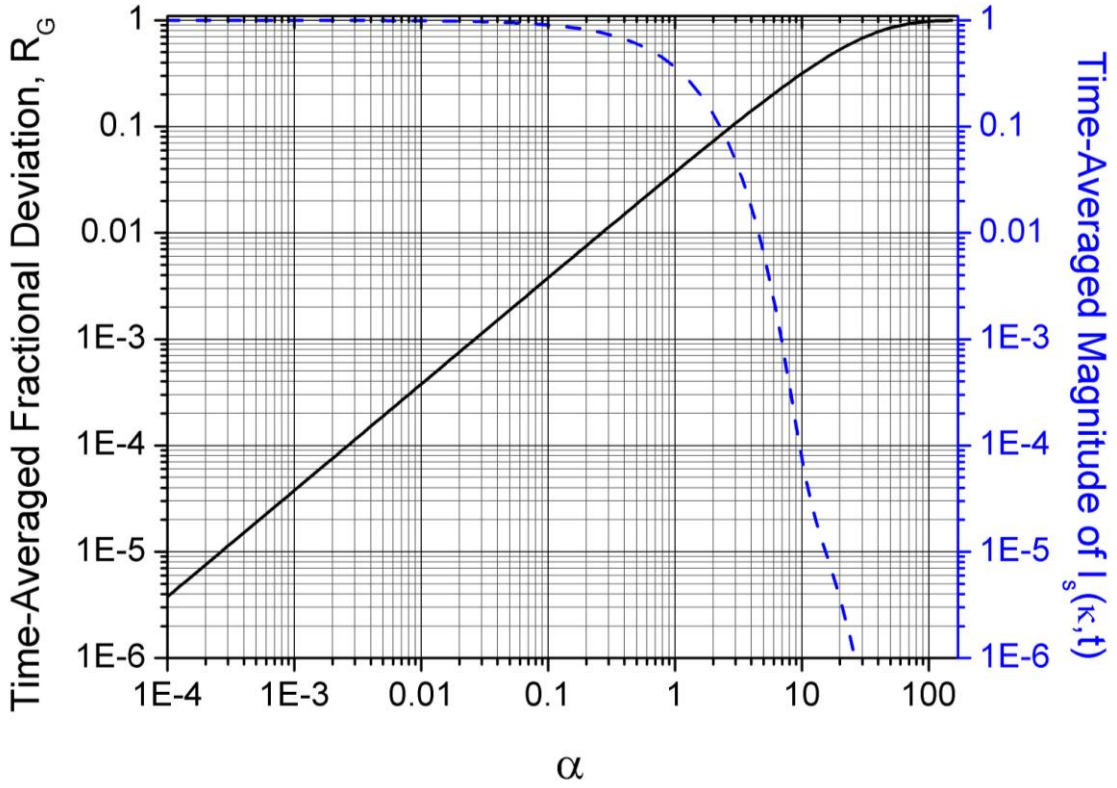

Fig. 4-24. Time-averaged deviation factor R_G (see Eq. (4.37)) as a function of α. Also shown is the time-average magnitude of the real part of $I_s(\kappa,t)$.

In Fig. 4-24, the deviation factor, R_G, increases monotonically with α, reaching a value of 4% at α = 1 and 10% at α = 3. Because the cross section is more sensitive to the low-α behavior of the scattering function, and also because the magnitude of $I_s(\kappa,t)$ dies out rapidly with increasing α, the deviation at high α has negligible effect on the cross section. Reasons for the large deviation at high α are at least partly numerical; for example, the decay of the Gaussian-approximated $I_s(\kappa,t)$ is governed by an analytic relation, whereas the decay of the κ-sampled $I_s(\kappa,t)$ follows from the numerical averaging of the particle density operator product of Eq. (4.36). It is not surprising, therefore, that the two formulae give somewhat

different results at high α where $I_s(\kappa,t)$ lies many orders of magnitude below unity (except at extremely short times).

4.4.6 Effect of Temperature

The impact of temperature on the cross section is determinable simply by raising the temperature of the MD system. Resultant changes in the time-dependent atomic positions are then reflected in the scattering law through the Fourier transform relations.

The high- temperature limit of the cross section is well known: as interatomic binding effects becomes less and less important, the system approaches the "free gas" limit in which no crystalline atomic structure exists. In this limit, the cross section is essentially the free atom cross section everywhere, modified by a 1/v tail at low energies. At intermediate temperatures, one would expect the cross section to increase with temperature due to the higher occupancy of phonon states, which in turn provides more opportunity for energy exchange between the impinging neutron and the crystal.

The effect of temperature on the scattering law and total cross section is shown in Fig. 4-25 and Fig. 4-26 respectively. Associated differential cross sections are given in Fig. 4-27. Agreement is excellent between the *ab-initio* / NJOY and MD cross sections, both of which approach the free gas limit at high temperatures, as expected. In the limit of high incident energies, temperature has negligible effect because the thermal vibrations of the nuclei will be insignificant with respect to the motion of the neutron.

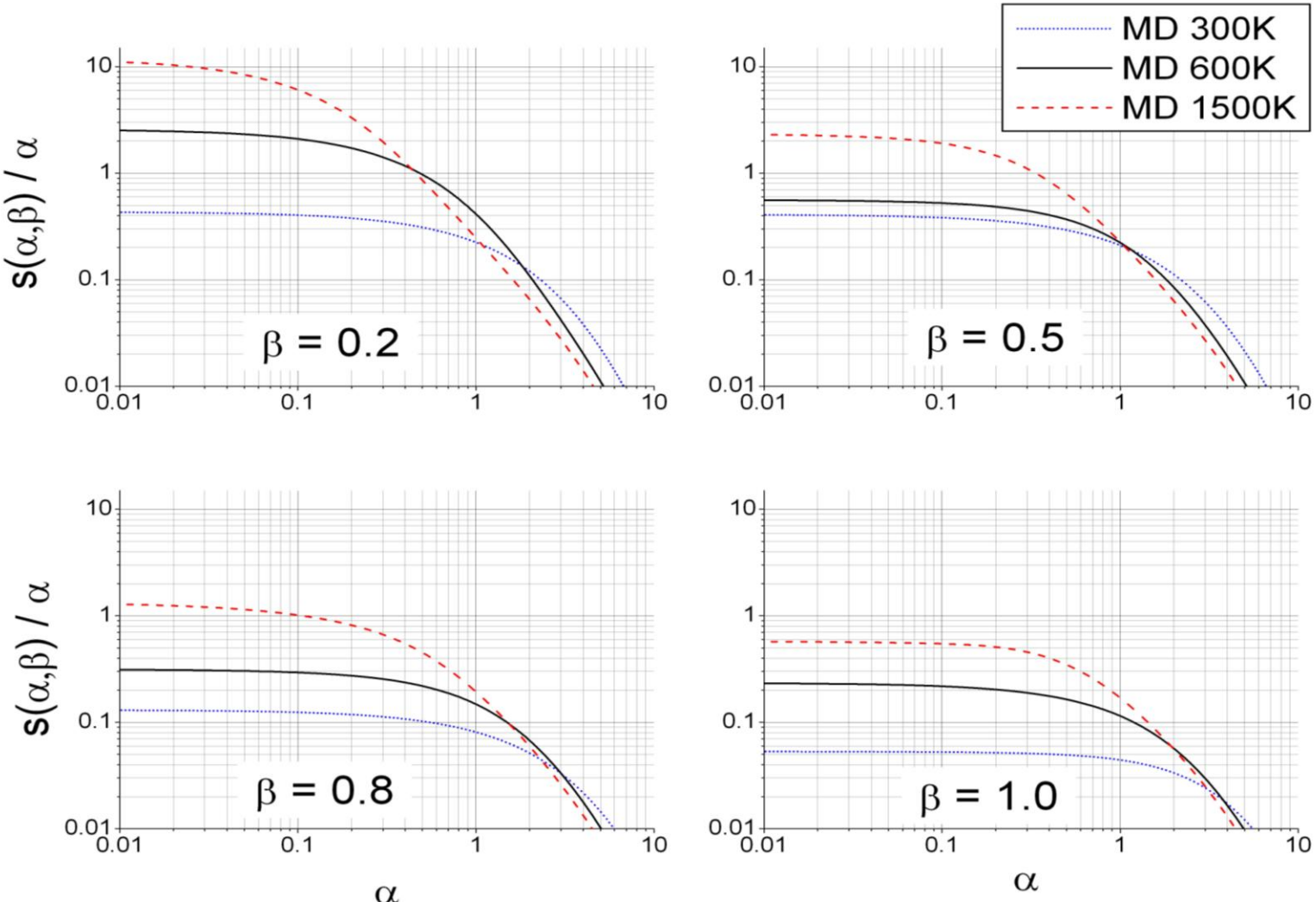

Fig. 4-25. Temperature dependence of the MD incoherent inelastic scattering law.

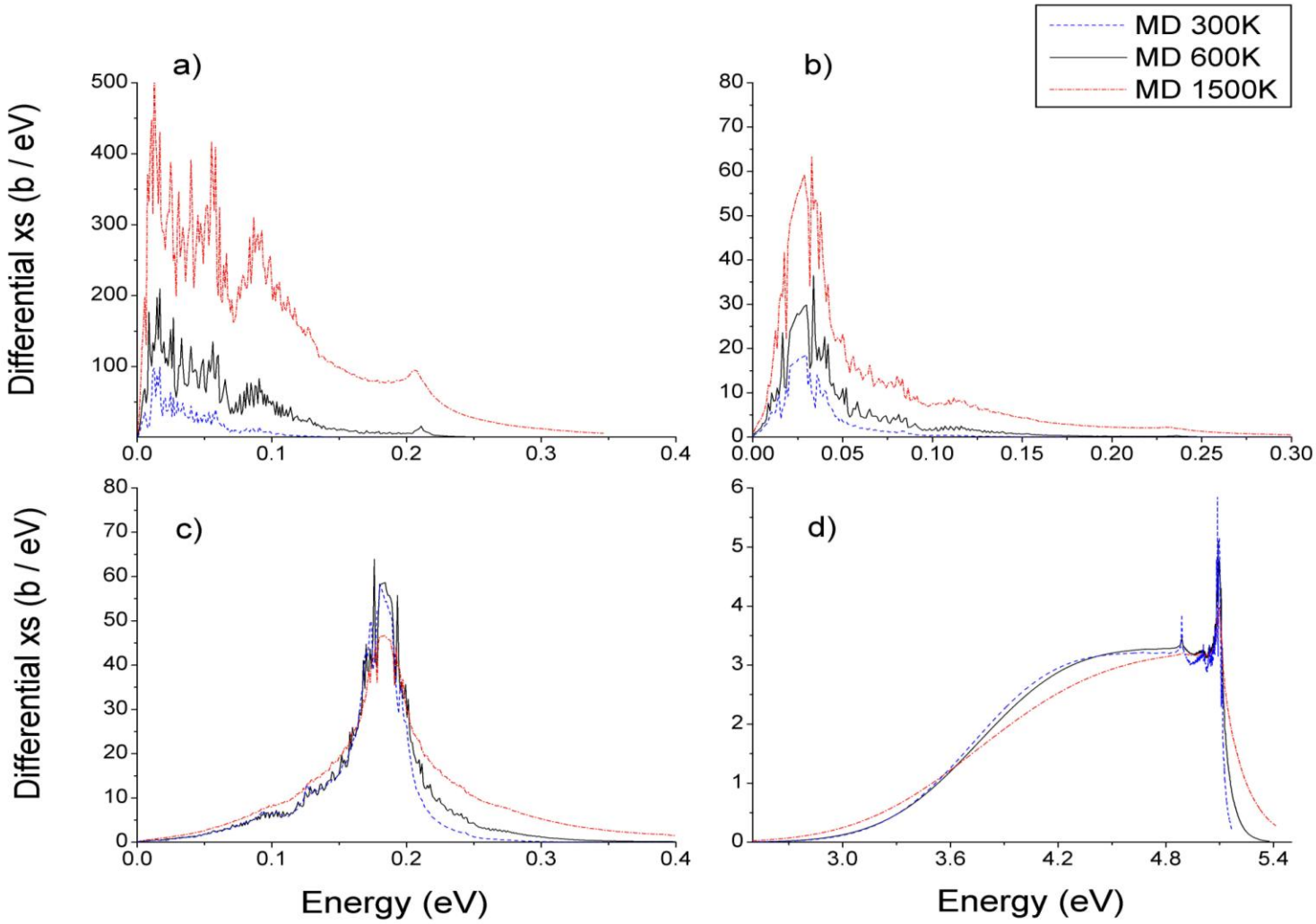

Fig. 4-26. Temperature dependence of the MD incoherent inelastic differential cross section at a) 1E-5 eV, b) 0.0253 eV, c) 0.184 eV and d) 5.1 eV.

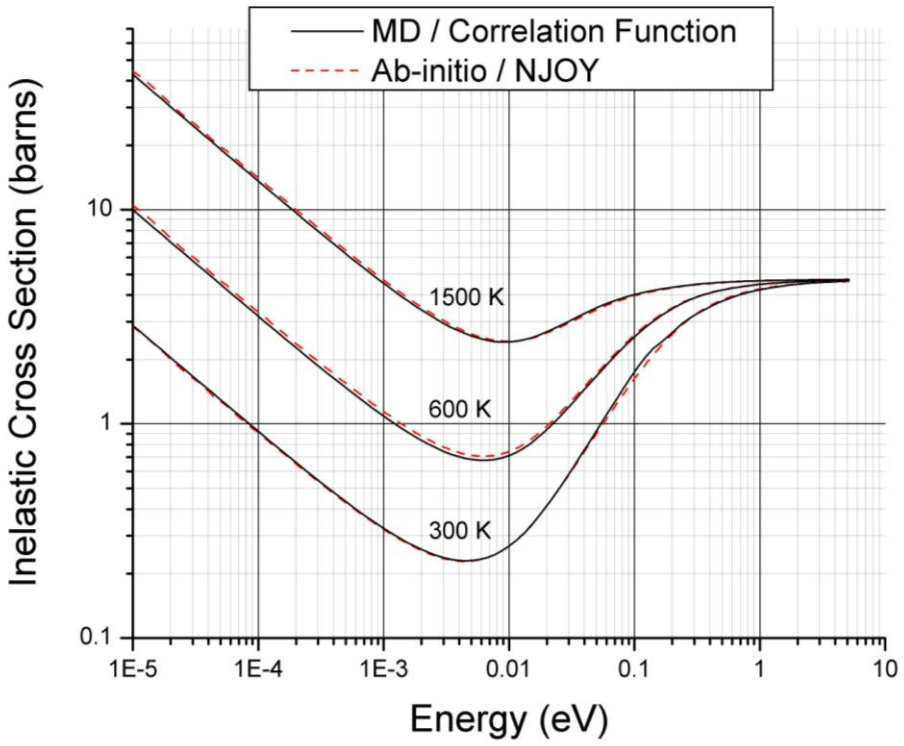

Fig. 4-27. Effect of temperature on the total inelastic incoherent cross section.

Two conclusions are readily drawn from the temperature dependence of the differential cross sections of Fig. 4-27. First, at low incident energies, the upscattering cross section (i.e. the region where $E' > E_{inc}$) increases in magnitude rapidly with temperature. Phonon absorption is the dominant mechanism of energy transfer at small E_{inc}, and so the cross section is highly sensitive to the phonon population (occupancy) of the lattice, which varies with temperature as per the Planck distribution. Second, there is a tendency for the differential distribution to become more symmetric about E_{inc} at higher temperature – a trend most apparent in panels c) and d). This is consistent with the earlier discussion of the classical cross section, for which parity was attained between positive and negative energy transfers due to the fact

that $S^{cl}(\alpha,\beta) = S^{cl}(\alpha,-\beta)$. Since the classical scattering law can be posited as the high temperature limit of $S(\alpha,\beta)$, the symmetry about E_{inc} at high temperatures follows from the diminished impact of quantum effects.

4.5 Coherent Scattering

Recoil (in the conventional sense) does not play a role in distinct scattering, and quantum effects are, on the whole, considerably less important in $S_d(\kappa,\omega)$ because energy and momentum transfers are generally much lower than in $S_s(\kappa,\omega)$. Similar conclusions have been drawn by Wick [71]. Detailed balance still holds for $S_d(\kappa,\omega)$, however, and the harmonic correction factor is therefore retained in the distinct formulation. As was shown in Fig. 3-8, the multiplicative correction factors for detailed balance all converge to unity at $\beta = 0$ but modulate the scattering law greatly at large values of β. Thus, the influence of the harmonic factor on the distinct scattering law is expected to be small due to the shorter effective range of β.

The spatial dimensions of the supercell are an immediate concern in evaluating $S_d(\kappa,\omega)$ since the supercell dimensions determine the range of interatomic distances over which $S_d(\kappa,\omega)$ is computed. From the Gaussian form of the coherent intermediate function (Eq. (3.71)), it is apparent that $I_d(\kappa,t)$ very quickly dies out as either κ or Δr increases. Noting that the number of candidate atomic pairs increases approximately in proportion to r^2 from a reference atom, one can show that a range of a few tens of angstroms is sufficient for ascertaining $S_d(\kappa,\omega)$.

For the present work, calculations were performed using a 9600 atom supercell. Computational cost was further reduced (and edge effects avoided) by selecting only the centermost 20 atoms as *j* atoms, with the *j'* index running over all 9600 atoms in the system. The atomic positions were recorded for 131,072 steps (65.5 ps) after the equilibration period, as in the incoherent case.

For a 9600 atom system (with the *j* index running over the central 20 atoms), a total of:

$$N_{pair} \;=\; N_j\left(N - N_j\right) + \frac{\left(N_j^2 - N_j\right)}{2} \;=\; 191790 \tag{4.38}$$

atomic pairs would have to be considered. The cost of the calculation is reduced considerably by invoking the coherent Gaussian approximation beyond a certain cutoff radius, which is justifiable in the case that correlated motion is negligible beyond that distance. This is generally a good approximation outside of the close neighbor shells. The intermediate function is therefore calculated as:

$$I_{j,j'}\left(\kappa,t\right) = \begin{cases} \left\langle \exp\left(-i\vec{\kappa}\cdot\vec{r}_j\left(0\right)\right)\cdot\exp\left(i\vec{\kappa}\cdot\vec{r}_{j'}\left(t\right)\right)\right\rangle & \textit{if} \quad R < R_{cut} \\ \exp\left[\dfrac{-\kappa^2}{6}\left\langle\left(r_j\left(t\right) - r_{j'}\left(0\right)\right)^2\right\rangle\right] & \textit{if} \quad R > R_{cut} \end{cases} \tag{4.39}$$

where $R = \left|\vec{r}_j - \vec{r}_{j'}\right|$. In all other respects, the computation of $S_d(\kappa,\omega)$ and derived quantities is identical to the incoherent case.

The room temperature MD total inelastic scattering cross section is plotted in Fig. 4-28, and the associated distinct distributions are shown in Fig. 4-29. Here, the *ab-initio* + 1-phonon

curve refers to the sum of the *ab-initio* / NJOY incoherent cross section and the exact distinct 1-phonon cross section. An R_{cut} value of 3.7Å was selected in order to ensure that correlations in the first few coordination shells were evaluated exactly. It is interesting to note that if the coherent Gaussian approximation is utilized everywhere (i.e. if $R_{cut} = 0$), then the differential spectra are guaranteed to be positive over the entire domain. Hence, negative values in the distinct scatter law or differential spectra are a consequence of the close neighbor correlations. Good agreement is observed against measured data for the total scattering cross section, and the differential cross sections from MD also match the *ab-initio* based 1-phonon differentials reasonably well. Limited experimental data for S(α,β) at 300 K is available from Wikner [72]; this is plotted alongside the total S(α,β) from MD in Fig. 4-30.

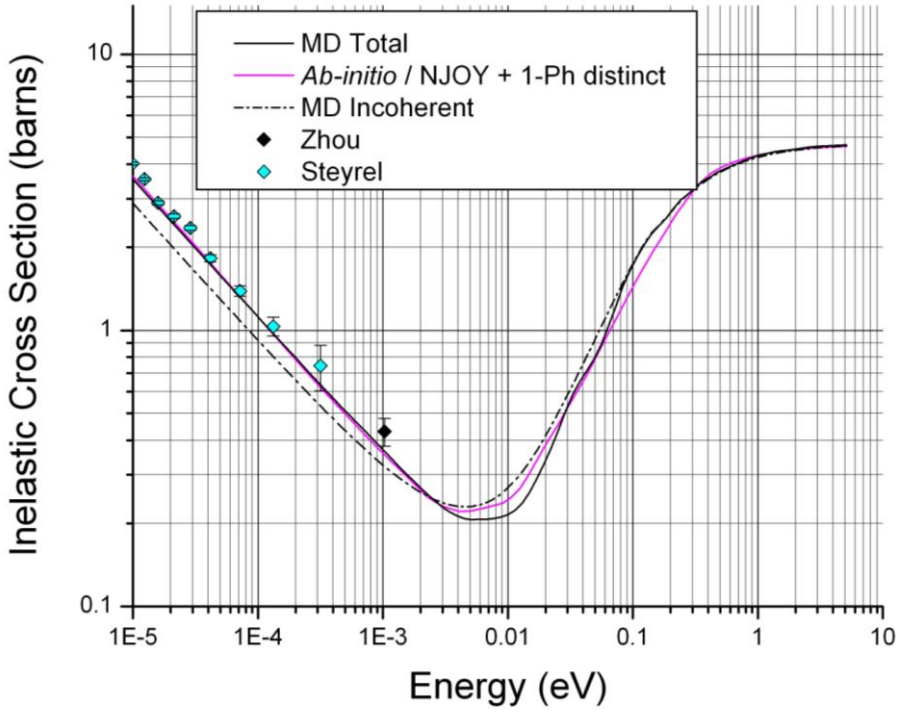

Fig. 4-28. Total inelastic cross section of graphite at 300 K. The experimental measurements of Steyrel [16] and Zhou [19] are shown as diamonds.

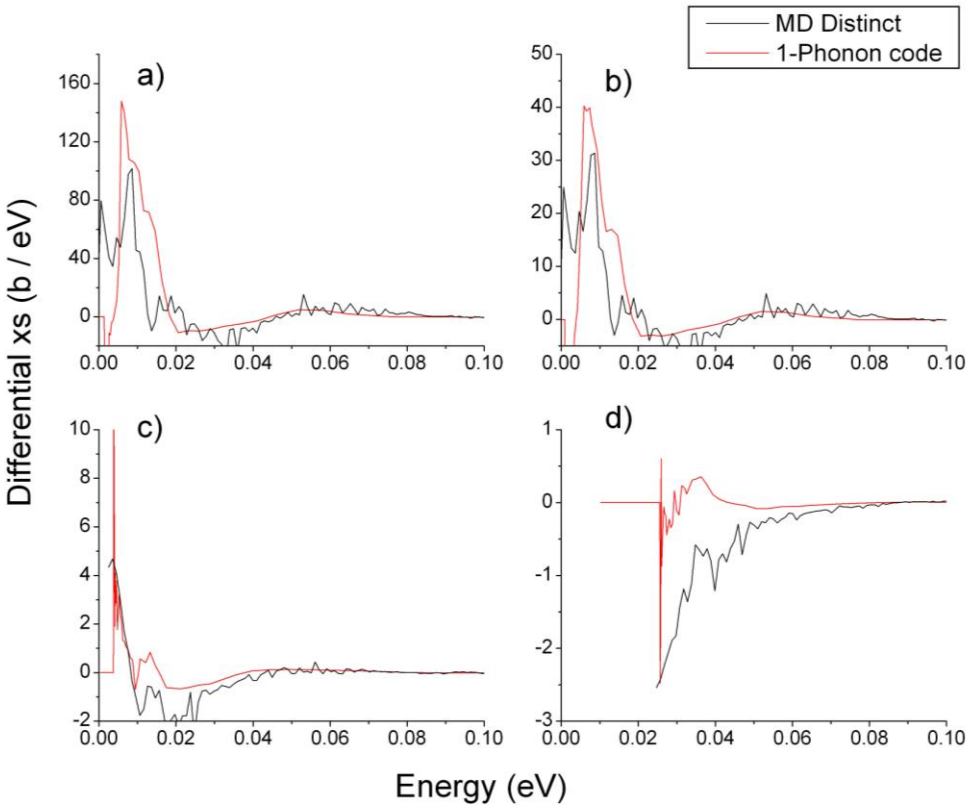

Fig. 4-29. Distinct differential cross section at a) 1E-5 eV, b) 1E-4 eV, c) 3E-3 eV and d) 0.025 eV.

An excellent benchmark of the MD coherent calculation is the set of experimental scattering law data published by Carvalho [73] for 533 K graphite. Carvalho's data, complete with uncertainty estimates, shows clearly the oscillations that $S_d(\alpha,\beta)$ superimposes onto the normally smooth $S_s(\alpha,\beta)$. By integrating $S(\alpha,\beta)$ to obtain the cross section, these oscillations are largely dampened or removed from the final product, and so the original $S(\alpha,\beta)$ distribution is a superior indicator of the underlying system dynamics. Fig. 4-31 demonstrates that oscillations in the MD $S(\alpha,\beta)$ are overwhelming in-phase with those of the 1-phonon distinct curve, and, furthermore, that the MD scattering law exhibits similar agreement with experimental measurements.

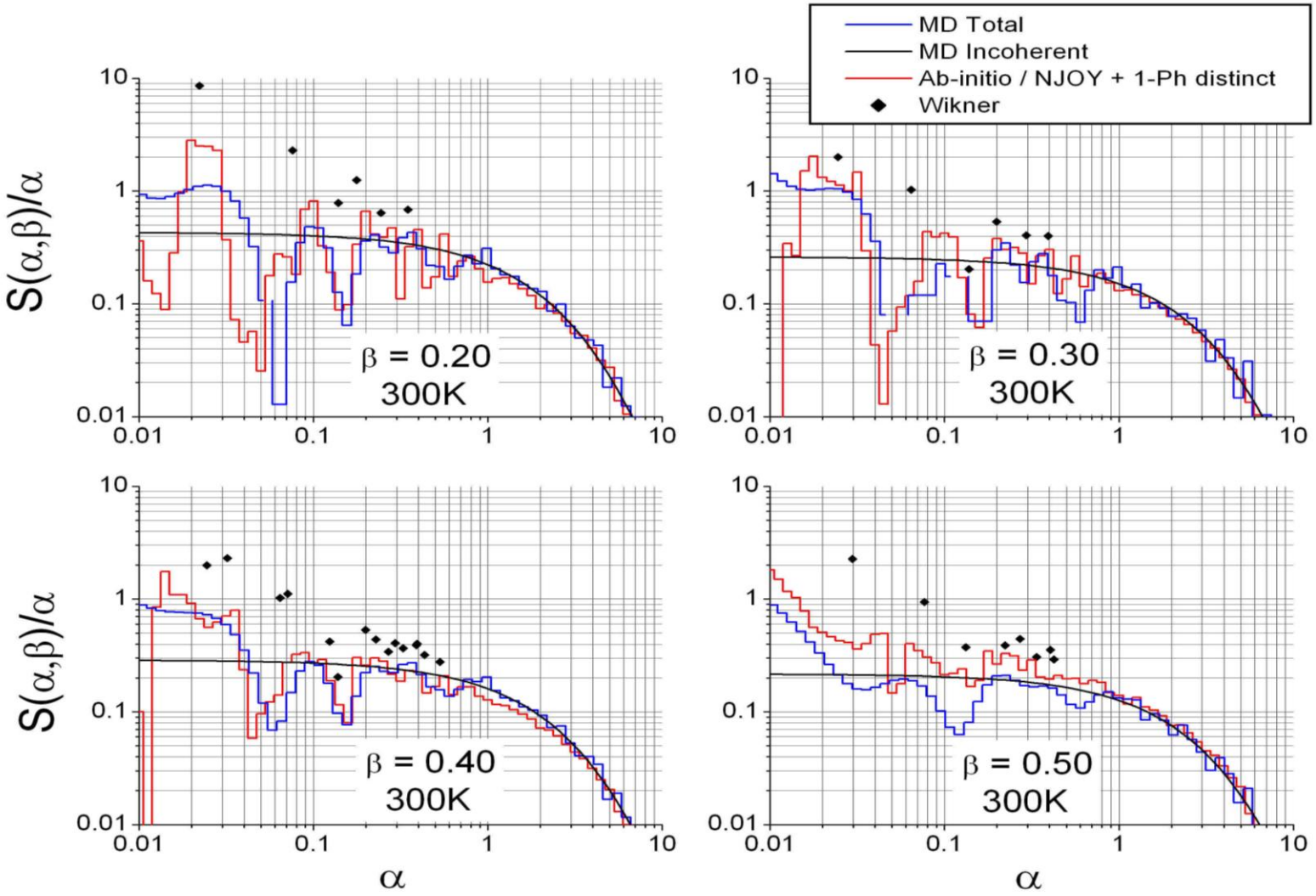

Fig. 4-30. Total scattering law of graphite at 300 K, including coherent effects.

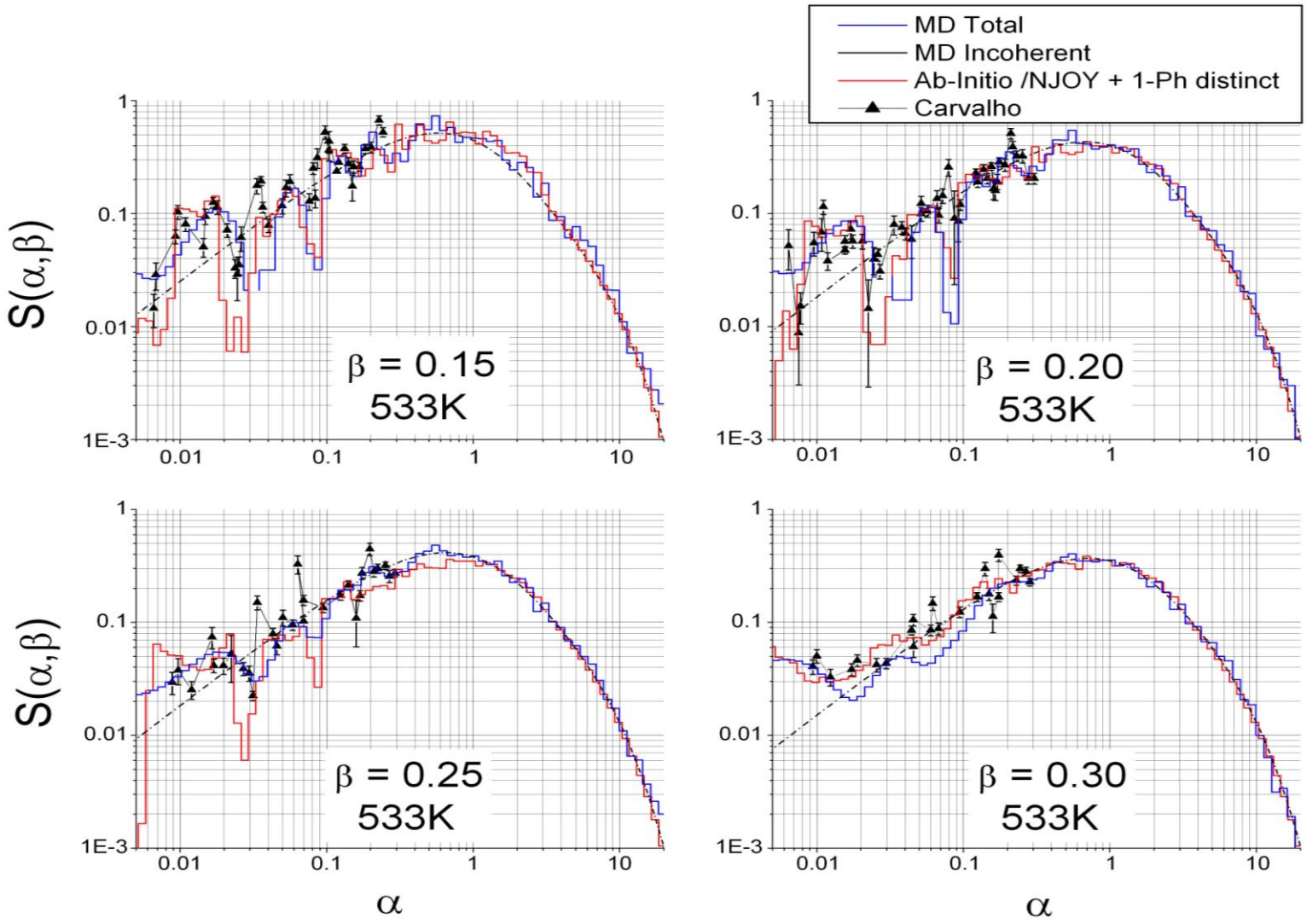

Fig. 4-31. Total scattering law of graphite at 533 K, including coherent effects.

Chapter 5

Results for Damaged Graphite

5.1 Introduction

Materials exposed to neutron irradiation (e.g. in a reactor environment) will experience defect accumulation as a consequence of neutron interactions with the constituent nuclei. For a moderator material, such damage arises overwhelmingly from fast, fission-born neutrons that slow down due to a series of collisions with the atoms comprising the moderator. Very often, the energy imparted by the neutron is far in excess of the site energy of the atom, in which case the atom is dislodged and instigates a cascade of defects. Over time, the defects created in this manner can interact to generate intricate formations. And while it is well known that the presence of defects can cause drastic changes in properties such as thermal and electrical conductivity, recent work with *ab-initio* simulations [21] suggests that irradiation-induced defects influence the thermal scattering cross section as well.

Simulating radiation damage with MD is, in principle, a fairly simple matter. The neutron need not be introduced explicitly into the simulation – only the kinetic energy transferred to the primary knock-on atom (PKA) is of practical import. Once the kinetic energy is imparted, the damage evolution process proceeds naturally until a new, quasi-stable state is reached (generally coinciding with the dissipation of the temperature spike). Atoms may continue to

migrate through defect hopping, but the characteristic timescale of defect migration largely falls outside the standard timescale of MD simulation.

5.2 Defect Formations

A damaged sample of graphite can contain a number of distinctive defect formations, some of which originate from the migration and consolidation of simple point defects. The most basic defect is the *Frenkel pair* – essentially a vacancy / interstitial pair. Frenkel defects exist naturally at concentrations dependent upon temperature via an Arrhenius-type relation, and their number is augmented by irradiation. Graphite interstitials preferentially congregate in the interlayer gaps, where there is abundant open space to accommodate them.

These interstitials, as well as the vacancies left in their wake, can coalesce into more complex structures such as the interstitial and vacancy loops shown schematically in Fig. 5-1. The migration energy for interstitials is relatively low between planes, and so, in the absence of recombination sites, diffusing interstitials will tend to congregate together in a more energetically favorable configuration resembling a new graphitic layer. A vacancy loop, on the other hand, causes the inward collapse of nearby layers due to local distortions in the Van der Waals forces.

On a typical MD timescale that is too short for significant diffusional restructuring to occur, radiation-damaged regions of graphite can be divided broadly into one of two categories:

- ***Lightly damaged regions***, dominated by simple vacancy and interstitial defects that are embedded within a well-defined graphitic layered structure
- ***Heavily damaged regions***, in which the graphitic structure has been disrupted to the point of amorphization, and discrete layers are no longer discernable

This distinction shall be further clarified through visualization of the products of MD collision cascades.

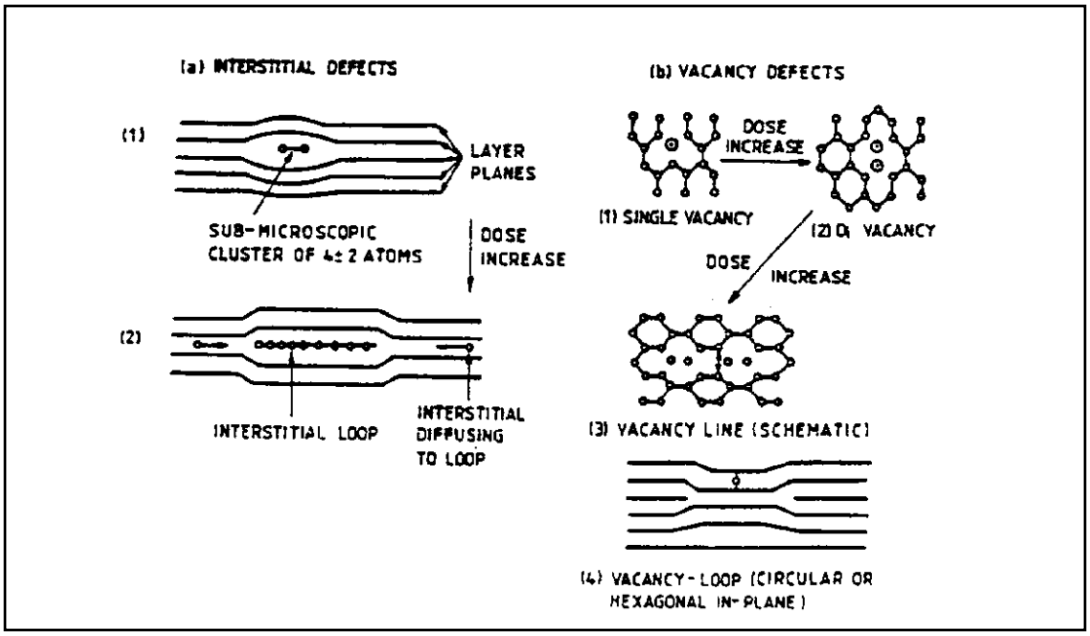

Fig. 5-1. Accepted model of defect aggregations in graphite [74].

In the present work, the following computational procedure was employed to simulate cascade defect production:

1. The system is relaxed at a set temperature, which is controlled using a thermal bath.
2. A PKA is selected at random from atoms outside of the bath. The velocity vector of the PKA is directed towards the center of the system in order to minimize energetic collisions within the thermal bath while still precluding directional bias.

3. A “cool down” period follows the cascade, allowing for prompt migration and/or recombination to take place.
4. Steps 2-3 are repeated until the desired degree of damage is reached.

5.2.1 Simple Vacancy and Interstitial Defects

Interplanar interstitials tend to be the most obviously observable defects in lightly damaged systems. As an example, the steady-state structure of an MD graphite system following a 1-keV cascade simulation is shown in Fig. 5-2. For the purpose of visualization, MD output was fed into the Visual Molecular Dynamics (VMD) code [75], which is capable of displaying and animating time-dependent atomic configurations. This required a simple conversion to the XYZ format – a minimalist file structure containing the coordinates of each atom at each time step. If desired, additional information such as the site energy or net force can also be appended to enable a visual interpretation of the interatomic interactions.

As expected, a number of interstitials are seen to have settled between the graphitic basal planes, including one di-interstitial that is clearly discernable near the top of the figure.

In addition to the generic interplanar interstitial, several other specific defect forms are known to exist in graphite. A typical vacancy formation is the Stone-Wales defect [76], distinguishable by the coexistence of pentagonal and heptagonal rings in close proximity. Numerous examples of this defect were observed in regions of the graphite MD supercell that were significantly impacted by cascade sequences; a close-up view of one such defect is shown in Fig. 5-3. The same imperfection is displayed in Fig. 5-4 in the context of a

damaged graphite layer. For purposes of comparison, a reference schematic of basal plane vacancy clusters is displayed in Fig. 5-5.

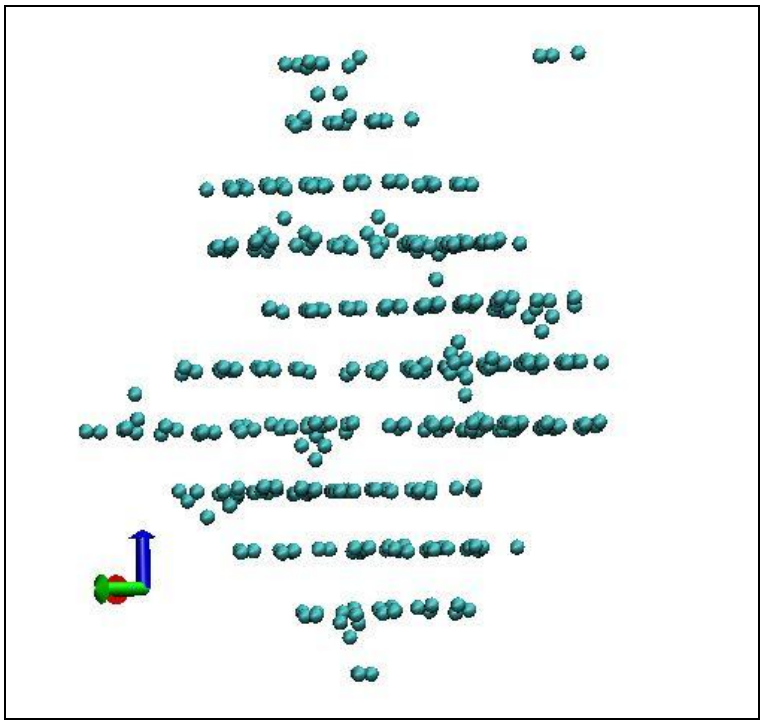

Fig. 5-2. Steady-state structure of graphite following a 1 keV cascade. Only those atoms significantly affected by the cascade are included; the supercell itself extends far beyond the displayed region.

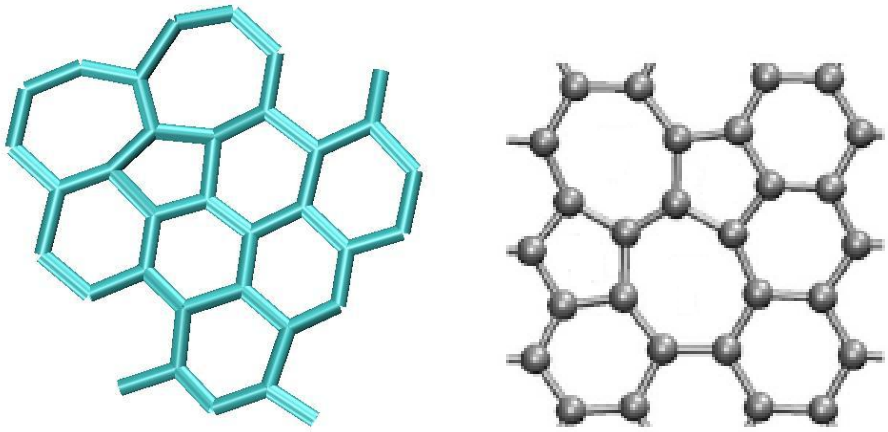

Fig. 5-3. Close-up view of a Stone-Wales defect from MD (left) and from *ab-intio* [76] (right).

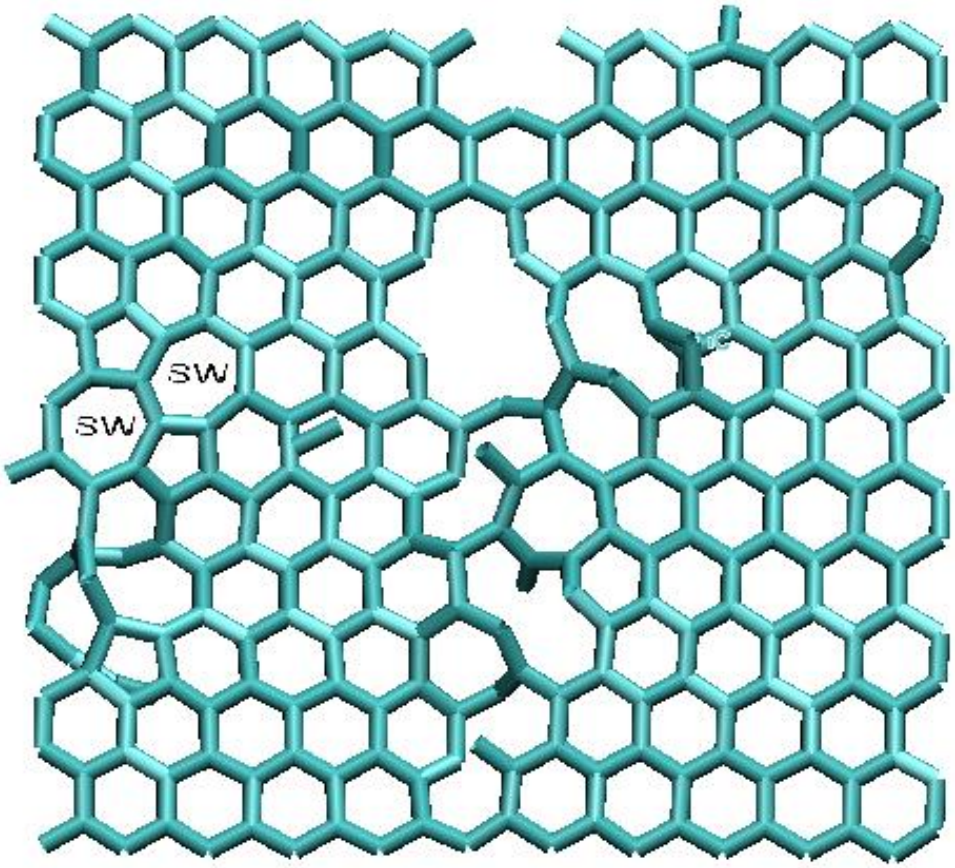

Fig. 5-4. Stone-Wales defect in the context of a damaged basal plane. The heptagonal rings are marked with an "SW".

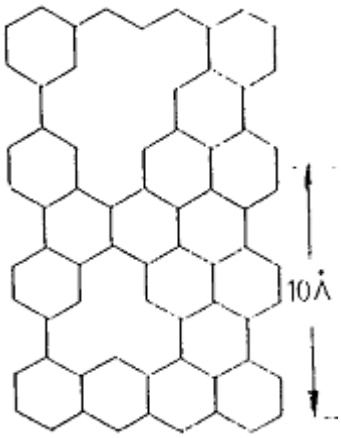

Fig. 5-5. Defects within the graphite layer, from [77].

The damaged layer of Fig. 5-4 contains single vacancies as well as a cluster of multiple adjoined vacancies. Occasional pentagonal or heptagonal rings are also visible apart from those comprising the Stone-Wales defect. At higher temperatures and sufficiently long times, diffusional processes becomes a significant factor in enabling the aggregation of vacancy loops from individual defects. Calculations in the present work typically span tens or hundreds of picoseconds, which is insufficient to witness considerable defect diffusion.

Another defect that has been identified through atomistic simulation is the cross-planar divacancy defect, which generates a "dumbbell" type bond between the planes.

A comparison of the MD formation with one generated from *ab-initio* structure optimization [78] is shown in Fig. 5-6, and a top view of the same MD defect is given in Fig. 5-7. In this particular MD formation, the dumbbell axis lies at a 45˚ angle to the crystallographic c-axis and oscillates about a mean length of 1.55 Å – somewhat longer than the corresponding *ab-initio* defect, which forms a lesser angle with the c-axis. Such a relationship between angle and distance is to be expected, since the bridging distance increases with angle.

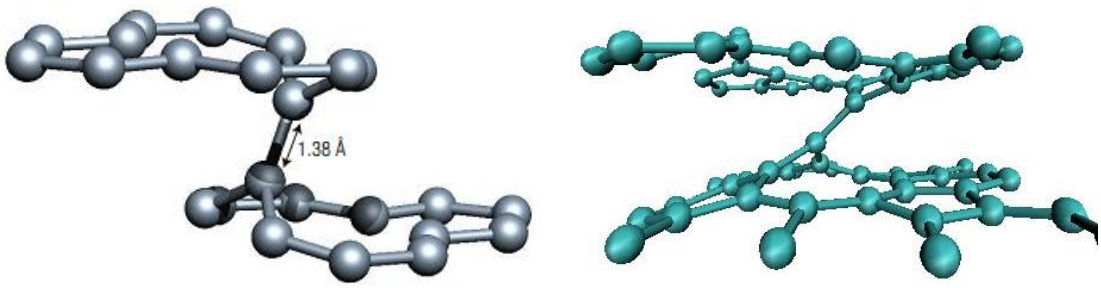

Fig. 5-6. Interplanar divacancy defect: from *ab-initio* simulation [78] (left) and from MD simulation (right).

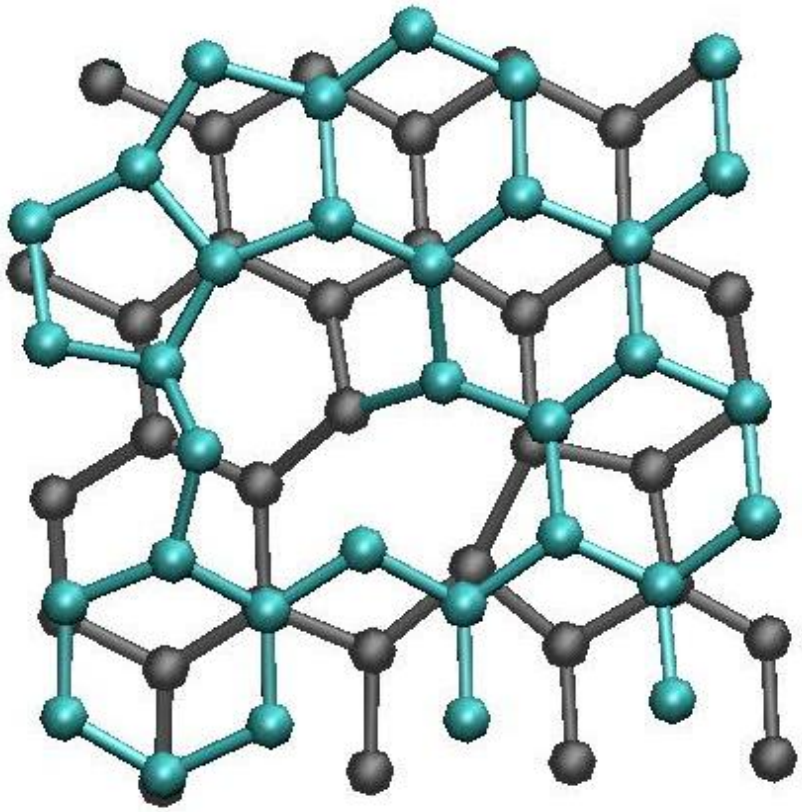

Fig. 5-7. Top view of the MD interplanar divacancy defect. Atoms colored in cyan form the top layer while atoms colored in grey comprise the bottom layer. The divacancy defect is evident near the center of the image. Other imperfections are also present such as the pentagonal rings in the top-left corner.

5.2.2 Heavily Damaged Systems

In regions of heavy damage that have, for instance, experienced the passage of multiple cascades, the ordered carbon layers of graphite exhibit amorphization and the simple defects described in the previous section become less distinguishable as the material structure itself undergoes fundamental changes. Taken to the limit of extremely heavy damage (i.e. an infinite number of cascades) and in the absence of annealing, one would anticipate the

transition to an isotropic, amorphous structure. Physical properties that are sensitive to the details of atomic binding would correspondingly reflect these structural alterations.

Of immediate interest is the effect of extensive damage on the MD graphite system. An example of the long-term accumulation of defects is shown in Fig. 5-8, which illustrates the state of a 9216 atom supercell following a series of 25 1-keV cascades. As the level of damage increases, isolated vacancies and interstitials no longer dominate the defect network, and fully-developed interplanar cross-linking becomes evident.

Indeed, individual planes lose their identity in certain regions of the cell, especially towards the center where most of the damage is concentrated. The cross-linking effect is displayed more clearly in the close-up view of Fig. 5-9, showing one subregion of the damaged structure. The associated rearrangement of atoms within the basal plane is illustrated in Fig. 5-10.

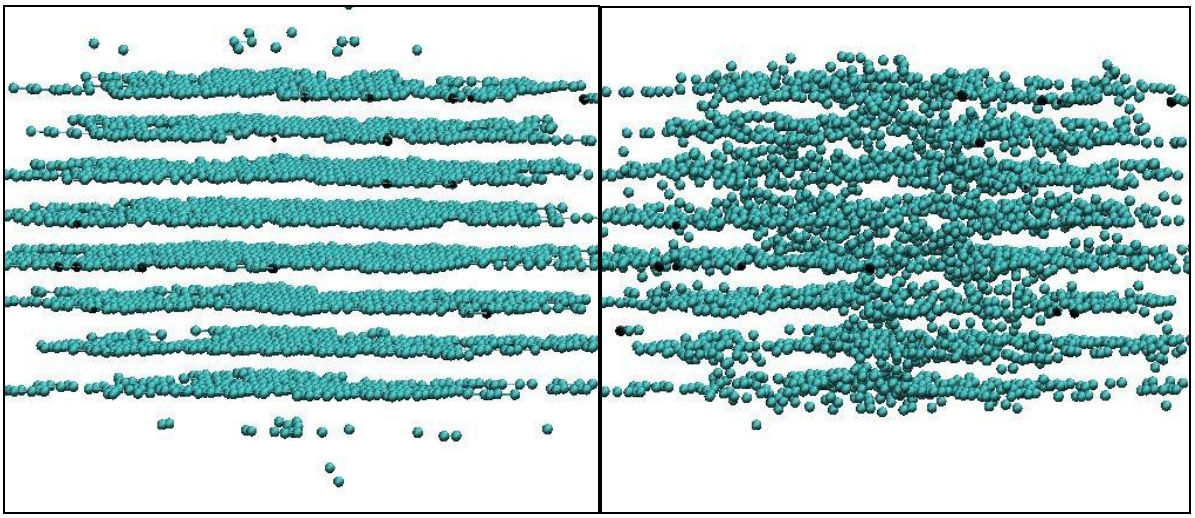

Fig. 5-8. A 24x24x4 graphite system before (left panel) and after (right panel) a series of 25 1-keV cascades initiated at random locations within the cell. Only the most heavily damaged region is shown here.

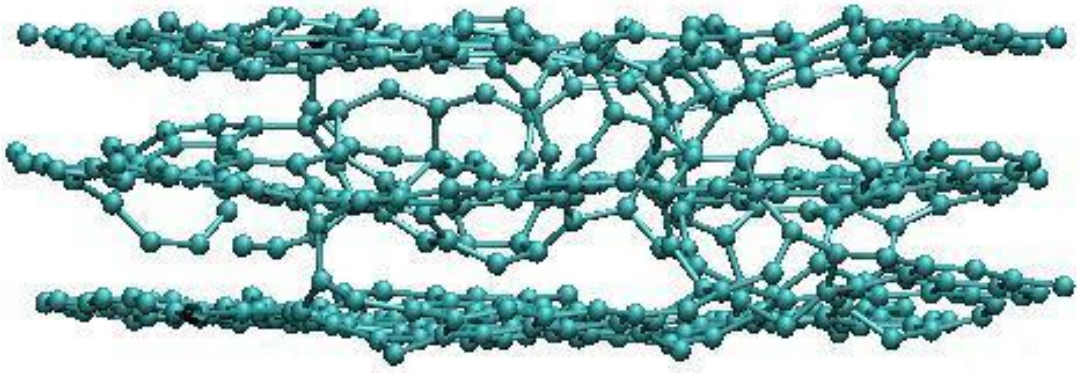

Fig. 5-9. Side view of one segment of a damaged MD graphite system. Extensive crosslinking has occurred between the planes

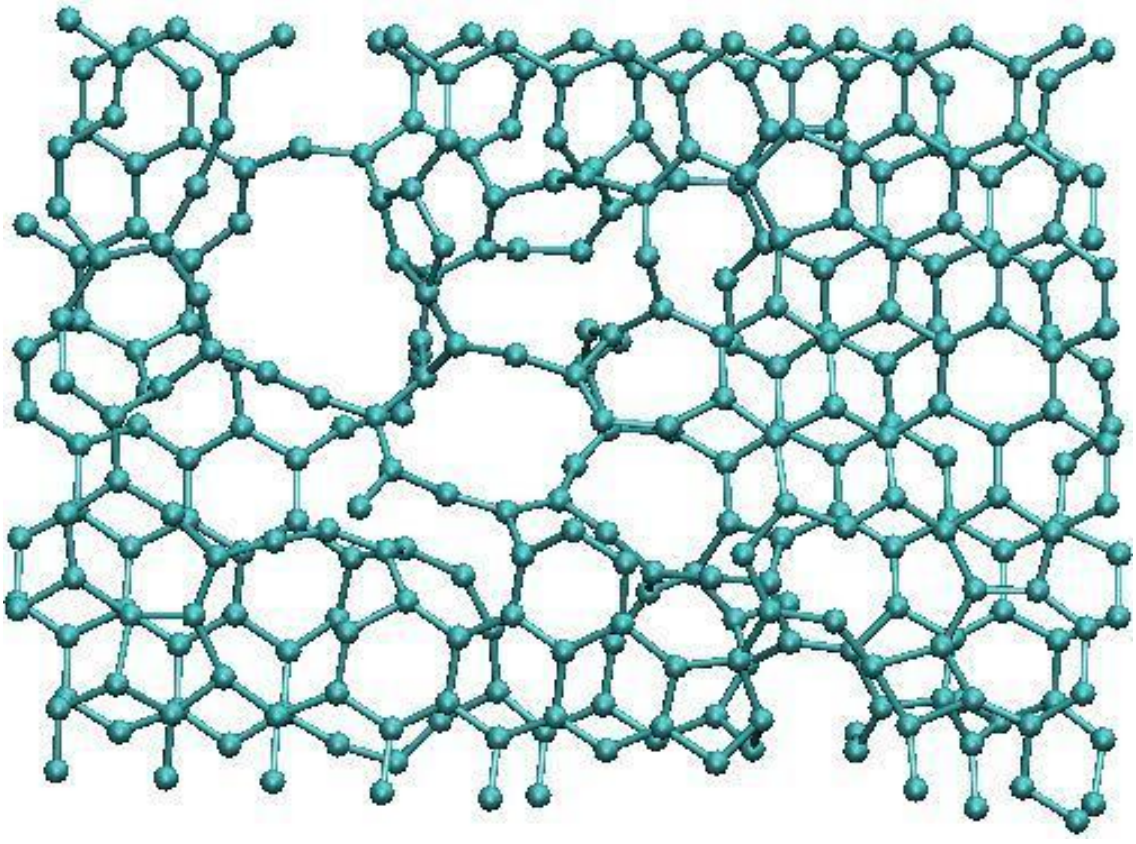

Fig. 5-10. Top view of the damaged segment. A line of vacancies cuts diagonally across the cell, forming a boundary between two continuous regions of the basal plane.

Evident in Fig. 5-10 is the development of a fissure (vacancy line) separating two distinct segments of the basal plane. The location of the fissure coincides with the cross-linked region shown in the adjacent panel. Burchell [79] has described a similar defect in conjunction with irradiation damage to graphite; this defect, displayed in Fig. 5-11, is also characterized by the linking together of two neighbor planes and the related formation of nearby vacancy clusters.

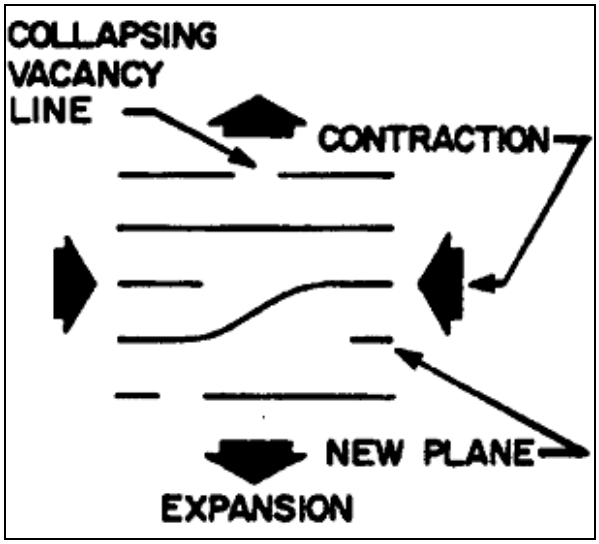

Fig. 5-11. Cross-linking of two planes, with the accompanying formation of vacancy lines (from [79]).

5.3 Stored Energy

As defects build up in the system, the average binding energy per atom will be reduced – in other words, a portion of the energy introduced through cascades is *stored* in the supercell. Any disruption to the minimum-energy structure will, by definition, increase the system potential energy. By the same token, defect annealing returns the system to lower-energy state, thereby transforming the stored energy into kinetic energy.

Recognized by E.P. Wigner [80] and investigated by later workers ([81],[82]), the issue of the buildup and release of stored energy has long been a concern in graphite-moderated reactors due to the possibility of a runaway temperature transient. While the stored energy is measurable indirectly using calorimetry, it is quite accessible computationally because the potential energy is a fundamental output variable of MD (or *ab-initio*). The quantity of interest is the average change in potential energy (per atom) brought about by defect accumulation, conventionally converted to units such as J/g.

Fig. 5-12 shows the change in the average potential energy of an 8000 atom supercell as randomly-located 1.5 keV cascades are initiated in the system. Each cascade causes a spike the potential energy that is partially dissipated by recombination processes, with the end result that the system settles out in a quasi-stable, higher-energy state. The system is only quasi-stable because, over long periods of time (relative to the standard timescale of MD), diffusional processes will instigate further defect recombination, and the system gradually transitions to a lower-energy state. For the purposes of MD, quasi-stability is usually

achieved shortly after the cascade-induced temperature spike had dissipated. From Fig. 5-12, the thermal spike is observed to quench within a few picoseconds of the cascade event.

In a closed supercell, stored energy does not accumulate linearly with respect to the introduced cascade energy; this is a consequence of the interaction of the cascading atoms with the products of previous cascades. Simply stated, less energy will be stored in a region that is already damaged. This effect, which has been confirmed by experimental studies [83]-[86], is apparent in the MD results of Fig. 5-12 where the incremental change in potential energy decreases (on average) in the later cascades.

The total stored energy is given by the formula:

$$E_s = N\left(E_p - E_p^0\right)$$

where E_p is the final potential energy (per atom), E_p^0 is the initial potential energy and N is the number of atoms in the supercell. For the MD simulation of 15 1.5 keV cascades (Fig. 5-12), E_s was calculated to be 2.68 keV, which is about 12% of the total cascade energy. The remaining 88% represents kinetic energy that was removed by the thermal bath. On an intrinsic basis, this corresponds to a stored energy of 2740 J/g (655 cal/g), which accords well with the value of 600 cal/g cited by Woods [87] as an upper bound in heavily irradiated graphite.

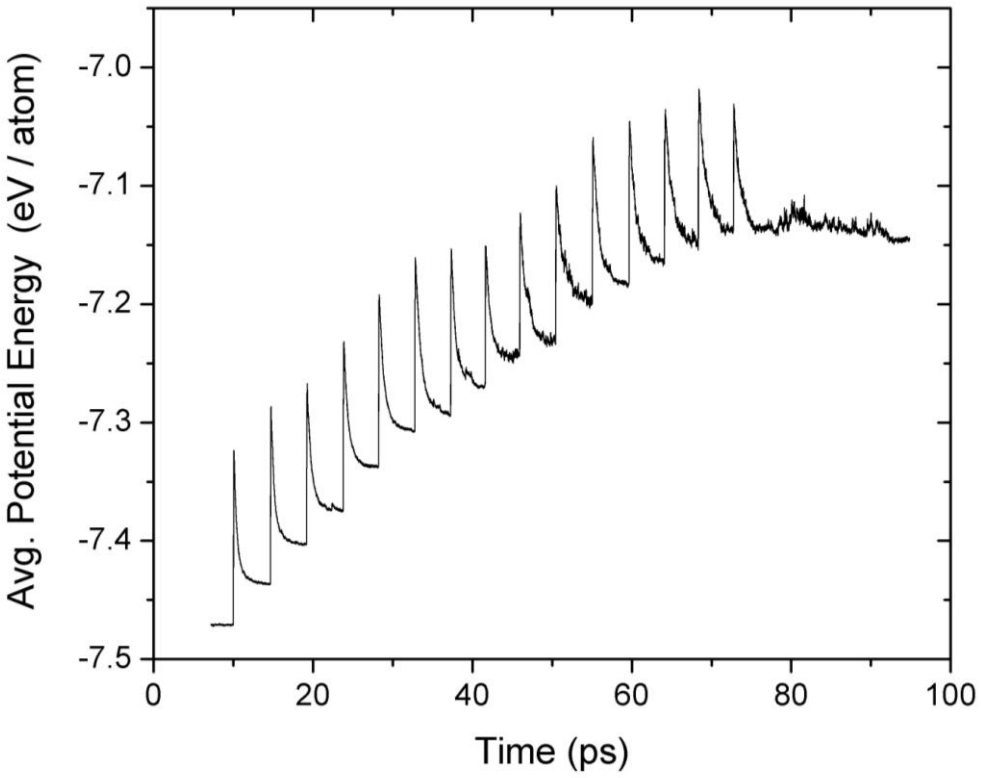

Fig. 5-12. Buildup of stored energy in a 300K MD graphite supercell. Each spike represents a 1.5 keV cascade event.

5.4 Amorphous Carbon

Carbon structures that exhibit no long-ranged order are referred to as *amorphous carbon (a-C).* Disorder is the universal feature of all amorphous carbon; however, many variants of the a-C structure have been identified, and the properties of these variants differ considerably depending on the details of fabrication. As shown in the phase diagram of Fig. 5-13, amorphous carbon is categorized partially on the basis of the sp^2 ("graphite-like") to sp^3 ("diamond-like") binding ratio. Other significant factors that influence the binding characteristics include density as well as the presence of any hydrogen in the system. The sp^2

to sp^3 binding ratio is, in fact, closely related to the density and stress of synthesis [88], with a lower density and/or stress corresponding to a higher proportion of sp^2 binding.

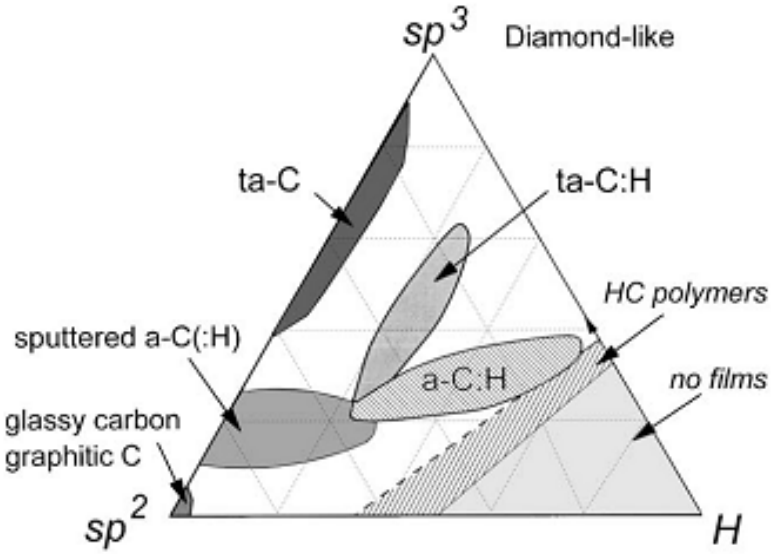

Fig. 5-13. Phase diagram of amorphous carbon, from [89]. The abbreviation ta-C refers to tetrahedral amorphous carbon.

Amorphous structures can be generated in MD by raising the temperature of a graphite system to well beyond its melting point and then quenching back to a sub-melting temperature. This severely disrupts the distinctive layering of the basal planes, resulting in a structure that is isotropic and less energetically favorable than crystalline graphite. To study the effects of amorphization, a 4,000 atom graphite supercell was heated to 9000 K and then cooled down at a rate of 2000 K per 2.5 picoseconds to a final temperature of 300 K. Densities of 1.7 g/cm^3 and 2.23 g/cm^3 were selected for investigation. The amorphized structure is displayed in Fig. 5-14 and the associated phonon frequency distribution is plotted in Fig. 5-15. Comparisons are drawn to a set of neutron spectroscopy measurements of $\rho(\omega)$ performed by Kamitakahara [90] on sputtered and glassy carbon samples.

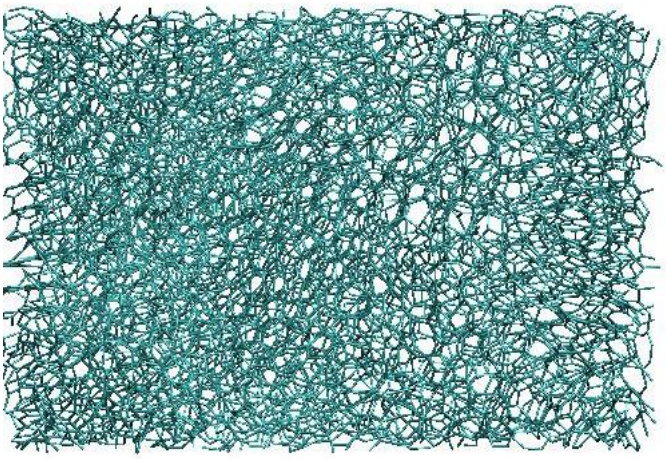

Fig. 5-14. Snapshot of an MD amorphous carbon system at T = 300 K and ρ = 1.7 g/cm^3.

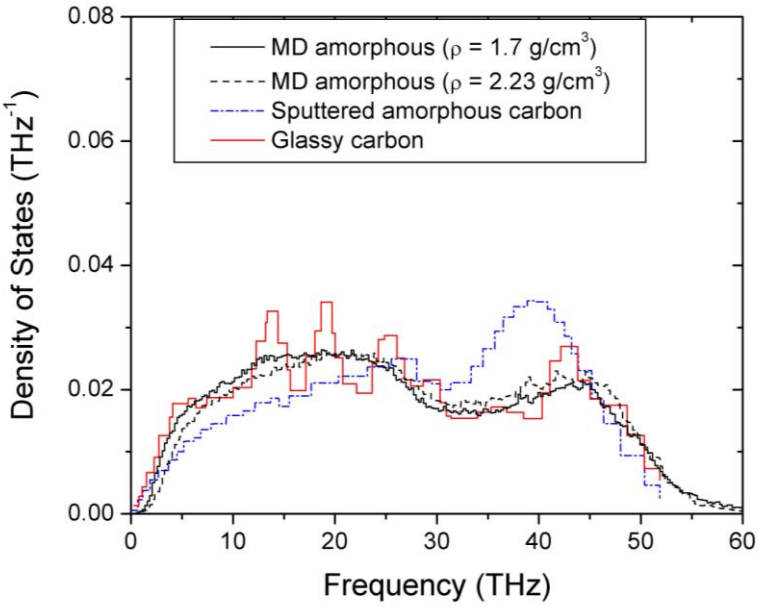

Fig. 5-15. MD amorphous ρ(ω) versus the measured distributions of sputtered and glassy carbon.

While all four distributions possess certain common features such as the disappearance of the optical graphitic peak at 50 THz, a particularly close correspondence is noticeable between the glassy carbon sample and the MD amorphous systems. One significant difference between glassy carbon and sputtered carbon is the sp^3 content, which is almost nonexistent in

the glassy form [89] but comprises a non-negligible fraction of sputtered carbon. The REBO potential is known to favor sp^2 binding preferentially in amorphous carbon [91], and the calculated distribution of bond types in the MD amorphous system, as listed in Table 5.1, indeed reveals a preponderance of sp and sp^2 binding. The resemblance of the MD $\rho(\omega)$ to glassy carbon is, therefore, not surprising.

Also relevant is the typical density of glassy carbon – about 1.47 g/cm^3 [92] – which is less than the average density of reactor-grade graphite and far below the density of the crystalline form. Indeed, agreement in $\rho(\omega)$ is seen to improve as the MD amorphous system density is decreased from 2.23 to 1.7 g/cm^3, implying that density plays an important role in shaping the vibrational distribution (and cross section) of the system. As expected, densification of the MD system causes a shift in $\rho(\omega)$ towards higher frequencies.

Table 5.1. Fractions of sp, sp^2, and sp^3 binding in the amorphous MD systems

	1.7 g/cm^3	2.23 g/cm^3
sp	0.20	0.07
sp^2	0.79	0.92
sp^3	0.01	0.02

5.5 Cross Section Impact

Defect structures such as those described in section 5.2 would be expected to substantially alter the thermal neutron scattering properties of graphite. Fundamentally, the cross section at thermal energies is dependent upon the details of interatomic binding, and these details

change as irradiation disrupts existing bonds while simultaneously originating new bond types in the structure. The effect of structure is illustrated well by the cross sectional difference between pyrolytic and nuclear-grade graphite (see Fig. 1-6). A*b-initio* based studies [21] suggest that the presence of simple interstitial or di-interstitial defects at concentrations of 3-5% can boost the cross section by 10-80% depending on temperature and incident energy. However, the impact of other damage formations (including basal plane vacancies and defect aggregates) is unknown at present. Results presented earlier in this work indicate that:

(1) MD techniques are capable of generating realistic damage formations in graphite.

(2) The thermal scattering cross section is accurately determinable from the classical time-dependent positions of the atoms comprising these formations

Thus, an appropriate set of tools has been assembled to perform a broader analysis of irradiation effects on the cross section. The goal of this section is to expand the scope of the *ab-initio* studies to encompass realistic defect clusters, and also to examine the effect of cascade buildup.

Cascade damage was introduced to an 8000-atom MD supercell through a series of 1.5 keV cascades that were initiated from random lattice sites and always directed towards the center of the system. Because each PKA recoils towards the supercell center, damage accumulation is highly non-uniform, and the centermost region is preferentially damaged whereas much of the remainder of the system is left unaltered. Cross section analysis was performed only on the damaged region of the supercell, herein defined as all atoms that possessed (at any point

in the simulation) a kinetic energy in excess of the threshold displacement energy (E_d) of graphite, as well as all neighbors of those atoms. E_d varies with crystallographic direction in graphite [28] and assumes a minimum value in the range of 23 – 36 eV ([28],[93],[94]). For the purposes of the present work, a threshold energy of 30 eV is assumed.

5.5.1 Cascade buildup at 300K

Fig. 5-16 through Fig. 5-19 show the cross section effect of a progressively increasing degree of damage in the graphite system. Changes in the scattering law are indicated in Fig. 5-20. The displayed set of plots include snapshots of the atoms comprising the damaged region of the supercell; from the time-dependent positions of these atoms, the incoherent cross section of the damaged region was determined using the correlation function methods developed in Chapters 3 and 4. Also shown is the progression of $\rho(\beta)$ with increasing cascade buildup. According to this analysis, radiation damage causes an *increase* in the inelastic cross section by as much as 48%, with the largest augmentation observed in the incident energy range of 0.01 – 0.03 eV. As the level of damage rises, the defect structure transitions from simple vacancies and interstitials to partial amorphization at the highest buildup level. Structural changes caused by damage are further elucidated by the behavior of $G_s(r,t)$, given in Fig. 5-21. Because defect-laden regions of the supercell can maintain a higher temperature than the overall system within the studied timeframe, cross section analysis was performed at the average temperature of the damaged region, which varies by as much as 28% from the bath temperature.

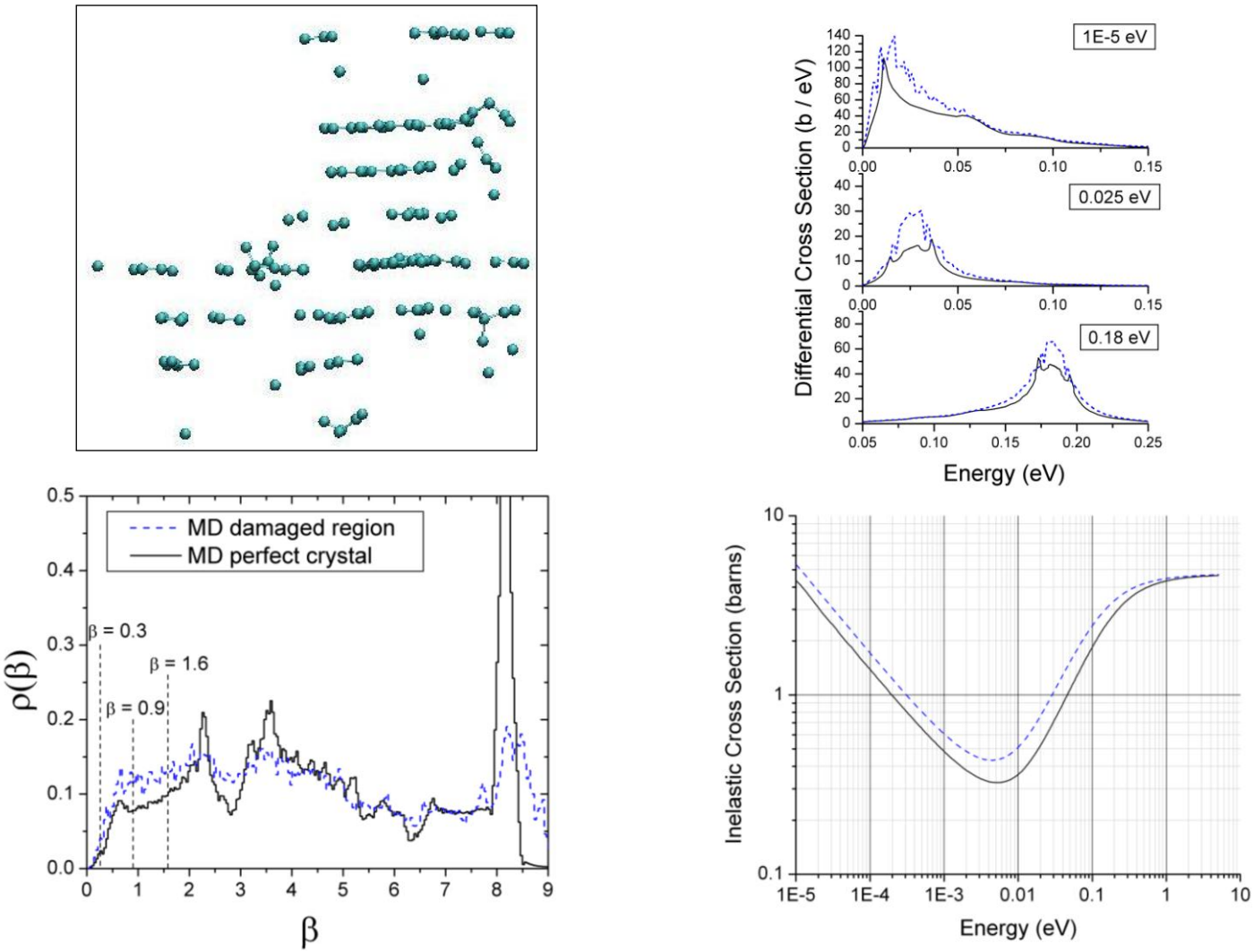

Fig. 5-16. Damage effect on the total and differential cross section following (1) 1.5 keV cascade initiated at 300 K.

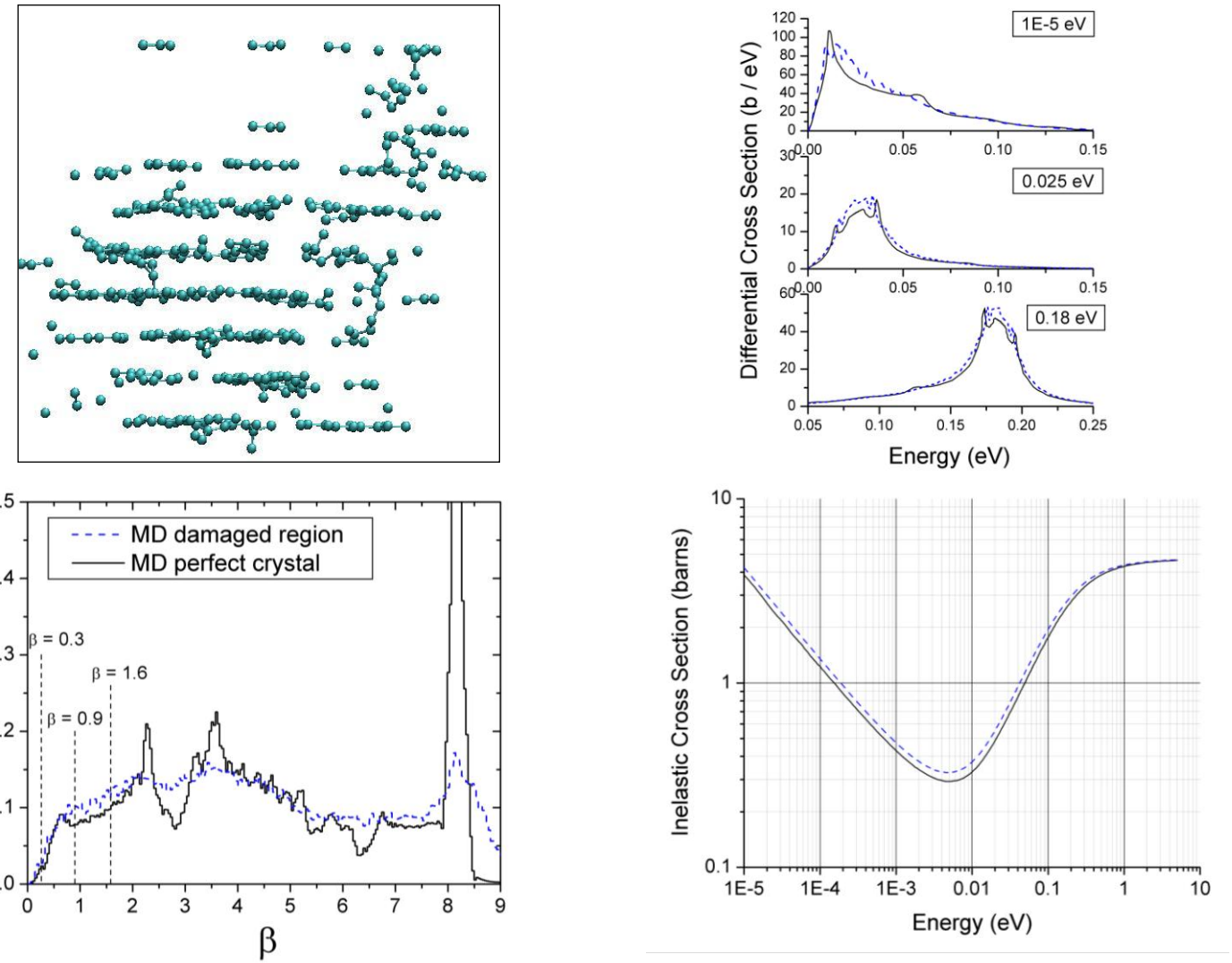

Fig. 5-17. Damage effect on the total and differential cross section following (3) 1.5 keV cascades initiated at 300 K.

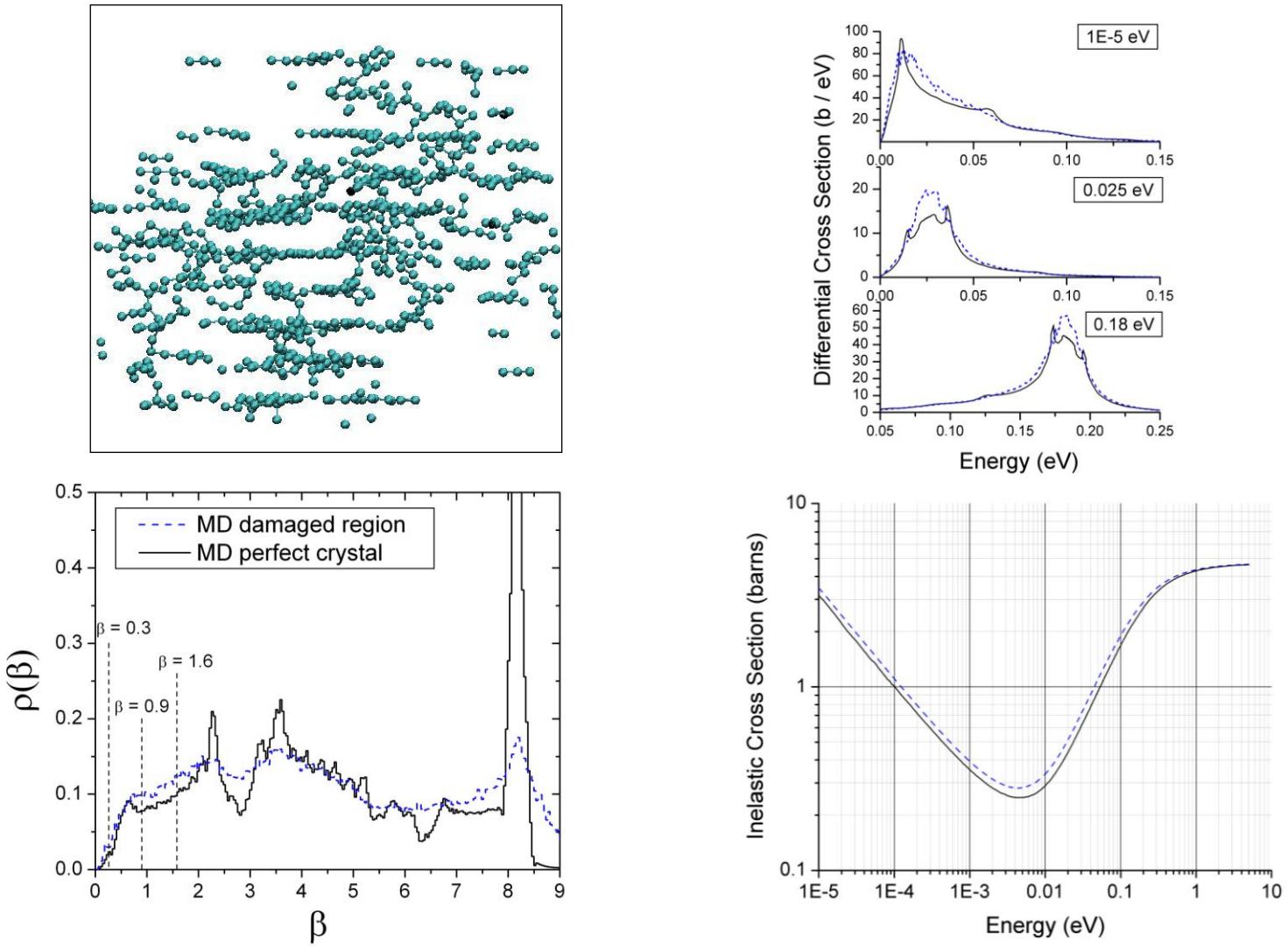

Fig. 5-18. Damage effect on the total and differential cross section following (7) 1.5 keV cascades initiated at 300 K.

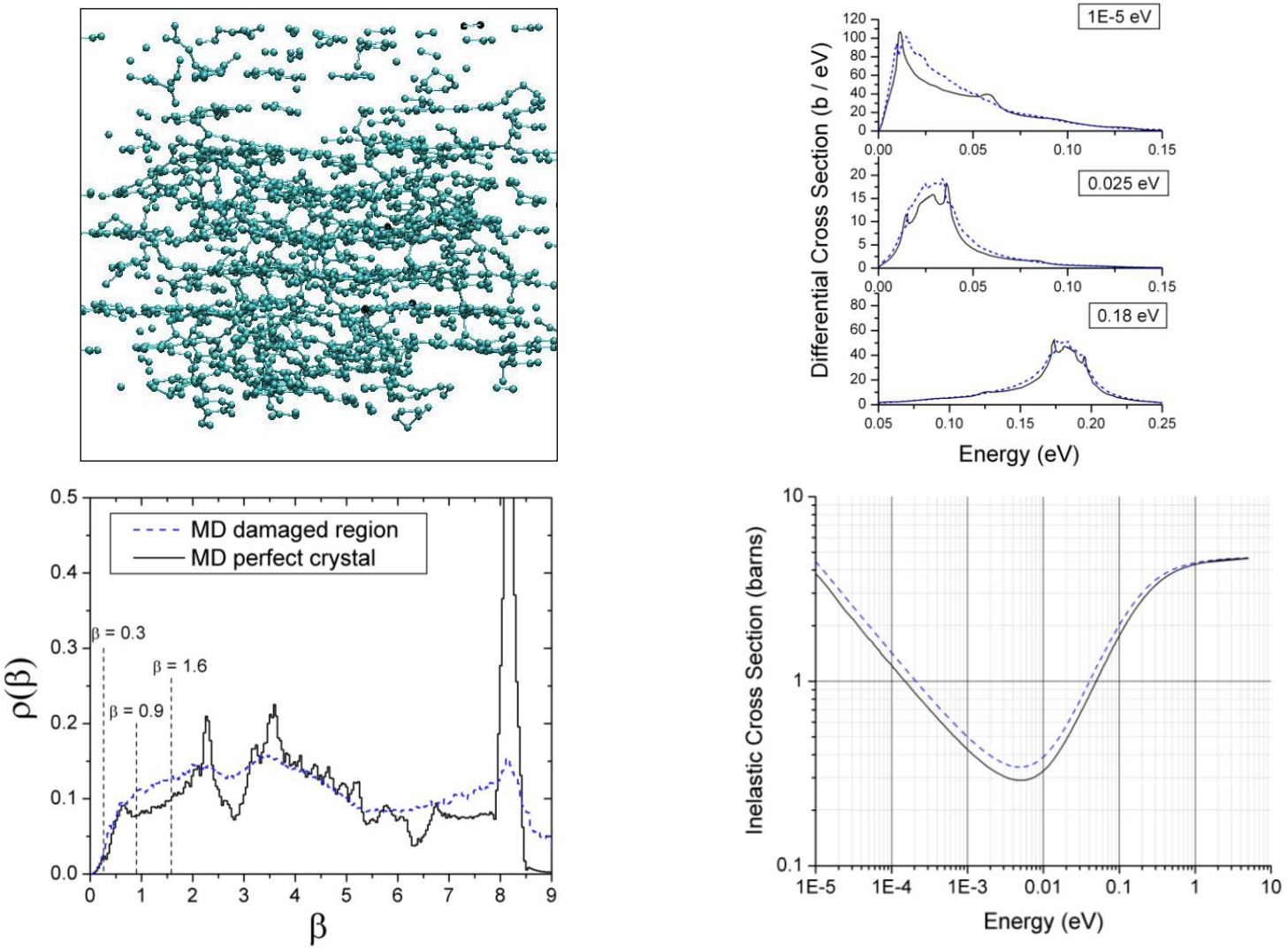

Fig. 5-19. Damage effect on the total and differential cross section following (13) 1.5 keV cascades initiated at 300 K.

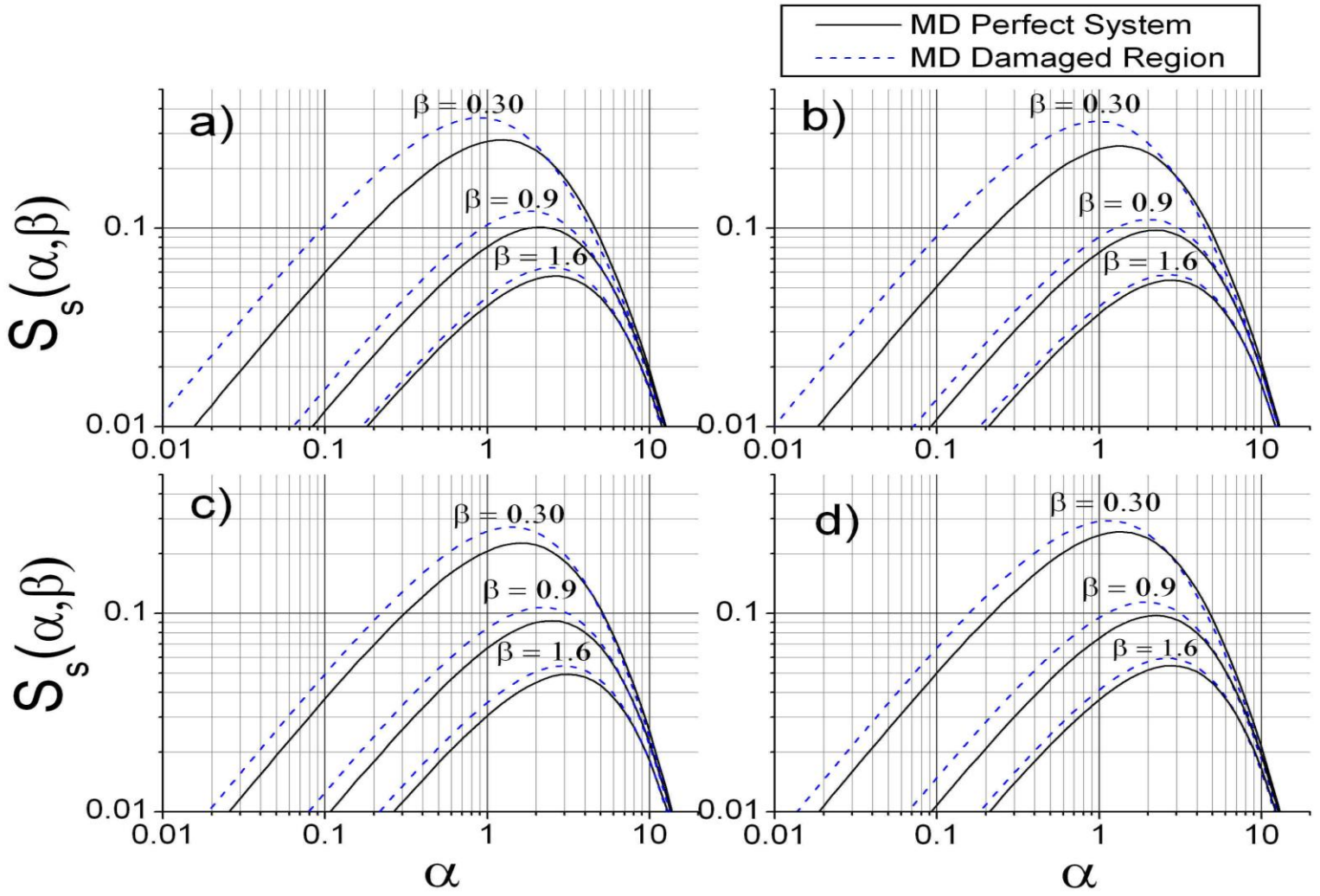

Fig. 5-20. Effect of cascade buildup on the self part of the thermal scattering law following a) 1 cascade; b) 3 cascades; c) 7 cascades; and d) 13 cascades

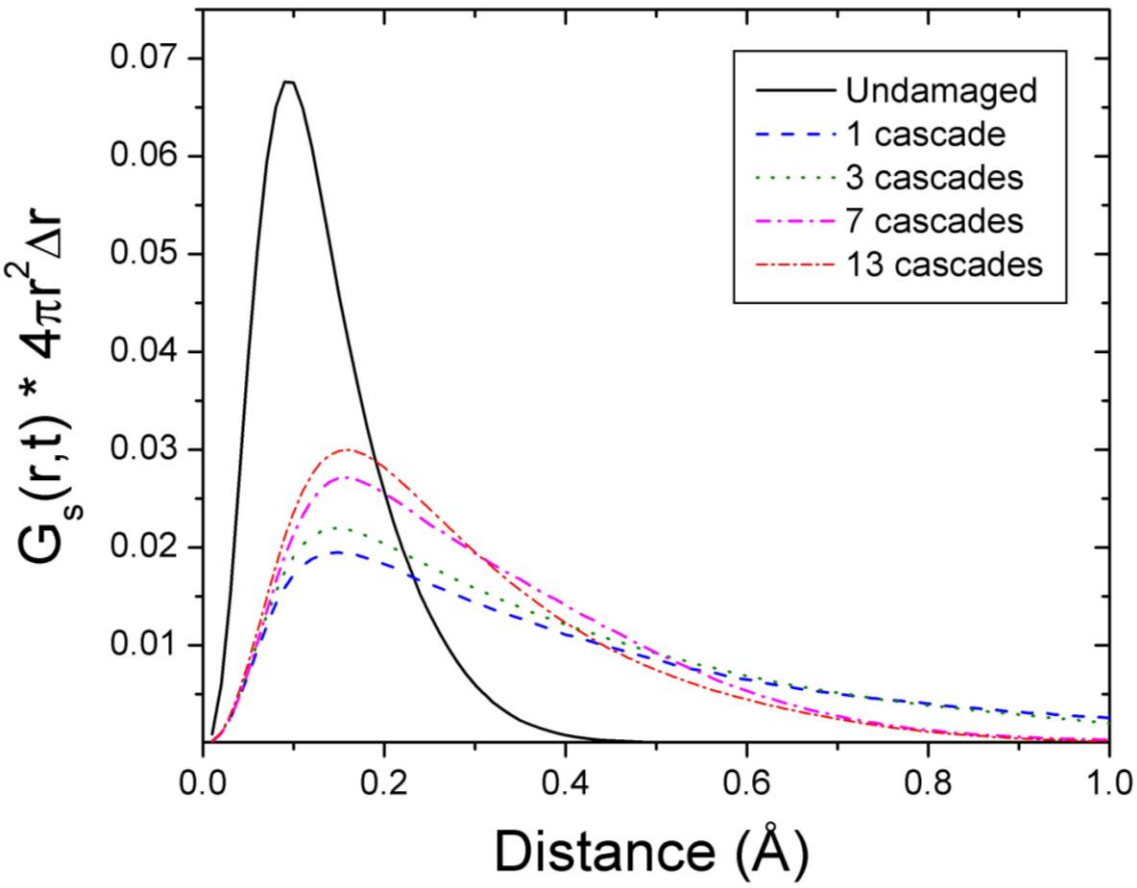

Fig. 5-21. Effect of damage on the self part of $G^{cl}(r,t)$. The displacement bin width, Δr, is 0.01 Å.

As apparent in the above plots, cascade buildup tends to increase the availability of low-frequency vibrational states, which in turn raises the magnitude of the scattering law in the corresponding range of energy transfers. Indeed, from Eqs. (4.10) and (4.11), the scattering law is seen to be directly proportional to ρ(β) in the limit of small α. The interrelations between ρ(β) and S(α,β) are demonstrated by comparing S(α,β) in the damaged region to S(α,β) in crystalline graphite, at specific values of β chosen to correspond with significant features of the ρ(β) curve. These values of β were selected from the low energy portion of

$\rho(\beta)$, which exerts a disproportionate influence on the scattering cross section due to the attenuation of accessible modes through the Planck distribution. By the same token, alterations to the features of $\rho(\beta)$ at high frequencies have a negligible impact on the cross section. In the high- energy (free atom) limit of $\sigma(E)$, the accessibility of vibrational states is unrelated to the magnitude of the cross section.

The presence of any degree of damage caused broadening and shifting in $G_s(r,t)$, which, through Eq. (4.6), is associated with a greater freedom of movement (i.e. a higher mean-squared displacement). In general, an increase in the mean-squared displacement is indicative of a greater availability of low frequency vibrational modes. This is consistent with the observed changes in the vibrational spectra and scattering law.

Because the MD-derived scattering law is distilled from the Fourier transformation of a time-dependent signal, the primary source of uncertainty in the calculated cross section is the signal length itself. Assuming that the bin width in frequency space is held constant, the variance of individual estimates of the scattering law (or of any other function of ω) will exhibit a $1/N$ relationship, where N is the signal length. Consequently, a test of convergence with respect to N is useful in assessing the uncertainty of the present calculations. For this purpose, the effect of N on the computed 3-cascade frequency distribution is shown in Fig. 5-22. Anisotropy in the graphite structure implies that some additional uncertainty could arise from the directionality of PKA launch. This factor is negligible at higher buildup levels and could be eliminated entirely through a directional-averaging procedure.

Little change is observed when *N* is raised from 131072 steps to 262144 steps, although some minor shifting does occur in the highest-frequency modes. At lower frequencies, the increase in *N* is associated with a smoothing of the distribution (as anticipated due to the reduction of variance); however, no significant changes are evident in the distribution itself. Hence, the frequency-dependent properties of the system are judged to be well-converged at this signal length.

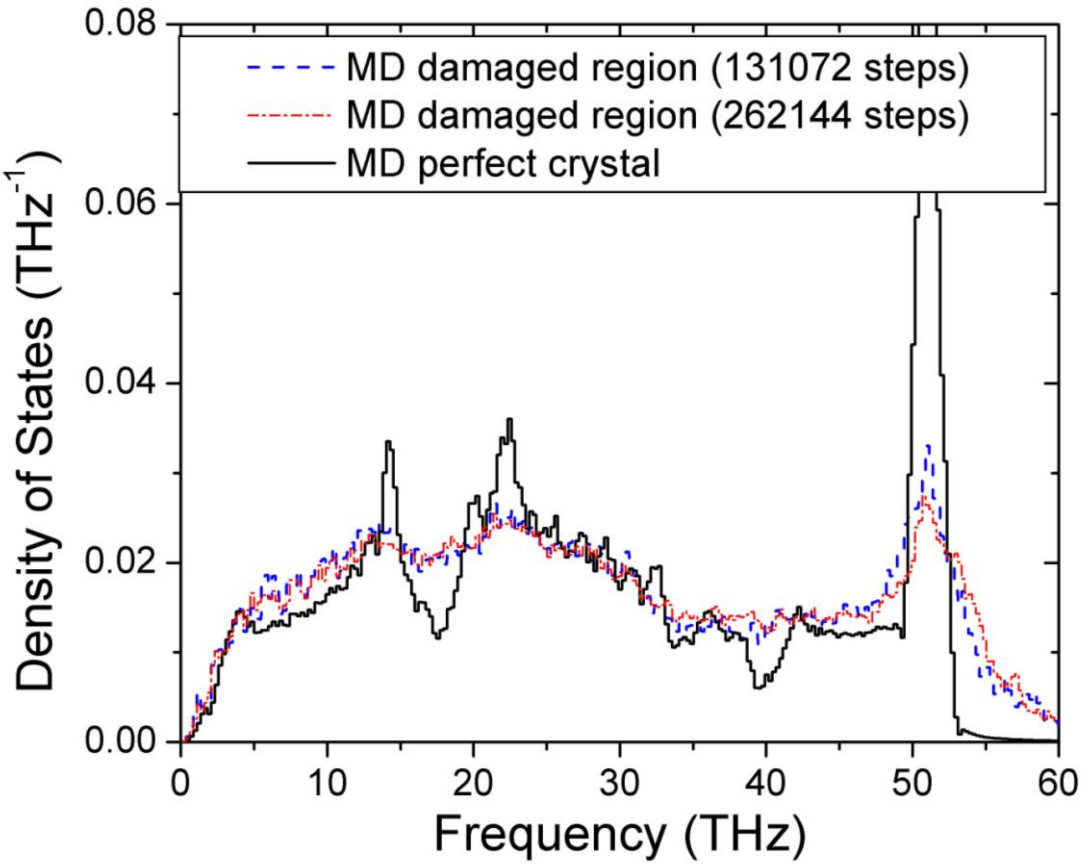

Fig. 5-22. Convergence of the frequency distribution with respect to the number of MD time steps.

5.5.2 Cascade buildup at 800K

Since the temperature of the scattering system can influence the cascade buildup process, it is productive to compare the 300K results against those from an equivalent high-temperature simulation. To this end, the sequence of (3) successive 1.5 keV cascades was repeated at an ambient temperature of 800K. The resulting cross sections and frequency distribution are given in Fig. 5-23, and the associated scattering law is shown in Fig. 5-24. Little change is observed relative to the 300K run, suggesting that the impact of temperature is minimal on the MD timescale. On a larger timescale, however, a higher ambient temperature would be expected to enhance diffusional processes in accordance with the Arrhenius factor, possibly leading to an annealing mechanism that alters the post-cascade structure (and cross section) to a much greater extent than at 300 K. This prospect remains speculative under the framework of the present calculations, which are applicable prior to the commencement of diffusional migration.

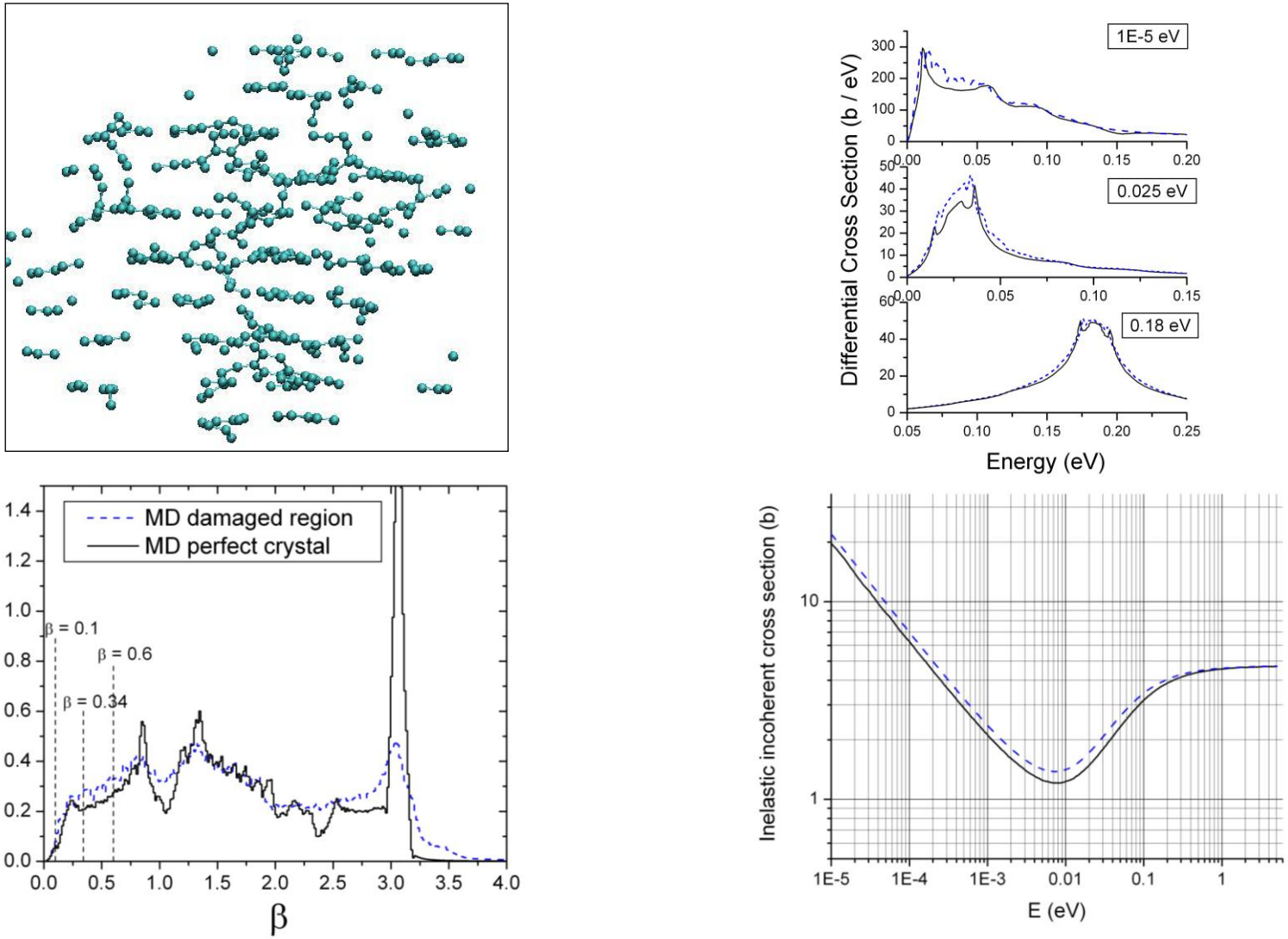

Fig. 5-23. Damage effect on the total and differential cross section following (3) 1.5 keV cascades initiated at 800 K.

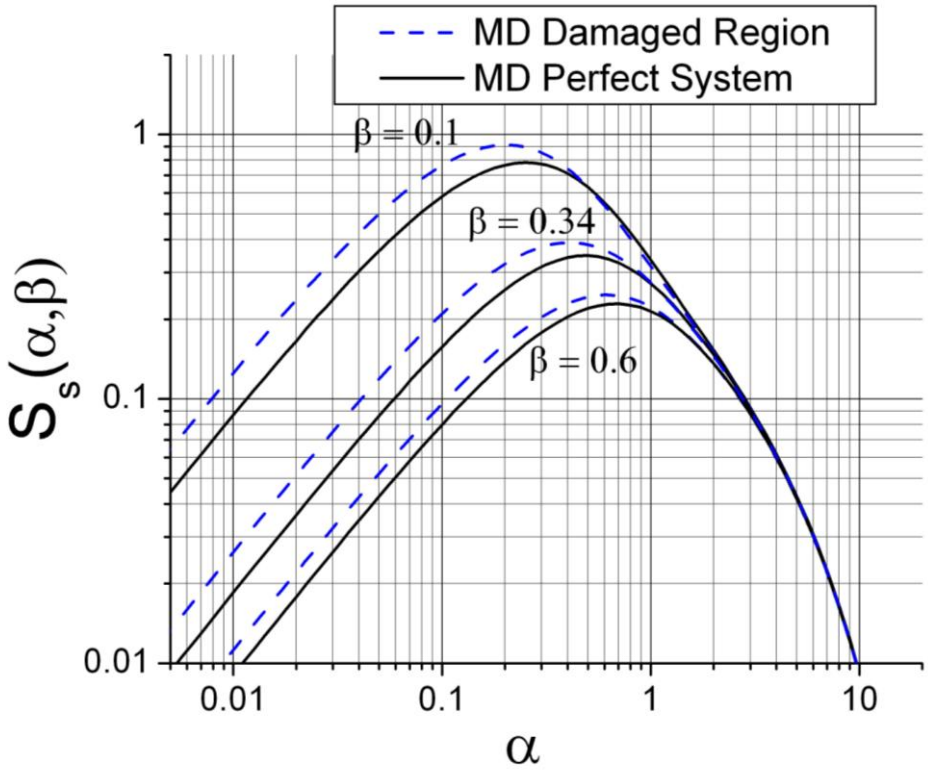

Fig. 5-24. Effect of cascade buildup on the self part of the thermal scattering law following (3) successive cascades at 800K.

5.5.3 Impact of damage on ρ(ω)

As the level of damage increases, and especially at high frequencies, ρ(ω) shows an unmistakable evolution towards the frequency distribution of amorphous carbon as illustrated in Fig. 5-25. For purposes of comparison, the *ab-initio* derived frequency distribution of a perfect 36-atom graphite supercell containing a di-interstitial [21] is displayed in Fig. 5-26. Noteworthy similarities include the enhanced availability of vibrational modes in the range of β =1 to β = 2, as well as the shallowing and shifting of the trough at β = 2.75. The sharp peak in the MD distribution just above 50 THz is conspicuously dampened by cascade damage

buildup, which is to be expected since the concentration of damage is gradually transforming the system into a more isotropic state, thereby breaking the 2D honeycomb arrangement that is responsible for the high-energy optical modes. This effect is not witnessed in the high-energy modes of the *ab-initio* di-interstitial system, in which the layered structure surrounding the defect was left intact. Conceptually, it is rational to posit that the presence of basal plane vacancies would affect these optical modes to a much greater extent than would interplanar interstitials, since the pertinent optical modes are *in-plane* modes (see Fig. 4-3).

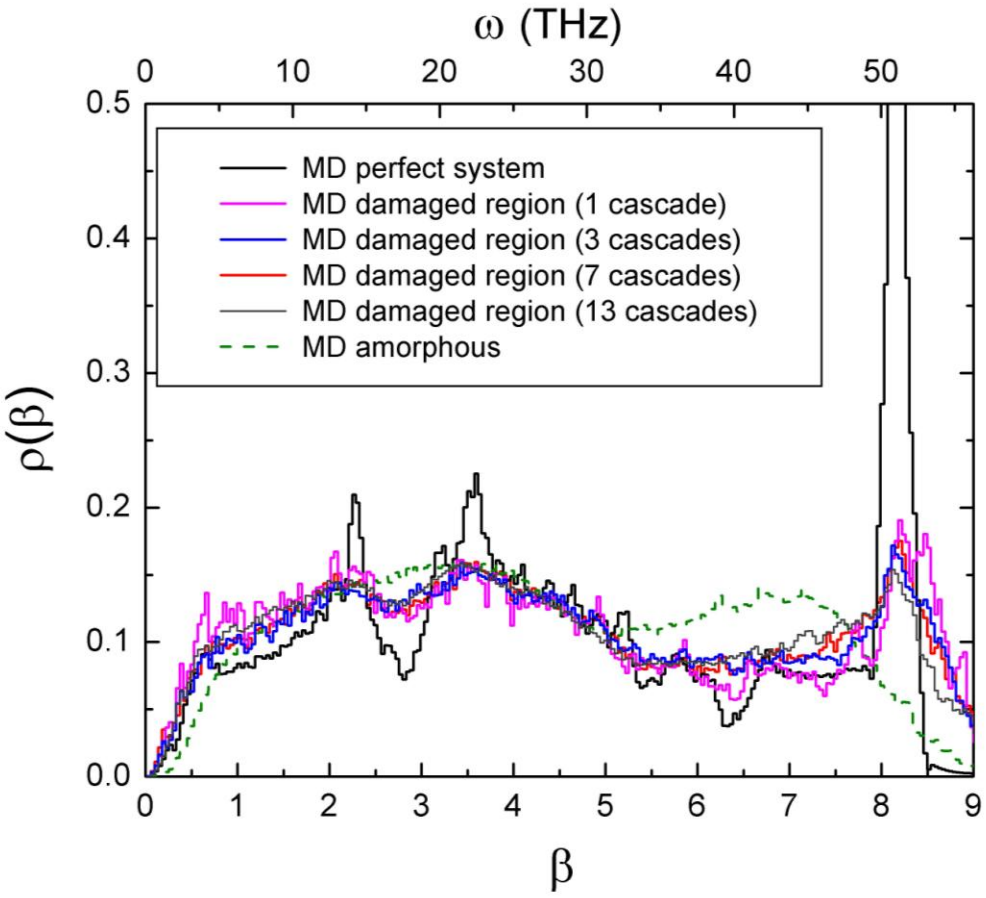

Fig. 5-25. Effect of cascade buildup on the frequency distribution of graphite

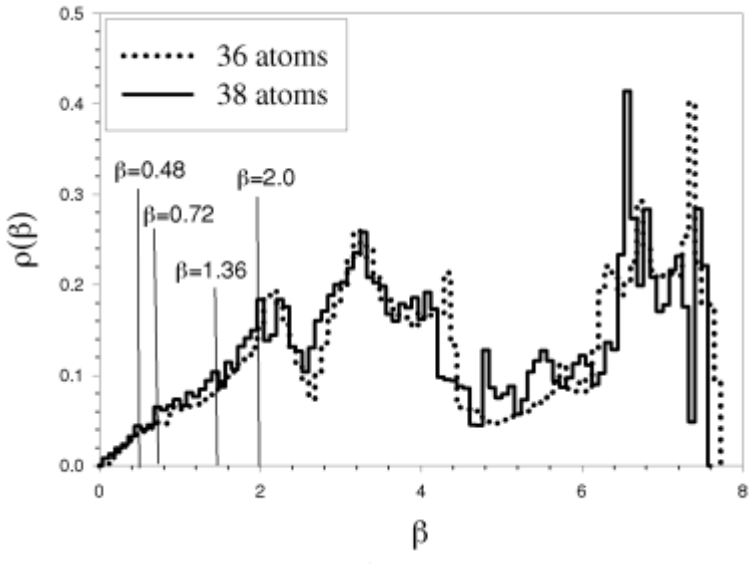

Fig. 5-26. *Ab-initio* based calculation of the ρ(β) impact of adding an interplanar di-interstitial into an otherwise perfect 36-atom graphite supercell, from [21].

As shown in Fig. 2-3, the out-of-plane MSD of graphite greatly exceeds the in-plane MSD due to the relative freedom of motion within the interlayer gap, which also defines the characteristics of the out-of-plane frequency spectrum. Vibrational modes in the range of 5 – 12 THz are predominantly out-of-plane optical (ZO) or out-of-plane acoustical (ZA) modes, and the existence of interplanar defects would be expected to redistribute the density of available states within this frequency interval. Similarly to the *ab-initio* di-interstitial study, the MD frequency distribution, following cascade buildup, reveals a substantial enhancement in the availability of modes at 5 – 12 THz.

Most of the distinctive features of the graphite distribution are progressively smoothed out as the damage buildup level rises. In fact, between 40 and 45 THz – a range coinciding with the high-energy peak of the frequency distribution of diamond – the change in the density of

states exhibits a positive trend with respect to damage. Cascade damage broadens the distribution of bond lengths and types, and it is therefore not surprising that the frequency distribution reflects a somewhat more diamond-like character even though the binding remains predominantly sp^2.

It is important to note that, in all MD simulations of cascade damage, the average system density was held fixed at the density of crystalline graphite. This fact, combined with the penchant of the REBO potential to unduly favor sp^2 binding, causes some difficulty in correlating the MD damaged or amorphous structures to the observed structure of reactor-grade graphite. Furthermore, the coexistence of two phases, the presence of pores and the resulting gradients in density are not considered in the present MD model.

Chapter 6

Conclusions and Future Work

In this work, the classical Van Hove correlation functions have been utilized to calculate the thermal neutron scattering cross section of graphite in the undamaged and damaged states. Although graphite is the focus of present work, the developed methodology is applicable to any atomistic system under any set of conditions. Molecular dynamics techniques were employed to model the graphite system and generate an appropriate set of atomic trajectories, which are the only required input for computations of the cross section. Interatomic interactions were evaluated using a modified REBO potential, in conjunction with a Lennard-Jones potential representing the long-ranged Van der Waals forces. The MD dynamics of the graphite system were benchmarked against temperature-dependent experimental data for the thermal expansion, mean-squared displacement, and thermal conductivity.

To distill accurate cross section data from the classical MD atomic positions, two main hurdles had to be overcome: first, the efficient evaluation of the classical Van Hove correlations from raw MD data, and second, the application of quantum corrections to the classical scattering formulae. In the absence of such corrections, the classical scattering law was shown to produce cross sections that approach σ_b rather than σ_f at high incident energies, and that overshoot reference data by nearly a factor of 5 at low energies.

Correlation function evaluations were made considerably faster by means of the cross correlation theorem, which reduced the calculation from an $O(N^2)$ to an O(NlogN) operation. Computations of the coherent scattering functions were sped up greatly by switching from κ-point sampling to the coherent Gaussian approximation beyond the first few neighbor shells of an atom.

The quantum effects of importance were identified as the detailed balance condition and atomic recoil, both of which relate to the response of the scattering system to neutron interaction. Furthermore, the system response was linked to the imaginary parts of G(r,t) and I(κ,t). Under the classical approximation, these functions are real and symmetric, thereby causing a violation of the first-order moment rule of S(κ,ω) while also preventing convergence to the free atom limit of the derived cross section. The application of a simple semiclassical harmonic correction to the classical scattering law was found to modify the scattering cross section appropriately at low incident energies, but divergence from the free atom limit remained apparent.

Due to the deficiencies discovered in the multiplicative semiclassical harmonic correction, a novel quantum correction approach was developed on the basis of a transformation from $I^{cl}(\kappa,t)$ to I(κ,t) based on the exact Van Hove equations for systems of classical and quantum harmonic oscillators. In this case, the relationship between the real and imaginary parts of I(κ,t) is grounded in fluctuation-dissipation theory, and Fourier transformation of the complex I(κ,t) function then yields the asymmetric quantum scattering law. In the limits of

small and large momentum transfers, the proposed transformation procedure was demonstrated to reduce to the semiclassical harmonic correction and the free atom correction respectively, where the free atom correction was derived from the quantum-classical correspondence principle.

The quantum-classical $I(\kappa,t)$ transformation was proven to generate consistent results that agree with *ab-initio* / NJOY calculations of the scattering law and cross section. The correlation function methods developed in the present work are considerably more versatile than the LEAPR / NJOY treatment, however, in that:

- The incoherent and Gaussian approximations are no longer compulsory.
- The phonon density of states is a byproduct of the calculation, rather than an input.
- The processing of the scattering law and cross section is independent of the state of matter.

All of these advantages have been demonstrated in Chapter 4 of the present work. The MD vibrational density of states, extracted from the low-α limit of $S_s(\alpha,\beta)$, closely matched analogous distributions obtained using the dynamical matrix and velocity autocorrelation formalisms. By combining the MD self and distinct density correlations, the total, coherent scattering law of graphite was determined and shown to agree with experimental measurements at 300K and 533K. Similarly good agreement was found in benchmarking against the coherent and incoherent scattering law of liquid argon at 120 K and 85.5 K respectively.

The effect of cascade buildup on the graphite model was studied by launching PKAs into the MD supercell, thereby causing collision cascades that leave residual defects in their wake. As the buildup is increased, the defect structure was shown to transition from simple vacancies and interstitials to extensive interplanar crosslinking, accompanied by the amorphization of certain regions. Specific defect types were identified in the damaged MD system such as the interplanar interstitial, di-interstitial, Stone-Wales defect and interplanar divacancy defect. The buildup of stored energy from these defects was confirmed in an MD simulation of 15 sequential 1.5 keV cascades in an 8000 atom system at 300 K, where, from the change in potential energy, it was found that 12% of the cascade energy (on average) was stored in the system through defects. Due to cascade overlap effects, the rate of stored energy buildup decreased with dose.

Because the thermal scattering cross section is highly sensitive to the atomic binding characteristics of the system, it was hypothesized that radiation damage would alter the cross section. Indeed, the cross section of damaged graphite was found to exceed the cross section of the crystalline form by as much as 48%, with the largest increase occurring in the incident energy range of 0.01 – 0.03 eV. All dose levels were associated with increases in the total cross section. From analysis of the frequency distribution and comparison against an *ab-initio* di-interstitial study, the enhancement of out-of-plane vibrational modes at 5 – 12 THz was correlated with the buildup of interstitials, while the attenuation of the highest-energy optical modes (around 50 THz) was linked to vacancies within the basal plane. These

changes were found to be consistent with the $\rho(\omega)$ impact of complete amorphization of the graphite system.

Future Work

Cross section calculations, in the present work, were performed on graphite in the damaged or undamaged state. Of great interest to the nuclear community is the thermal cross section characteristics of reactor-grade graphite – a porous, two-phase material comprised of regions of crystalline graphite embedded in a matrix of amorphous carbon. The classical correlation function methodology is entirely compatible with studies of reactor-grade graphite and is straightforward to implement once a reliable MD model of the system is formulated. Such a model could feature separate treatments of the amorphous and crystalline regions, or, alternatively, could combine them with an appropriate interface. The results of the present work (including damage effects) would be expected to apply to the crystalline region. An important consideration is the density of RG graphite, which averages to 1.6 – 1.85 g/cm^3 (18 – 30% lower than the crystalline state alone) but exhibits significant local variations due to the co-existence of dissimilar phases. Since variations in density can cause a frequency shift in the phonon spectrum, non-uniformities must be taken into account.

The accuracy of reactor core design calculations could be improved through the compilation of a comprehensive set of temperature- and dose-dependent scattering cross sections. Essentially, this task would be an extension of the final chapter of the present work. The generality of the cross section extraction tool developed herein suggests that such an analysis

could be performed on any reactor material of interest. Ideally, for coherent scatters such as carbon, the impact of damage on the coherent inelastic cross section would also be assessed. Coherent calculations of realistic systems exhibiting complex damage formations are expected to be rather expensive unless analysis is limited to localized regions of the structure. Enormous reductions in computational cost are achievable through implementation of the coherent Gaussian approximation in combination with a distance-based cutoff. Furthermore, since the cross section compilation code is designed to run on parallel processors (and with very little communicational overhead), a "brute force" strategy could certainly be taken.

References

[1] *A Technology Roadmap for Generation IV Nuclear Energy Systems.* December 2002. *US. DOE and Generation IV International Forum.* May 2010. <http://www.ne.doe.gov/genIV/documents/gen_iv_roadmap.pdf>

[2] J. J. Duderstadt and L. J. Hamilton. *Nuclear Reactor Analysis*. John Wiley & Sons, Inc., New York, NY, p. 324 (1976)

[3] *Graphite Material Safety Data Sheet (MSDS).* Updated November 2008. <http://www.sciencelab.com/xMSDS-Graphite-9924202>

[4] R. Wakeford. *J. Radiol. Prot.*, **27**, 211 (2007).

[5] C. R. Gould, A. I. Hawari and E. I. Sharapov. *Nuc. Sci. Eng.* **165**, 2000 (2010).

[6] H. Shi, J. N. Reimers and J. R. Dahn. *J. Appl. Crystallogr.*, **26**, 827 (1993).

[7] D. D. Dijulio and A. I. Hawari. *J. Nuc. Mat.*, **392**, 225 (2009).

[8] B. T. Kelly, B. J. Marsden and K. Hall. *Irradiation Damage in Graphite due to Fast Neutrons in Fission and Fusion Systems* TECDOC-1154. International Atomic Energy Agency, Vienna, Austria, (2000). Available online at http://www.iaea.org.

[9] R. E. MacFarlane and D. W. Muir, *The NJOY Nuclear Data Processing System, Version 91*, LA-12740-MS, Los Alamos National Laboratory (1994).

[10] B. D. Hehr and A. I. Hawari. "Calculation of the Thermal Neutron Scattering Cross Section of Alpha Quartz", Proc. PHYSOR 2008: *Nuclear Power: A Sustainable Resource.* Interlaken, Switzerland, Sept. 14-19, (2008).

[11] B. D. Hehr and A. I. Hawari, "Generation of Thermal Neutron Scattering Libraries for Beryllium Carbide," Proc. INREC'10: *International Nuclear and Renewable Energy Conference*. Amman, Jordan, March 21-24, (2010).

[12] A. I. Hawari, I. I. Al-Qasir, V. H. Gillette, B. W. Wehring and T. Zhou. "Ab Initio Generation of Thermal Neutron Scattering Cross Sections", Proc. PHYSOR 2004: *The Physics of Fuel Cycles and Advanced Nuclear Systems: Global Developments*. Chicago, USA, Apr. 25-29, (2004).

[13] A. I. Hawari, I. I. Al-Qasir and K. K. Mishra. "Accurate Simulation of Thermal Neutron Filter Effects in the Design of Research Reactor Beam Applications", Proc. PHYSOR 2006, Vancouver, Canada, Sept. 10-14 (2006).

[14] I. I. Al-Qasir. *Thermal Neutron Scattering in Graphite,* Ph.D. Dissertation, North Carolina State University (2007).

[15] J. A. Young and J. U. Koppel. *J. Chem. Phys.*, **42**, 357 (1965).

[16] A. Steyrel and W. D. Trustedt. *Z. Physik*., **267**, 379 (1974).

[17] P. A. Egelstaff. *J. Nuc. Energy,* **5**, 203 (1957).

[18] D. J. Hughes and R. B. Schwartz. *Neutron Cross Sections,* 2nd ed., Brookhaven National Laboratory Report BNL-325, 95 (1958).

[19] T. Zhou. *Benchmarking Thermal Neutron Scattering in Graphite*, Ph.D. Dissertation, North Carolina State University (2006).

[20] A. I. Hawari, T. Zhou and P. R. Huffman. "Measurement of the Total Inelastic Scattering Cross Section of Graphite using 9 Angstrom Neutrons," *Transactions of the American Nuclear Society*, **100**, 591 (2009).

[21] A. I. Hawari, I. I. Al-Qasir and A. M. Ougouag, *Nuc. Sci. Eng.*, **155**, p. 449 (2007).

[22] R. Kubo, M. Toda and N. Hashitsume. *Statistical Physics II*. 2nd ed., Springer-Verlag, Berlin, Germany, (1991).

[23] J. E. Jones. *Proc. R. Soc. Lond. A*, **106**, 463 (1924).

[24] G. C. Abell. *Phys. Rev. B.*, **31**, 6184 (1985).

[25] D. W. Brenner, O. A. Shenderova, J. A. Harrison, S. J. Stuart, B. Ni, and S. B. Sinnott, *J. Phys.: Cond. Matt.*, **14**, 783 (2002).

[26] J. Tersoff. *Phys. Rev. Lett.*, **39**, 5566 (1989).

[27] S. J. Stuart, A. B. Tutein and J. A. Harrison. *J. Chem. Phys.*, **112**, 6472 (2000).

[28] B. D. Hehr, A. I. Hawari and V. H. Gillette, *Nuclear Technology*, **160,** 251 (2007).

[29] M. Hasegawa and K. Nishidate, *Phys. Rev. B*, **70,** 205431 (2004).

[30] E. Fitzer and U. Funk. *Carbon*. **16,** 85 (1978).

[31] B. Firey, F. W. de Wette, and E. de Rouffignac, *Phys. Rev. B*, **28**, 7210 (1983).

[32] B. T. Kelly, *Journal of Nuclear Materials*, **24**, 210 (1967).

[33] E. A. Kellett, B. P. Jackets and B. P. Richards. *Carbon*, **2**, 175 (1964).

[34] B. Post. *Acta Crystallogr.*, **13**, 1103 (1960).

[35] A. P. P. Nicholson and D. J. Bacon, *J. Phys. C: Solid State Phys.*, **10**, 2295 (1977).

[36] B. D. Hehr, *High Temperature Graphite Simulations using Molecular Dynamics*, M.S. Thesis, North Carolina State University (2007).

[37] B. H. Billings and D. E. Gray, *American Institute of Physics Handbook*, McGraw-Hill, New York (1972).

[38] E. G. Steward, B. P. Cook, and E. A. Kellet, *Nature*. **187**, 1015 (1960).

[39] A. C. Bailey and B. Yates, *J. Appl. Phys*., **41**, 5088 (1970).

[40] A. Papoulis, *Probability, Random Variables, and Stochastic Processes*, McGraw-Hill Inc., New York, USA (1991).

[41] J. M. Haile, *Molecular Dynamics Simulation*, John Wiley & Sons Inc., New York, USA (1997).

[42] N. Zettili, *Quantum Mechanics: Concepts and Applications*, 2nd ed., John Wiley & Sons Ltd., West Sussex, UK (2009).

[43] G. L. Squires, *Introduction to the Theory of Thermal Neutron Scattering*, Dover Publications Inc., New York, USA (1987).

[44] K. Huang, *Statistical Mechanics*, 2nd ed., Wiley, New York, USA (1987).

[45] D. E. Parks, M. S. Nelkin, J. R. Beyster and N. F. Wikner. *Slow Neutron Scattering and Thermalization*. W.A. Benjamin Inc., New York, USA (1970).

[46] G. I. Bell and S. Glasstone. *Nuclear Reactor Theory*. Krieger Publishing Co., Malabar, USA (1970).

[47] G. R. Kneller, V. Keiner, M. Kneller and M. Schiller, *Comp. Phys. Comm.*, **91**, 191 (1995).

[48] M. Aichele and J. Baschnagel. *Eur. Phys. J. E.*, **5**, 229 (2001).

[49] Materials Explorer 4.0 Ultra, Fujitsu Ltd. (2006).

[50] A. Rahman. *Phys. Rev.*, **136**, 405 (1964).

[51] K. Sköld, J. M. Rowe and G. Ostrowski. *Phys. Rev. A*, **6**, 1107 (1972).

[52] A. A. van Well et al. *Phys. Rev. A*, **31**, 3391 (1985).

[53] S. A. Egorov, K. F. Everitt and J. L. Skinner. *J. Phys. Chem.*, **103**, 9494 (1999).

[54] P. Schofield. *Phys. Rev. Lett.*, **4**, 239 (1960).

[55] J. S. Bader and B. J. Berne. *J. Chem. Phys.*, **100**, 8359 (1994).

[56] T. D. Hone and G. A. Voth. *J. Chem. Phys.*, **121**, 6412 (2004).

[57] L. Frommhold. *Collision-induced absorption in gases*, 1st ed., Cambridge Monographs on Atomic, Molecular, and Chemical Physics, Vol. 2, Cambridge Univ. Press: London (1993).

[58] R. E. Turner. *Physica*, **27**, 260 (1961).

[59] V. F. Sears. *Phys. Rev. A*, **5**, 452 (1972).

[60] S. Sunakawa, S. Yamasaki and T. Nishigori. *Progress Theor. Phys.*, **37**, 1051 (1967).

[61] T. Nishigori and S. Sunakawa. *Progress Theor. Phys.*, **41**, 619 (1969).

[62] T. Nishigori. *Progress Theor. Phys.*, **43**, 1423 (1970).

[63] U. Bafile, L. Ulivi, M. Zoppi and S. Pestelli. *Mol. Phys.*, **79**, 179 (1993).

[64] K. Parlinski et al. *Phys. Rev. Lett*, **78,** 4063 (1997)

[65] C. Kittel. *Introduction to Solid State Physics.* 8th ed., John Wiley and Sons Inc., New York, NY, (2004).

[66] W. DeSorbo and G. E. Nichols, *J. Phys. Chem. Solids*, **6**, 352 (1958).

[67] W. H. Press, S. A. Teukolsky, W. T. Vetterling and B. P. Flannery. *Numerical Recipes: The Art of Scientific Computing*, Cambridge University Press, Cambridge, UK, p.656 (2007).

[68] J. Liu and W. H. Miller. *J. Chem. Phys.,* **128**, 144511 (2008).

[69] D. A. McQuarrie. *Statistical Mechanics.* Harper & Row, New York, NY, (1976).

[70] D. M. Kaplan and P. F. Zweifel. *Phys. Rev.*, **183**, 310 (1969).

[71] G. C. Wick. *Phys. Rev.,* **94**, 1228 (1954).

[72] N. F. Wikner, G. D. Joanou and D. E. Parks. *Nuc. Sci. Eng.,* **19**, 108 (1964).

[73] F. Carvalho. *Nuc. Sci. Eng.,* **34**, 224 (1968).

[74] B. T. Kelly. *Carbon*, **20**, 2 (1982).

[75] W. Humphrey**,** A. Dalke and K. Schulten. *J. Mol. Graphics*, **14**, 33 (1996).

[76] O. V. Yazyev, I. Tavernelli, U. Rothlisberger and L. Helm. *Phys. Rev. B,* **75**, 115418 (2007).

[77] L. M. Manocha. *Mat. Sci. Forum,* **223-224**, 117 (1996).

[78] R. H. Telling, C. P. Ewels, A. A. El-Barbary and M. I. Heggie. *Nature Materials*. **2**, 333 (2003).

[79] T. D. Burchell. *MRS Bulletin*. April (1997), p.29.

[80] E. P. Wigner. *J. Appl. Phys.*, **17**, 857 (1946).

[81] B. T. Kelly, *Physic of Graphite,* Applied Science Publishers, London, UK (1981).

[82] J. H. W. Simmons. *Radiation Damage in Graphite,* Pergamon Press, Oxford, UK (1965).

[83] R. E. Nightingale. *US/UK Graphite Conference*. Washington: United States Atomic Energy Commission TID-7565, pt.1, (1957).

[84] G. H. Kinchin. *Proc. First Int. Conference on the Peaceful Uses of Atomic Energy,* Vol. 7, United Nations, 472 (1956).

[85] J. C. Bell, H. Bridge, A. H. Cottrell, G. B. Greenough, W. N. Reynolds and J. H. W. Simmons. *Phil. Trans. Roy. Soc.*, **A254**, 361 (1962).

[86] J. E. Brocklehurst, B. S. Gray, J. G. Tindle, D. Mottershead and H. Sorensen. *Proc. Second SCI Conference on Industrial Carbons and Graphites*, SCI, London, 540 (1967).

[87] W. K. Woods, L. P. Bupp and J. F. Fletcher. *Proceedings of the International Conference on the Peaceful Uses of Atomic Energy*. VMIA/CONF 8/P/746, (1956).

[88] D. G. McCulloch, D. R. McKenzie and C. M. Goringe. *Phys. Rev. B*, **61**, 2349 (2000).

[89] J. Robertson. *Mat. Sci. Eng. R*, **37**, 129 (2002).

[90] W. A. Kamitakahara. *J. Phys. Chem. Solids*, **57**, 671 (1996).

[91] S. J. Stuart, M. T. Knippenberg, O. Kum and P. S. Krstic. *Phys. Scr.*, **T124,** 58 (2006).

[92] F. C. Cowlard and J. C. Lewis. *J. Mat. Sci.*, **2**, 507 (1967).

[93] H. J. Steffen, D. Marton and J. W. Rabalais. *Nuc. Instr. Meth. Phys. Res. B*, **67**, 308 (1992).

[94] G. L. Montet. *Carbon*, **5**, 19 (1967).

[95] R. E. Taylor, *Phil. Mag.*, **13**, p. 157 (1966).

[96] M. R. Null, W. W. Lozier and A. W. Moore, *Carbon*, **11**, p. 81 (1973).

Appendices

Appendix A

Thermal Conductivity

An interesting and important property that is expressible in terms of an MD correlation function is the thermal conductivity, K – a standard input parameter for thermal-hydraulics calculations involving fuel or moderator materials. Phenomenologically, K is defined in terms of the extent by which a temperature gradient instigates a heat flux in a given substance, as per the equation:

$$q'' = K\nabla T \tag{A.1}$$

where q'' is the heat flux (heat transmitted per unit area per unit time) and ∇T is the local temperature gradient. A well-known result of solid state physics is that thermal conductivity is fundamentally linked to the propagation of lattice vibrations in a crystal. Debye demonstrated that the conductivity expression can be derived from the kinetic theory of gases as:

$$K = \frac{1}{3} C_v v L \tag{A.2}$$

where v and L are the average particle velocity and mean free path respectively, and C_v is the heat capacity per unit volume [65]. This expression is also valid for solids when the variables v and L are interpreted as the phonon velocity and phonon mean free path. Eq. (A.2) applies only to the *phonon* component of K; in certain materials (especially pure metals), thermal energy is also transported by the electrons to a considerable extent. An implication of Eq. (A.2) is that, in the absence of some phonon scattering mechanism, solids

would be infinitely conductive. Real systems, however, exhibit phonon scattering from grain boundaries, from defects and from other phonons, with the latter process being highly temperature-dependent.

Changes in the thermal conductivity with temperature therefore represent a balance between the excitation of additional phonon modes and alterations in the phonon mean free path due to scattering phenomena. Since K is proportional to C_v, the conductivity is zero at 0 K (because there are no phonon excitations) and typically reaches a maximum before declining monotonically due to increased phonon-phonon scattering. This argument does not generally hold true for materials with a significant electronic component of K, as the electronic component tends to increase with temperature.

In the realm of equilibrium MD simulation, the Green-Kubo autocorrelation methodology is commonly used to estimate the phonon contribution to thermal conductivity. The quantity being correlated here is the heat current vector, $\vec{J}(t)$, which is completely determined by the positions, momenta, and interatomic potential energies as:

$$\vec{J}(t) = \sum_i \vec{v}_i h_i + \frac{1}{2}\sum_{i,j}\sum_{k,l} \vec{r}_{ik}\left(\vec{F}_{ij}^{\,kl} \cdot \vec{v}_i\right) \tag{A.3}$$

$$\vec{F}_{ij}^{\,kl} = -\frac{\partial V_{kl}}{\partial \vec{r}_{ij}} \tag{A.4}$$

where h_i is the site energy of atom i, $\vec{v}_i$ is its velocity, F is force, and $\vec{r}_{ij} = \vec{r}_j - \vec{r}_i$ is the vector displacement between atoms i and j. The conductivity relation is given by:

$$\lambda(T) = \frac{1}{3Vk_B T^2} \int_0^{\infty} d\tau \frac{1}{L(\tau)} \sum_{k=1}^{L(\tau)} \vec{J}(t_k) \cdot \vec{J}(t_k + \tau) \qquad \text{(A.5)}$$

where V is the MD supercell volume, T is temperature, and L(τ) is the number of MD steps available for averaging. Essentially, the magnitude of the integral in Eq. (A.5) – and hence the conductivity – depends upon how quickly the autocorrelation of the heat current vector dies away. In general, the more rapidly this decay occurs the lower the computed conductivity will be. It is well known that the increased frequency of phonon-phonon scattering processes at high temperatures gives rise to an inverse relationship between λ and T; in other words, the heat current vector quickly "loses memory" of its initial orientation due to the action of scattering events.

As a benchmark of the graphite MD code, as well as an illustration of the application of MD correlation functions, the basal plane conductivity was evaluated directly from Eqs. (A.3) - (A.5) between 300 K and 1800 K using a 12x12x1 (576 atom) supercell. Typical production run times ranged from 600 – 800 picoseconds under NVT ensemble conditions, with temperature held constant by a thermal bath. Fig. A-1 shows the convergence of the heat current autocorrelation integral over time, and the resulting conductivities are compared to the measurements of Taylor [95]and Null [96] in Fig. A-2. Agreement with experiment is reasonably good throughout the investigated range of temperatures. Error bars on the MD calculations represent the standard error of the mean and are shown for temperatures at which multiple conductivity calculations were performed (starting from different initial velocity distributions).

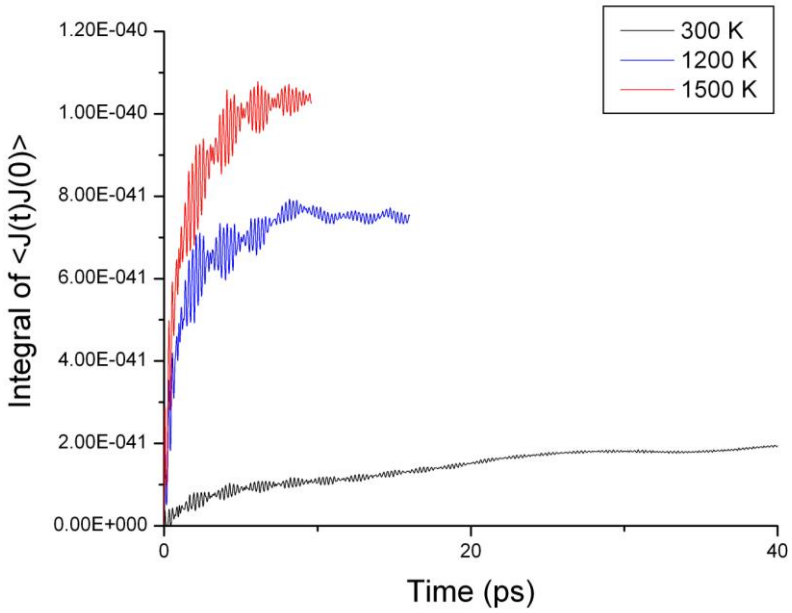

Fig. A-1. Convergence of the conductivity integral. The time required for convergence decreases withtemperature, as the heat current vector more quickly "loses memory" of its initial orientation.

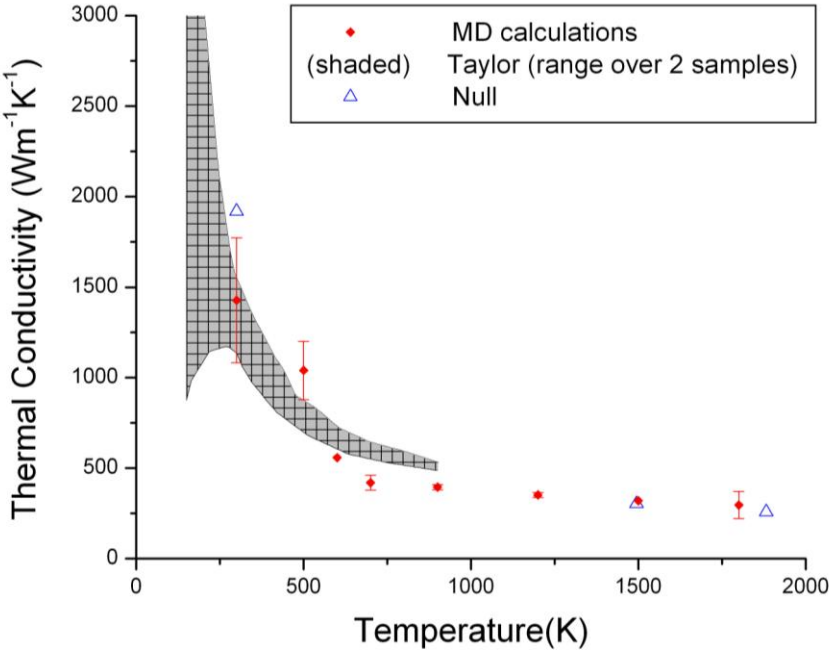

Fig. A-2. Thermal conductivity of the MD graphite system, calculated using the Green-Kubo methodology.

Appendix B

B.1 ρ(ω) from the Classical Scattering Law

Starting from the expression for the classical intermediate scattering function under the Gaussian approximation:

$$I_s^{cl}(\kappa,t) = \exp\left[-\frac{1}{2}\kappa^2\sigma^2(t)\right] \tag{B.1}$$

where:

$$\left\langle r^2(t)\right\rangle = 3\sigma^2(t) \tag{B.2}$$

and, recognizing that:

$$\left\langle r^2(t)\right\rangle = 2\int_0^t dt'(t-t')\left\langle v(0)\cdot v(t')\right\rangle \tag{B.3}$$

The second-order derivative of the mean squared displacement becomes:

$$\frac{d^2\left\langle r^2(t)\right\rangle}{dt^2} = 2\left\langle v(0)\cdot v(t)\right\rangle \tag{B.4}$$

Because the velocity autocorrelation function and the phonon density of states are Fourier conjugates of each other, the velocity autocorrelation can be written as:

$$\left\langle v(0)\cdot v(t)\right\rangle = \frac{3}{2}\frac{k_B T}{M}\int_{-\infty}^{\infty} d\omega\rho(\omega)\exp(i\omega t) \tag{B.5}$$

Therefore:

$$\frac{d^2\left\langle r^2(t)\right\rangle}{dt^2} = \frac{3k_B T}{M}\int_{-\infty}^{\infty} d\omega\rho(\omega)\exp(i\omega t) \tag{B.6}$$

Now, in the limit of small κ:

$$\lim_{|\kappa|\to 0}\left[I_s^{cl}(\kappa,t)\right] = 1-\frac{1}{2}\kappa^2\sigma^2(t) \tag{B.7}$$

Solving for $\sigma^2(t)$:

$$\sigma^2(t) = \lim_{|\kappa|\to 0}\left\{\frac{2\left[1-I_s^{cl}(\kappa,t)\right]}{\kappa^2}\right\} \tag{B.8}$$

and twice differentiating both sides with respect to time:

$$\frac{d^2\sigma^2(t)}{dt^2} = \lim_{|\kappa|\to 0}\left\{\frac{-2}{\kappa^2}\frac{d^2\left[I_s^{cl}(\kappa,t)\right]}{dt^2}\right\} \tag{B.9}$$

Combining Eqs. (B.2), (B.6), and (B.9), the following relation holds between the intermediate function and the density of states:

$$\lim_{|\kappa|\to 0}\left\{\frac{-2}{\kappa^2}\frac{d^2\left[I_s^{cl}(\kappa,t)\right]}{dt^2}\right\} = \frac{k_B T}{M}\int_{-\infty}^{\infty} d\omega\rho(\omega)\exp(i\omega t) \tag{B.10}$$

Differentiating the backwards Fourier transform of the classical Van Hove scattering law, it is apparent that:

$$\begin{aligned}\frac{d^2\left[I_s^{cl}(\kappa,t)\right]}{dt^2} &= \frac{d^2}{dt^2}\left\{\hbar\int_{-\infty}^{\infty} d\omega S_s^{cl}(\kappa,\omega)\exp(i\omega t)\right\}\\ &= \hbar(i\omega)^2\int_{-\infty}^{\infty} d\omega S_s^{cl}(\kappa,\omega)\exp(i\omega t)\\ &= -\hbar\omega^2\int_{-\infty}^{\infty} d\omega S_s^{cl}(\kappa,\omega)\exp(i\omega t)\end{aligned} \tag{B.11}$$

Substituting this expression into Eq. (B.10) and equating the integrands:

$$\rho(\omega) = \frac{2M\hbar\omega^2}{k_B T}\lim_{|\kappa|\to 0}\left[\frac{S_s^{cl}(\kappa,\omega)}{\kappa^2}\right] \tag{B.12}$$

or, in dimensionless form:

$$\rho(\beta) = \beta^2 \lim_{\alpha \to 0} \left[\frac{S_s^{cl}(\alpha, \beta)}{\alpha} \right] \tag{B.13}$$

which defines the relation between the density of states and the classical, symmetric scattering law.

B.2 ρ(ω) from the Quantum Harmonic Scattering Law

The quantum harmonic scattering law already depends upon ρ(ω) explicitly as:

$$S_s(\vec{\kappa}, \omega) = \frac{1}{2\pi} \int_{-\infty}^{\infty} \exp\left(\frac{\hbar \kappa^2}{2M} \int_{-\infty}^{\infty} \frac{\rho(\omega) \exp\left(\frac{\hbar \omega}{2k_B T} \right)}{2\omega \sinh\left(\frac{\hbar \omega}{2k_B T} \right)} \left[\exp(i\omega t) - 1 \right] d\omega \right) \exp(-i\omega' t)\, dt \tag{B.14}$$

Taking the low-κ limit and expanding the first exponential term on the RHS:

$$\lim_{|\kappa| \to 0} \left\{ S_s(\kappa, \omega) \right\} = \frac{1}{2\pi} \int_{-\infty}^{\infty} \exp(-i\omega' t)\, dt \; +$$

$$\frac{1}{2\pi} \left(\frac{\hbar \kappa^2}{2M} \right) \int_{-\infty}^{\infty} \left(\int_{-\infty}^{\infty} \frac{\rho(\omega) \exp\left(\frac{\hbar \omega}{2k_B T} \right)}{2\omega \sinh\left(\frac{\hbar \omega}{2k_B T} \right)} \left[\exp(i\omega t) - 1 \right] d\omega \right) \exp(-i\omega' t)\, dt \tag{B.15}$$

Noting that:

$$\delta(\omega') = \frac{1}{2\pi} \int_{-\infty}^{\infty} \exp(-i\omega' t)\, dt \tag{B.16}$$

The first term on the RHS of Eq. (B.15) is seen to be zero since, in any simple solid, $\rho(\omega) \rightarrow 0$ as $\omega \rightarrow 0$. Moreover, the present study is concerned with *inelastic* scattering, for which $\omega \neq 0$ by definition (i.e. at least one phonon must be excited or de-excited). After performing the integrations in the second term on the RHS, Eq. (B.15) reduces to:

$$\lim_{|\kappa|\to 0}\left\{S_s(\kappa,\omega)\right\} = \frac{\rho(\omega)\hbar\kappa^2 \exp\left(\frac{\hbar\omega}{2k_BT}\right)}{4M\omega\sinh\left(\frac{\hbar\omega}{2k_BT}\right)} \tag{B.17}$$

and converting from the asymmetric to the symmetric scattering law:

$$\lim_{|\kappa|\to 0}\left\{\tilde{S}_s(\kappa,\omega)\right\} = \frac{\rho(\omega)\hbar\kappa^2}{4M\omega\sinh\left(\frac{\hbar\omega}{2k_BT}\right)} \tag{B.18}$$

which, in terms of α and β, is equivalent to:

$$\lim_{\alpha\to 0}\left\{\tilde{S}_s(\alpha,\beta)\right\} = \frac{\alpha\rho(\beta)}{2\beta\sinh\left(\beta/2\right)} \tag{B.19}$$

Solving for the density of states, Eq. (B.18) becomes:

$$\rho(\omega) = \frac{4M\omega}{\hbar}\sinh\left(\frac{\hbar\omega}{2k_BT}\right)\lim_{|\kappa|\to 0}\left\{\frac{\tilde{S}_s(\kappa,\omega)}{\kappa^2}\right\} \tag{B.20}$$

and Eq. (B.19) becomes:

$$\rho(\beta) = 2\beta\sinh\left(\beta/2\right)\lim_{\alpha\to 0}\left\{\frac{\tilde{S}_s(\alpha,\beta)}{\alpha}\right\} \tag{B.21}$$

which reduces to the classical formula of Eq. (B.13) in the limit $\beta \rightarrow 0$. At any value of β, the classical and quantum distributions are related by conversion factor of Eq. (4.29) (without

the symmetrizing exponential term), which arose in the derivation of the classical-to-quantum $I(\kappa,t)$ transformation.

Appendix C

Derivation of the Harmonic Semiclassical Correction from the I(κ,t) Transform Equations

From the definition of the semiclassical correction to the scattering law:

$$Q(\beta)=\frac{S_s(\alpha,\beta)}{S_s^{cl}(\alpha,\beta)} \tag{C.1}$$

the harmonic correction is found by inserting the relevant expressions for systems of quantum ($S_s(\alpha,\beta)$) and classical ($S_s^{cl}(\alpha,\beta)$) harmonic oscillators, which are given by Eqs. (4.22) and (4.21) respectively. After this substitution, the correction factor becomes:

$$Q(\beta)=\frac{\int_{-\infty}^{\infty} dt'\exp(-i\beta' t')\exp\left[-\alpha\left\{\int_{-\infty}^{\infty}\frac{d\beta\rho(\beta)\exp\left(\beta/2\right)}{2\beta\sinh\left(\beta/2\right)}\right\}\left(1-\exp[i\beta t']\right)\right]}{\int_{-\infty}^{\infty} dt'\exp(-i\beta' t')\exp\left[-\alpha\left\{\int_{-\infty}^{\infty}\frac{d\beta\rho(\beta)}{\beta^2}\right\}\left(1-\cos(\beta t')\right)\right]} \tag{C.2}$$

where β' is a dummy Fourier transform variable. In the limit of small α:

$$Q(\beta)=\frac{\int_{-\infty}^{\infty} dt'\exp(-i\beta' t')\left[1-\alpha\left\{\int_{-\infty}^{\infty}\frac{d\beta\rho(\beta)\exp\left(\beta/2\right)}{2\beta\sinh\left(\beta/2\right)}\right\}\left(1-\exp[i\beta t']\right)\right]}{\int_{-\infty}^{\infty} dt'\exp(-i\beta' t')\left[1-\alpha\left\{\int_{-\infty}^{\infty}\frac{d\beta\rho(\beta)}{\beta^2}\right\}\left(1-\cos(\beta t')\right)\right]} \tag{C.3}$$

Utilizing the following relations:

$$\delta(\beta')=\frac{1}{2\pi}\int_{-\infty}^{\infty}\exp(-i\beta' t')dt' \tag{C.4}$$

$$\delta(\beta'-\beta)=\frac{1}{2\pi}\int_{-\infty}^{\infty}\exp\left(-i[\beta'-\beta]t'\right)dt' \tag{C.5}$$

$$\delta(\beta'-\beta)=\frac{1}{2\pi}\int_{-\infty}^{\infty}\cos(\beta t')\exp\left(-i\beta' t'\right)dt' \tag{C.6}$$

and carrying out the Fourier integration, Eq. (C.3) reduces to the following expression after the removal of the zero-frequency components of the transform:

$$Q(\beta)=\frac{\alpha\left\{\int_{-\infty}^{\infty}\frac{d\beta'\rho(\beta')\exp\left(\beta'/2\right)}{2\beta'\sinh\left(\beta'/2\right)}\delta[\beta'-\beta]\right\}}{\alpha\left\{\int_{-\infty}^{\infty}\frac{d\beta'\rho(\beta')}{(\beta')^2}\delta[\beta'-\beta]\right\}} \tag{C.7}$$

Integrating over the Dirac delta function simply isolates the integrand, herein evaluated at $\beta=\beta'$. Therefore:

$$Q(\beta)=\frac{\alpha\left(\frac{d\beta\rho(\beta)\exp\left(\beta/2\right)}{2\beta\sinh\left(\beta/2\right)}\right)}{\alpha\left(\frac{\rho(\beta)}{\beta^2}\right)} \tag{C.8}$$

and after converting the hyperbolic sine to exponential form and simplifying the resulting formula, Eq. (C.8) becomes:

$$Q(\beta)=\frac{\beta}{1-\exp(-\beta)} \tag{C.9}$$

which is identical to the harmonic semiclassical correction of Eq. (3.75).